Monthly Notices
of the
ROYAL ASTRONOMICAL SOCIETY

MNRAS **432,** 1768–1795 (2013)
Advance Access publication 2012 December 3

doi:10.1093/mnras/sts315

The ATLAS^{3D} project – XVII. Linking photometric and kinematic signatures of stellar discs in early-type galaxies

Davor Krajnović,[1]⋆ Katherine Alatalo,[2] Leo Blitz,[2] Maxime Bois,[3] Frédéric Bournaud,[4] Martin Bureau,[5] Michele Cappellari,[5] Roger L. Davies,[5] Timothy A. Davis,[1] P. T. de Zeeuw,[1,6] Pierre-Alain Duc,[4] Eric Emsellem,[1,7] Sadegh Khochfar,[8] Harald Kuntschner,[1] Richard M. McDermid,[9] Raffaella Morganti,[10,11] Thorsten Naab,[12] Tom Oosterloo,[10,11] Marc Sarzi,[13] Nicholas Scott,[14] Paolo Serra,[10] Anne-Marie Weijmans[15]† and Lisa M. Young[16]

[1]*European Southern Observatory, Karl-Schwarzschild-Strasse 2, D-85748 Garching bei München, Germany*
[2]*Department of Astronomy and Radio Astronomy Laboratory, University of California, Berkeley, CA 94720, USA*
[3]*Observatoire de Paris, LERMA and CNRS, 61 Av. de l'Observatoire, F-75014 Paris, France*
[4]*Laboratoire AIM Paris-Saclay, CEA/IRFU/SAp CNRS Université Paris Diderot, F-91191 Gif-sur-Yvette Cedex, France*
[5]*Sub-department of Astrophysics, Department of Physics, University of Oxford, Denys Wilkinson Building, Keble Road, Oxford OX1 3RH*
[6]*Sterrewacht Leiden, Leiden University, Postbus 9513, NL-2300 RA Leiden, the Netherlands*
[7]*Université Lyon 1, Observatoire de Lyon, Centre de Recherche Astrophysique de Lyon and Ecole Normale Supérieure de Lyon, 9 avenue Charles André, F-69230 Saint-Genis Laval, France*
[8]*Max Planck Institut für extraterrestrische Physik, PO Box 1312, D-85478 Garching, Germany*
[9]*Gemini Observatory, Northern Operations Centre, 670 N. A'ohoku Place, Hilo, Hawaii 96720, USA*
[10]*Netherlands Institute for Radio Astronomy (ASTRON), Postbus 2, NL-7990 AA Dwingeloo, the Netherlands*
[11]*Kapteyn Astronomical Institute, University of Groningen, Postbus 800, NL-9700 AV Groningen, the Netherlands*
[12]*Max-Planck-Institute for Astrophysics, Karl-Schwarzschild-strasse 1, D-85741 Garching, Germany*
[13]*Centre for Astrophysics Research, University of Hertfordshire, Hatfield, Herts AL1 09AB*
[14]*Centre for Astrophysics and Supercomputing, Swinburne University of Technology, Hawthorn, Vic 3122, Australia*
[15]*Dunlap Institute for Astronomy & Astrophysics, University of Toronto, 50 St George Street, Toronto, Canada*
[16]*Department of Physics, New Mexico Institute of Mining and Technology, Socorro, NM 87801, USA*

Accepted 2012 October 30. Received 2012 October 30; in original form 2012 June 29

ABSTRACT

We analyse the morphological structures in galaxies of the ATLAS^{3D} sample by fitting a single Sérsic profile and decomposing all non-barred objects (180 of 260 objects) in two components parametrized by an exponential and a general Sérsic function. The aim of this analysis is to look for signatures of discs in light distributions of nearby early-type galaxies and compare them to kinematic properties. Using Sérsic index from single-component fits for a distinction between slow and fast rotators, or even late- and early-type galaxies, is not recommended. Assuming that objects with $n > 3$ are slow rotators (or ellipticals), there is only a 22 per cent probability to correctly classify objects as slow rotators (or 37 per cent of previously classified as ellipticals). We show that exponential sub-components, as well as light profiles fitted with only a single component of a low Sérsic index, can be linked with the kinematic evidence for discs in early-type galaxies. The median disc-to-total light ratio for fast and slow rotators is 0.41 and 0.0, respectively. Similarly, the median Sérsic indices of the bulge (general Sérsic component) are 1.7 and 4.8 for fast and slow rotators, respectively. Overall, discs or disc-like structures are present in 83 per cent of early-type galaxies which do not have bars, and they show a full range of disc-to-total light ratios. Discs in early-type galaxies contribute with about 40 per cent to the total mass of the analysed (non-barred) objects. The decomposition into

⋆ E-mail: dkrajnovic@aip.de
† Dunlop Fellow.

© 2012 The Authors
Published by Oxford University Press on behalf of the Royal Astronomical Society

Downloaded from http://mnras.oxfordjournals.org/ at European Southern Observatory on August 13, 2014

discs and bulges can be used as a rough approximation for the separation between fast and slow rotators, but it is not a substitute, as there is only a 59 per cent probability to correctly recognize slow rotators. We find trends between the angular momentum and the disc-to-total light ratios and the Sérsic index of the bulge, in the sense that high angular momentum galaxies have large disc-to-total light ratios and small bulge indices, but there is none between the angular momentum and the global Sérsic index. We investigate the inclination effects on the decomposition results and confirm that strong exponential profiles can be distinguished even at low inclinations, but medium-size discs are difficult to quantify using photometry alone at inclinations lower than $\sim 50^{\circ}$. Kinematics (i.e. projected angular momentum) remains the best approach to mitigate the influence of the inclination effects. We also find weak trends with mass and environmental density, where disc-dominated galaxies are typically less massive and found at all densities, including the densest region sampled by the ATLAS^{3D} sample.

Key words: galaxies: elliptical and lenticular, cD – galaxies: bulges – galaxies: kinematics and dynamics – galaxies: structure.

1 INTRODUCTION

Excluding those unsettled systems undergoing mergers, bright galaxies come in two flavours: with and without discs. This was recognized in the early part of the 20th century (Reynolds 1920; Hubble 1922, 1926; Jeans 1929; Hubble 1936) and today it is characterized as the Hubble sequence of galaxies (Sandage 2005, for a review). Recognizing where discs disappear on the sequence, however, is a much more difficult task as projection effects play a key role in our (in)ability to quantify their incidence. This is evident in the fact that the idea of S0 galaxies actually being similar to spirals, while present in the works of Spitzer & Baade (1951) and Sandage, Freeman & Stokes (1970), waited some 40 years after the appearance of the Hubble tuning fork to be qualitatively presented (van den Bergh 1976). The importance of the parallelism between the two sequences of late- and early-type galaxies for the understanding of galaxy structure was nearly ignored for decades. The parallelism between the two classes of galaxies was recently revived by our project, thanks to the use of integral-field stellar kinematics (Cappellari et al. 2011b, hereafter Paper VII), which allowed us to recognize discs even at low inclinations. This was followed a few months later by two independent photometric studies reaching the same conclusion (Laurikainen et al. 2011; Kormendy & Bender 2012).

In practice, there are three ways to look for discs in galaxies: by means of photometric or kinematic analysis, or by constructing dynamical models using both types of information. Dynamical models are often complex and typically rely on certain assumptions. One of these is an assumption on the shape, which could be a limitation if we are interested in quantifying structural components such as discs.

The photometric analysis is based on recognizing structural components of galaxies in their light distributions, while the kinematic analysis is based on recognizing features in the higher moments of the line-of-sight velocity distribution (i.e. the mean velocity, velocity dispersion). Stellar discs, which are the main topic of this study, are flattened structures in which stars move on orbits of high angular momentum, hence they should leave both photometric and kinematic traces. Next to their flattened shape, which is clearly recognizable only when viewed directly from a side, or edge-on, discs could be expected to have a specific distribution of light. Indeed, discs of late-type spirals were found to have exponential light profiles (Freeman 1970). In contrast, ellipticals and bulges of spirals were first fitted with an $R^{1/4}$ profile (de Vaucouleurs 1959; Kormendy 1977), but since the early 1990s the paradigm shifted towards describing these structures with a more general Sérsic (1968) $R^{1/n}$ law which provided a continuous parameter applicable across the Hubble sequence (e.g. Caon, Capaccioli & D'Onofrio 1993; Andredakis, Peletier & Balcells 1995; de Jong 1996; Graham et al. 1996).

Early-type galaxies, traditionally divided into ellipticals and S0s, are particularly interesting as among them the separation into objects with and without discs is ambiguous. Photometric analysis of their isophotes revealed that some do contain non-obvious discs (Bender et al. 1989), that these might be very common (Rix & White 1990), and that inclination effects misclassify S0s as ellipticals (Jorgensen & Franx 1994). A new way of searching for discs in early-type galaxies was found in the so-called *bulge-disc* decompositions (e.g. Kent 1985; Saglia et al. 1997; Scorza et al. 1998; D'Onofrio 2001). The essence of these techniques is that they attempt to separate the light contribution from a bulge (having an $R^{1/4}$ or an $R^{1/n}$ light profile) and a disc (having an exponential light profile). As disc-dominated galaxies are frequently made of more than just a bulge and a disc, and contain also bars, rings, ovals, nuclear discs and nuclear clusters, as well as of bulges which are not necessarily similar to elliptical galaxies (e.g. Kormendy & Kennicutt 2004), recent decomposition techniques allow for a more general description of sub-components (e.g. MacArthur, Courteau & Holtzman 2003; de Jong et al. 2004; Laurikainen et al. 2009; Weinzirl et al. 2009; Laurikainen et al. 2010; Kormendy & Bender 2012), as well as applying it on 2D spectra (Johnston et al. 2012).

The other way of looking for discs is by observing the kinematics of galaxies. As stars in discs rotate at large velocities, and as their motion is typically ordered, observing regular rotation similar to those expected from ideal thin discs implies that those systems are discs, contain discs, or are related to discs by evolution. Elliptical galaxies, or bulges that are similar to them, should not exhibit such ordered and simple rotations (e.g. Statler 1991; Arnold, de Zeeuw & Hunter 1994). Early studies of kinematics of early-type galaxies indeed pointed out there are differences between them (Davies et al. 1983; Bender, Saglia & Gerhard 1994), but to bring kinematic and photometric analysis to a comparable level it was necessary to wait for integral-field spectrographs (IFS) and 2D maps of stellar kinematics.

The benefits of such observations were clearly pointed out by the SAURON Survey (de Zeeuw et al. 2002) and ATLAS^{3D} project (Cappellari et al. 2011a, hereafter Paper I). Using velocity and velocity dispersion maps (e.g. Emsellem et al. 2004), it is possible

Downloaded from http://mnras.oxfordjournals.org/ at European Southern Observatory on August 13, 2014

to robustly classify early-type galaxies according to their global angular momentum, even though it is still a projected quantity (Cappellari et al. 2007; Emsellem et al. 2007). This study proposed a separation of early-type galaxies into fast and slow rotators based on a physical property more robust to the effects of the inclination, instead of the traditional elliptical/S0 separation which is based on the apparent shape. This point was taken further with the ATLAS^{3D} data which comprise observations of a sample of nearby early-type galaxies, volume limited and complete down to a magnitude of -21.5 in the K band. Using this statistical sample, Emsellem et al. (2011, hereafter Paper III) showed that 86 ± 2 per cent of ETGs are fast rotators and 14 ± 2 per cent are slow rotators. This separation agrees closely with a quantitative separation of the morphology of the kinematics maps (Krajnović et al. 2011, hereafter Paper II), supporting the robustness of the distinction between the two classes.

Furthermore, utilizing KINEMETRY (Krajnović et al. 2006), it is possible to quantify how well the velocity maps of early-type galaxies agree with those of ideal discs. Krajnović et al. (2008) and Paper II found that differences of only 2–4 per cent, between observed stellar velocity maps of early-type galaxies and maps of inclined discs, are typical for fast rotators, while velocity maps of slow rotators simply cannot be represented by those of ideal discs. This suggest that fast rotators as a class are indeed discs or at least disc-like objects, and this is the essence of the fast–slow rotators' separation used in Paper VII to set apart objects with and without discs and update the Hubble sequence accordingly. The fact that the presence, or lack, of discs differentiates fast from slow rotators is also confirmed though semi-analytical modelling. In Khochfar et al. (2011, hereafter Paper VIII), we show that selecting galaxies by disc fraction, where fast rotators are selected to have more than 10 per cent of mass in discs, semi-analytic model is able to reproduce the observed abundance of fast and slow rotators as a function of mass or luminosity.

Armed with these results on galaxies' internal kinematics, we now turn our attention to the photometric analysis of ATLAS^{3D} galaxies. We fit single Sérsic profiles to all ATLAS^{3D} galaxies and attempt to separate the light contributions into a general Sérsic and an exponential profile. It is generally assumed that exponential profiles can be associated with discs. This is applicable to spiral and edge-on S0s galaxies, where discs are obvious, but for a general early-type galaxy, seen at a random orientation, where a disc might be masked due to the projection, it is not obvious that the exponential profile is really related to a (hidden) disc. Put in another way, the existence of an exponential profile does not necessarily prove that the galaxy contains a disc. This was pointed out by de Jong et al. (2004) and Naab & Trujillo (2006), who suggest that the kinematic information is crucial for determining the disc nature of early-type galaxies. The purpose of this work is to quantify the incidence of exponential light profiles, make a link with the observed kinematics and investigate the difference between fast and slow rotators from the point of view of their light distributions.

In Section 2 we briefly outline the ATLAS^{3D} sample, relevant observations and define samples of galaxies used in this work. In Section 3 we present the method used for the parametrization of the light distributions and for the disc/bulge decomposition. In Section 4 we outline our global fits with a single Sérsic function. In Section 5 we show and discus the results, while in Section 6 we summarize the main conclusions of this work. A further discussion on the merits of the chosen method is presented in Appendix A, a comparison of our results with literature is in Appendix B and a table with the results is in Appendix C.

2 SAMPLE AND OBSERVATIONS

The ATLAS^{3D} sample and its selection are described in detail in Paper I. Briefly, ETGs were visually selected from a parent sample of objects in the Northern hemisphere ($|\delta - 29^\circ| < 35^\circ$, where δ is the sky declination), brighter than $M_K < -21.5$ mag and within a local volume of radius of $D = 42$ Mpc. The final sample contains 260 nearby early-type galaxies, which were observed with the SAURON IFS (Bacon et al. 2001) mounted on the William Herschel Telescope (WHT). The SAURON kinematics was introduced in Paper I, and we refer to that paper for details on the extraction, while the stellar velocity maps used here were presented in Paper II.

Photometric data of 258 galaxies were assembled from the Sloan Digital Sky Survey (SDSS) Data Release 7 (Abazajian et al. 2009) and from our own imaging with the Wide Field Camera (WFC) mounted on the 2.5-m Isaac Newton Telescope (INT). These data, their reduction and photometric calibrations are presented in Scott et al. (2013, hereafter Paper XXI). In this study we use the r-band imaging. We exclude two galaxies without SDSS or INT imaging from further analysis. We use the same zero-points and the photometric calibration as Scott et al. (in preparation).

In Paper II we showed that at least 30 per cent of galaxies in ATLAS^{3D} sample contain bars and/or rings. These systems obviously have more than two components, comprising at least a bulge, a bar, a ring (alone or in addition to the bar), and a disc. A two-component fit will not describe these systems well. Crucially, bars (and rings) are disc phenomena; they happen only if there is a disc in the first place. Therefore, we removed from the sample all galaxies showing clear bars (and/or large-scale rings), according to classification in Paper II. This reduced the number of galaxies for the decomposition analysis to 180. Included are 34 of 36 slow rotators (two slow rotators are actually barred galaxies), and 146 of 224 fast rotators, as classified in Paper III. It is, however, still possible that among the remaining galaxies there are barred systems or galaxies with more than two components. However, we perform the global one-component fits on all ATLAS^{3D} galaxies (258 galaxies with the SDSS or INT imaging). We caution the reader that in all statistical consideration throughout the paper we use the limited sample of 180 galaxies (no barred galaxies), unless stated otherwise. Specifically, in Section 5.1, which deals with the one-component Sérsic fits, we use the 258 galaxies of the ATLAS^{3D} sample.

3 DECOMPOSITION OF ONE-DIMENSIONAL PROFILES

3.1 One- or two-dimensional decomposition?

Parametric decomposition of light into various structural components is often done in two dimensions (e.g. MacArthur et al. 2003; de Jong et al. 2004; Allen et al. 2006; Benson et al. 2007; Gadotti 2009; Simard et al. 2009; Weinzirl et al. 2009; Laurikainen et al. 2010; Simard et al. 2011), as more information is available to constrain the parameters of the components. The extra information held in the original images (e.g. on ellipticity and position angle) may be diluted when deriving a 1D profile, and the analysis of 1D profiles may not use changes in the other properties to constrain the model parameters. This is important because, for example, while position angle can remain unchanged between the components, the ellipticity will generally differ; if a system is composed of a spheroidal bulge and a thin disc, there will be a marked change in the ellipticity as one of the components starts dominating over the other (e.g. Binney & Merrifield 1998, p. 217).

Downloaded from http://mnras.oxfordjournals.org/ at European Southern Observatory on August 13, 2014

Based on simulations, Byun & Freeman (1995), de Jong (1996) and Simard et al. (2002) argued that 2D decompositions are superior to those done in one dimension, and several algorithms, of which some are publicly available, have been developed with that purpose, such as GIM2D (Simard et al. 2002), GALFIT (Peng et al. 2002), BUDDA (de Souza, Gadotti & dos Anjos 2004; Gadotti 2008), GASPHOT (Pignatelli, Fasano & Cassata 2006, using a hybrid 1D/2D approach), GASP2D (Méndez-Abreu et al. 2008) and GALPHAT (Yoon, Weinberg & Katz 2011). A number of authors, however, continue to work in one dimension (e.g. Graham 2001; Aguerri & Trujillo 2002; Balcells et al. 2003; Blanton et al. 2003; Naab & Trujillo 2006; Fisher & Drory 2008; Fabricius et al. 2012; Kormendy & Bender 2012), while Courteau, de Jong & Broeils (1996) and MacArthur et al. (2003) argued that 1D decompositions should not be disfavoured as they give similar results as 2D fits, provided the data have high signal-to-noise ratios.

Our purpose here is to attempt to decompose and look for discs in a robust and homogenous way in both fast and slow rotators. To do this, we limit ourselves to considering only simple one- or two-component models. We therefore consider that the additional information gained in fitting 2D images is offering a negligible improvement while introducing significant additional complexity and computational effort. The high signal-to-noise ratio images and the large size of the ATLAS^{3D} galaxies ensure that extraction of the profiles can be done robustly. In the next section we present our method in detail, and in Appendix A we present additional considerations regarding the choice of our methods.

3.2 Method

1D light profiles were extracted by azimuthally averaging the light along the best-fitting ellipses obtained by means of an isophotal analysis (for an overview of other possibilities see Appendix A). The best-fitting ellipses were found using the method of KINEMETRY[1] (Krajnović et al. 2006), run in the *even* mode optimized for images. It this case, kinemetry reduces to the analysis of even moments of the line-of-sight velocity distribution (e.g. light distributions) and the methodology is similar to Jedrzejewski (1987) and the IRAF task ELLIPSE. For a given ring of radius r (semimajor axis length) and thickness Δr (which is a geometric function of r such that rings at larger radii are wider), the intensity $I(r)$ is sampled at equal intervals in the eccentric anomaly θ along a trial ellipse defined by the position angle PA, flattening $Q = b/a$, where a and b are the lengths of the semimajor and semiminor axes, respectively, and the centre (X_0, Y_0). The intensity $I(r, \theta)$ is expanded into a Fourier series and the amplitudes of the Fourier coefficients are minimized until a fit as close as possible to $I(r, \theta) = \text{const.}$ is achieved.

In practice, the centre of a galaxy was pre-determined as the centroid of the light distributions, obtained in the same way as the global photometric position angle and ellipticity in Paper II, and kept fixed during the analysis. Bright stars and companion galaxies were masked prior to the fit. Dust is not often seen in our galaxies, and we masked or excluded from fitting the most contaminated regions. Sky levels were estimated and subtracted from the images using a routine `sky.pro` available from the IDL Astronomy Library (Landsman 1993).

In addition to extracting along the best-fitting ellipses where PA and Q were allowed to vary freely, we also extracted a second set of profiles for which PA and Q were fixed to the global values from Paper II. These two sets of light profiles are used for different purposes: the set from the fixed ellipses for a global single-component fit (see Section 4) and the set from free ellipses for the decompositions as outlined below.

We use two different forms of the Sérsic (1968) fitting function to describe the components in the light profiles. The first one is a general $r^{1/n}$ model, often used to describe the surface brightness profiles (and images) of bulges or whole galaxies (e.g. Caon et al. 1993; Graham 2001; de Jong et al. 2004; Weinzirl et al. 2009; Hoyos et al. 2011):

$$I(r) = I_{\rm e} \exp\left\{-b_n\left[\left(\frac{r}{R_{\rm e}}\right)^{1/n} - 1\right]\right\}, \quad (1)$$

where $I_{\rm e}$ is the intensity at the effective radius $R_{\rm e}$ that encloses half of the light of the component, n is the parameter which describes the shape of the function, while b_n is dependent on n, and not an additional free parameter. It can be obtained by solving the equation $\Gamma(2n) = 2\gamma(2n, b_n)$, where Γ is the gamma function and $\gamma(2n, b_n)$ is the incomplete gamma function (Ciotti 1991). We use an accurate numerical approximation of $b_n = 2n - 1/3 + 4/(405n) + 46/(25\,515n^2)$ given in Ciotti & Bertin (1999). A number of useful mathematical expressions related to the Sérsic model are given in Graham & Driver (2005).

The other function is a special case of the Sérsic model when $n = 1$. In this case the model simplifies to an exponential function:

$$I_{\rm d}(r) = I_0 \exp\left(-\frac{r}{R_{\rm d}}\right) \quad (2)$$

where $I_0 = I_{\rm e}e^{b_n}$ is the central surface brightness, $R_{\rm d} = R_{\rm e}/b_n$ is the scale length and $b_n = 1.678$ for $n = 1$. This exponential form is usually used to define a disc component, as it reproduces well the outer light profiles of disc galaxies (Freeman 1970).

In this work we use two sets of parameters linked with equation (1), one for a single-component fit to the light profile, where the Sérsic function describes the total light, and another for a two-component fit to the light profile, where the general Sérsic function describes the bulge light (more precisely, light not belonging to the exponential component). In the former case, the parameters of equation (1) are: $I_{\rm e,tot}$, $R_{\rm e,tot}$ and $n_{\rm tot}$, and in the latter case: $I_{\rm e,b}$, $R_{\rm e,b}$ and $n_{\rm b}$. As will be seen later, after the decomposition of some galaxies it is evident that a sufficiently good fit is obtained using the general Sérsic component only (i.e. the decomposition and the exponential components are not necessary). In these cases, we will still refer to the parameters of the fit as the bulge parameters (e.g. $n_{\rm b}$), even though they describe the full galaxy, to differentiate it from the direct single-component fit. In spite of both being results of single-component fits, they are not necessarily equal, as will become apparent in Section 4.

We decompose the light profiles $I(r)$ of ATLAS^{3D} galaxies by assuming that $I(r) = I_{\rm e,b}(r) + I_{\rm d}(r)$, with $I_{\rm e,b}, R_{\rm e,b}, n_{\rm b}, I_0$ and $R_{\rm d}$ as free parameters. The fit is performed using `mpfit` (Markwardt 2009), an IDL implementation of the MINPACK algorithm (Moré, Garbow & Hillstrom 1980) of the Levenberg–Marquardt method. As more parameters will always provide a better fit to the data, to decide on whether a one-component model is sufficient to describe the galaxy, we use the following method. The same light profiles were fitted also using only the general $r^{1/n}$ Sérsic model (equation 1), within the same radial range. The root mean square (rms) of the residuals (within the fitting range) of these single-component fits ($\rm rms_1$) were then compared with the rms of the residuals of the

[1] An IDL implementation of kinemetry is available at this address: http://www.eso.org/∼dkrajnov/idl

Downloaded from http://mnras.oxfordjournals.org/ at European Southern Observatory on August 13, 2014

two-component fits (rms_2). If $\mathrm{rms}_1 > 1.5 \times \mathrm{rms}_2$ then the two-component fit was deemed better than the one-component fit, and its parameters were adopted. It is important to note that we visually inspected all residuals (both one and two components) as it is not only the rms what should be considered, but also the systematic changes in the correlated residuals visible as wiggles. In this respect, adopting a higher threshold value (e.g. $\mathrm{rms}_1 > 2 \times \mathrm{rms}_2$) does not change the results significantly, as long as one considers that the disappearance of the correlated wiggles is the prime evidence for the existence of multiple components (see Section 3.3 and Fig. 1 for more details and examples).

The total luminosity of the individual sub-components can be estimated as follows:

$$B(r) = \int_0^\infty I_{\mathrm{e,b}}(r) 2\pi q_\mathrm{b} r \, \mathrm{d}r = \frac{2\pi I_{\mathrm{e,b}} R_{\mathrm{e,b}}^2 \mathrm{e}^{b_n} n_\mathrm{b} q_\mathrm{b}}{b_n^{2n_\mathrm{b}}} \Gamma(2n_\mathrm{b}) \quad (3)$$

and for the case of an exponential disc,

$$D(r) = \int_0^\infty I_\mathrm{d}(r) 2\pi q_\mathrm{d} r \, \mathrm{d}r = 2\pi I_0 R_\mathrm{d}^2 q_\mathrm{d}, \quad (4)$$

where we assume that the flattening of the sub-components q_b and q_d does not change with radius. The flattening of a sub-component was determined as the flattening at the representative radius of the sub-component. For the sub-component described with an $R^{1/n}$ model this means $q_\mathrm{b} = q(R_{\mathrm{e,b}})$ and for the exponential $q_\mathrm{d} = q(R_\mathrm{d})$. Finally, we want to know what is the relative fraction of light contained in the exponential sub-component and we calculate 'disc-to-total' (D/T) ratio,[2] with the following expression: $D/T = D/(B + D)$, where D and B are the expressions from equations (3) and (4).

We also estimated the total luminosity within the radius R_max which corresponds to the largest coverage of our IFU observations (matching the coverage of our kinematics). This was done by integrating the integrals in equations (3) and (4) from $r = 0$ to $r = R_\mathrm{max}$ to estimate the bulge and disc light within these regions, respectively. In practice, for the bulge component we use equation (2) from Graham & Driver (2005) and apply the tabulated form of the integral in equation (4) (e.g. Gradshteyn et al. 2000, p. 357) for the exponential component. Depending on the coverage of the individual objects there are some modifications to D/T ratios, but none of the conclusions of this work changes if we consider this limited luminosity instead of the (standard) total luminosity. The main reason why this is the case comes from the fact that our IFU coverage is on average twice as large as R_b and R_d estimated in this study. In the rest of the paper we only consider the total luminosities defined by equations (3) and (4).

A number of studies discuss the robustness of the decomposition parameters (Schombert & Bothun 1987; de Jong 1996; MacArthur et al. 2003; Kormendy et al. 2009). We found that the crucial step of our fitting procedure is an adoption of the radial range within which the fit is done, and partially the initial conditions for the fit. We use one continuous range excluding the central parts influenced by the effects of seeing and running until the sky level. Scott et al. (in preparation) estimate that the average point spread function of our data has full width at half-maximum of 1.25 arcsec and as a rule we exclude a region twice as big (the fitted region starts at ∼2.5 arcsec, or ∼300 pc, assuming the average distance to ATLAS^{3D} galaxies). If necessary, and in a limited number of cases, both inner and outer radii for the fits were adapted for each galaxy individually (see Section 3.3).

[2] At this moment we call the exponential components a disc component without proof that this is applicable for all early-type galaxies. This is done by convention, but in Section 5.4 we address this issue in detail justifying our choice.

3.3 Decomposition examples

In Fig. 1 we show six example fits to light profiles extracted along the best-fitting ellipses. These include three profiles which can be reproduced with a single component of a low Sérsic index, and three light profiles which are reproduced with two components of various relative fractions. We also show residuals of both one- and two-component fits for comparison. These examples are representative of the fits to other galaxies in the sense of their quality, types of residuals, fitting ranges and types of models that reproduce the observed light profiles.

The residuals within the fitted range are generally small indicating good model fits; a median of the rms deviation is 0.05 mag arcsec^{-2} and its standard deviation is 0.03 mag arcsec^{-2}. On the top-left panel (NGC 3156), we show an example of a galaxy for which residuals of the two-component fit are not significantly smaller than the one-component fit residuals. Hence, the one-component fit was deemed sufficient, and the decomposition results were discarded. Contrary examples, when a two-component fit was considered necessary, are shown for NGC 4434, NGC 4623 and NGC 5198.

After carrying out similar comparisons for all galaxies and choosing if the decomposition is necessary, we examined all galaxies with rms > 0.1 mag (29 objects) to understand the reasons for the deviations. In only one case (NGC 4753), residuals could be connected with dust features, with a characteristically jagged distribution of values. In all other cases, the distribution of residuals was monotonically varying. These kinds of features suggest that there are possible additional components in the light profile, which cannot be described by the assumed decomposition in two components only.

Among the galaxies with high residuals, we found both those fitted with one component (16 objects) and with two components (13 objects). The majority (9/13) of galaxies fitted with two components have $\epsilon > 0.6$, and are often seen in disc-dominated systems close to edge-on. NGC 4623 from Fig. 1 is an example. We tested these cases by decomposing their light profiles obtained as major axis cuts, but there were no significant improvements to the two-component fits, nor was there any large difference in the parameters of the best-fitting components. The cause for the poor fits can be fully attributed to the existence of additional components, which could be interpreted as manifestations of instabilities (e.g. bars, rings) induced by secular evolution and hard to recognize due to the inclination angle.

On the other hand, systematic variations of residuals in galaxies with only one component might suggest that these galaxies are actually better fitted with two components and that our threshold criterion should not apply here. However, for nine (of 16) objects the fitting algorithm actually automatically excluded the two-component solutions and this result was robust to changes in both the initial conditions and fitting ranges. Additionally, only one (of 16) objects has $n > 3$, while for the majority (12/16) of the objects Sérsic index ranges from 0.8 to 1.2. These single components, near exponential galaxies, have additional structures, often seen in the shape of correlated wiggles in the residuals, but a two-component fit is not sufficient to describe them.

Inwards of the inner fitting range point (2.5 arcsec), one can often detect departures from the fitted and the observed light profiles. This trend is particularly visible in NGC 3156 and NGC 5322 of Fig. 1. The models either overpredict or underpredict the light in the centres of the galaxies. In some cases, these can be directly associated with

Downloaded from http://mnras.oxfordjournals.org/ at European Southern Observatory on August 13, 2014

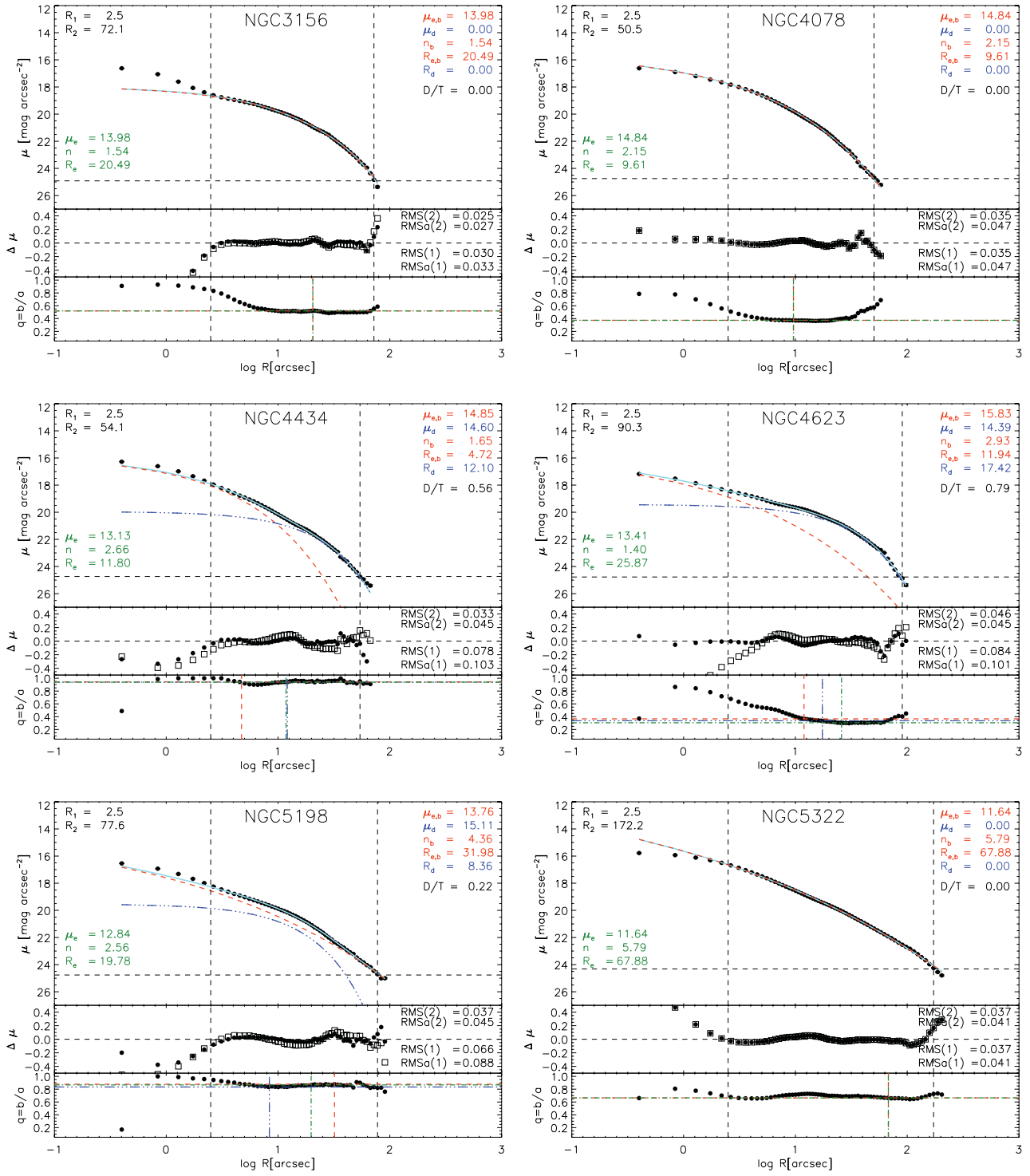

Figure 1. Decomposition examples. Each galaxy is represented by three panels, where top panel shows the extracted light profile, the middle panel shows the residuals (data − best-fitting model) in mag arcsec^{-2} and the bottom panel shows the flattening ($q = 1 - \epsilon$) profile extracted at the same time as the light profile. On the top panel the data are shown with solid symbols. Results of the two-component fit (the effective radius $R_{e,b}$, the bulge Sérsic index n_b, disc scale height R_d, the total light for both components, $\mu_{e,b}$ and μ_d, and the disc-to-total light ratio) are given in the upper-right corner. The results of the one-component fit (total light μ, Sérsic index n and effective radius R) are shown in the lower-left corner. Vertical dashed lines indicate the region used in the fit. The actual values in seconds of arc are given in the upper-left corner. These lines are also shown in the middle and bottom panels. The horizontal dashed line is our estimate of the σ of the sky level. Light profiles of the different components are shown with lines: red dashed line for the bulge model, blue triple-dot–dashed line for the exponential model and solid cyan for the combined fit. We do not show the one-component fit. In the middle panel solid symbols show residuals for the two-component fit and open squares show the one-component fit. The rms values for the fitted (RMS) and the full (RMSa) data range are shown in the upper- and lower-right corners for two- and one-component fits, respectively. In the bottom panel vertical red (dashed) and blue (triple-dot–dashed) lines correspond to the sizes of the bulge ($R_{e,b}$) and the exponential (R_d) components, respectively, and green (dot–dashed) line to the one component fit effective radius (R_e). The horizontal red and blue lines give the values of q used in equations (3) and (4), respectively.

Downloaded from http://mnras.oxfordjournals.org/ at European Southern Observatory on August 13, 2014

the excess/deficit observed within ETGs with the *Hubble Space Telescope* (*HST*) (Ferrarese et al. 1994; Faber et al. 1997; Graham et al. 2003; Ferrarese et al. 2006; Kormendy et al. 2009), or small nuclear components, but we do not attempt to quantify the effects as one generally needs higher spatial resolution for this analysis (e.g. the *HST* data) to allow fits that extend to smaller radii.

Finally, we note that our decomposition was performed on relatively shallow SDSS images focusing on morphological structures within a few effective radii. Deeper images are likely to show more varied structures at larger radii introducing a need for more than just two components to describe the light distributions of galaxies (e.g. Duc et al. 2011).

3.4 Uncertainties

As mentioned above, we obtain the best-fitting parameters by doing a linear least-squares fit with the `mpfit` routine. In doing so we assume constant relative errors, which ensures equal weighting to all points on our light profiles. To estimate the uncertainties to Sérsic parameters we perform Monte Carlo simulations based on the rms scatter of the residuals to the fit. We perturb original light profiles, fit them again 100 times and estimate the uncertainties as the standard deviation of the simulations. These are only statistical estimates of the uncertainties, and they do not properly represent the systematic ones coming from the choice of the method, initial condition, sky levels and, in particular, the choice of the fitting range. In Appendix A we discuss the systematic effects when using different methods outlined above. We caution the reader that these sources of the systematic uncertainties could drive the difference between our results and the literature results.

In Appendix B we present a comparison of our results (focusing on the Sérsic index and the D/T ratio) with the results of other studies. We compare our results both directly and in a statistical sense: first, with studies that analyse samples which overlap with our own (i.e. comparison of individual galaxies), and, secondly, with studies that analyse large numbers of galaxies. The reason for this approach is in the presence of large systematics (e.g. definition of the sample and fitting technicalities such as the fitting range or choice of one- over two-component fits) and absence of a similar to our own data set for which calculations were done in a comparable way (e.g. decomposition into free Sérsic and exponential components for a significant number of galaxies in common with this study). Our conclusion is, based on comparing individual cases, that there is a sufficiently good agreement with previous work, but that different types of above-mentioned systematics are the dominant factor for uncertainties.

4 SÉRSIC FITS TO ONE-DIMENSIONAL PROFILES

We also fitted a single-component Sérsic function to the light profiles of all ATLAS^{3D} galaxies with SDSS and INT imaging, in order to derive their global structural parameters, as it is often done with early-type galaxies (e.g. Caon et al. 1993; Graham et al. 1996; Trujillo et al. 2004; Ferrarese et al. 2006). After some testing, and contrary to our choice for the decomposition, we decided to fit azimuthally averaged light profiles obtained along fixed ellipses. Note that in Section 3.2, when we outlined the method for choosing whether a profile needs to be decomposed or not, we stated that we fitted both one and two components to the same light profile extracted along the best-fitting ellipses. We, however, do not think that these profiles are best suited for determination of the global parameters, and, hence, use profiles extracted along the fixed ellipse.

Our choice for fixed ellipse profiles is motivated by our wish to parametrize the whole galaxy with a single component. As shown by Erwin, Pohlen & Beckman (2008), multicomponent systems will have different light profiles depending on whether they are extracted along fixed or free ellipses. Our choice of fixing PA and Q is justifiable as we are fitting a single function to objects which are predominantly two or more component systems (see Section 5). For some objects, such as massive, triaxial slow rotators, the change in ellipticity or position angle is most likely not an indication of multiple components but of triaxiality or smoothly varying orbital structure. For these objects an approach with free ellipses could also be preferred. As there are, however, only a handful of such objects, we choose to fit a constant in PA and Q model, as for all other galaxies. As these galaxies typically do not warrant a decomposition (see Section 5.2), an interested reader can find in Appendix C the values for single-component fits obtained on light profiles extracted from free ellipses. Our choice is similar to what a typical 2D fitting algorithm does: the component used to fit the galaxy image has a fixed shape and orientation. We support our decision with a discussion in Appendix A.

The parameters of the ellipses (PA, Q) were taken from Paper II, which are global and measured at large radii (typically around 2–3 effective radii). As another difference from the approach outlined in Section 3, we performed the fits on all galaxies, including objects with bars and/or rings. Note that the PA and Q used are not related to bars because in Paper II we took care to obtain them at radii beyond these structures and, hence, in barred systems they describe the shape and orientation of host discs.

We fitted the light profiles in the same radial range as for the two-component fits with the general $r^{1/n}$ profile of equation (1). The results of the fits are the global Sérsic index $n_{\rm tot}$, effective radius $R_{\rm e,\,tiot}$ and the intensity $I_{\rm tot}$ at the effective radius. As can be expected, one-component fits have somewhat larger residuals than two-component fits. The median rms is 0.08 mag arcsec^{-2}, while the standard deviation is 0.05 mag arcsec^{-2}. If we exclude barred galaxies and compare the rms for only those objects for which we also performed the disc/bulge decompositions, the median rms drops to 0.06 and its standard deviation to 0.04 mag arcsec^{-2}.

5 RESULTS

5.1 Global structural parameters of ETGs

Results of the single Sérsic fits to all galaxies are presented in Fig. 2 and given in Table C1. In addition to division into slow and fast rotators (top panels), we split the sample by mass into two subsets similar in number using $M_{\rm dyn} = 4 \times 10^{10}\,{\rm M}_{\odot}$ as the divider (bottom panels), a value similar to the characteristic mass derived by Shen et al. (2003).

The mass is constrained by the ATLAS^{3D} integral-field kinematics, images used in this paper and the Jeans Anisotropic Models (Cappellari 2008). It is defined as $M_{\rm dyn} = L \times (M/L)_{\rm dyn}$, where L is the galaxy total luminosity and the mass-to-light ratio was obtained via dynamical models. This mass represents $M_{\rm dyn} \approx 2 \times M_{1/2}$ where $M_{1/2}$ is the total dynamical mass within a sphere containing half of the galaxy light. Given that the stellar mass dominates the mass inside $M_{\rm dyn}(r = r_{1/2})$, $M_{\rm dyn}$ provides a very good approximation (in median within 10 per cent) to the galaxy stellar mass (Cappellari et al. 2013b, hereafter Paper XV).

Downloaded from http://mnras.oxfordjournals.org/ at European Southern Observatory on August 13, 2014

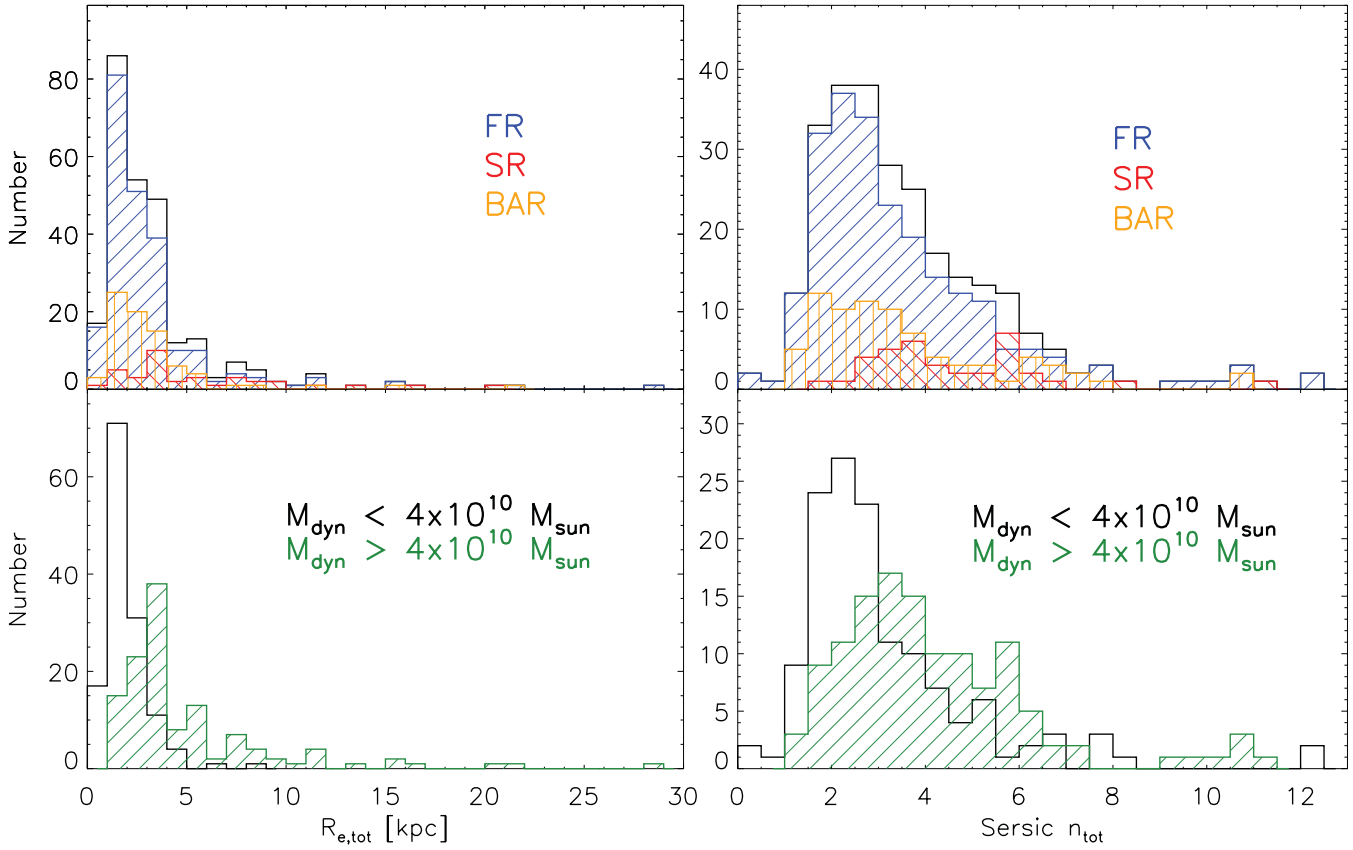

Figure 2. Distribution of the effective radius $R_{e,tot}$ (left-hand column) and the global Sérsic index n_{tot} (right-hand column) of single Sérsic fits to light profiles obtained averaging along fixed ellipses, for 258 ATLAS^{3D} galaxies. In the top row galaxies are divided into fast rotators (blue histogram hatched to the left), slow rotators (red histogram hatched to the right) and barred objects (orange histogram with vertical lines), while the open histogram is for all galaxies. In the bottom row, galaxies are divided in terms of mass into less massive (open histogram) and more massive (green hatched histogram) than 4×10^{10} $M_{\odot}$, which splits the sample into two roughly equal halves.

When mass is used as a proxy, there are clear trends in size (global effective radius of the Sérsic profiles) and the Sérsic index: high-mass galaxies are typically larger and have larger n_{tot}. However, when using this particular mass pivot point, the overlap between the values of the two samples is large.

When dividing galaxies into slow and fast rotators, there is a significant difference between the two classes based on these two parameters. A Kolmogorov–Smirnov (KS) test gives a probability of 10^{-5} and 10^{-4} that sizes and Sérsic n of fast and slow rotators are drawn from the same distribution, respectively. On the other hand, barred galaxies (Paper II) show a very similar distribution of sizes and Sérsic indices as other fast rotators. A KS test gives a 98 per cent probability that bars are drawn from the distribution of fast rotators, implying that a typical non-barred fast rotator will have the same size or Sérsic index as a barred galaxy.

Detailed comparisons with literature data are difficult due to various ways in which samples of early-type galaxies are selected (e.g. morphology, magnitude cuts or colour properties). However, in terms of the distribution of the Sérsic index, our results are in a reasonable agreement with previous studies of early-type galaxies (e.g. Caon et al. 1993), which found a large fraction of galaxies with $n_{tot} < 4$. A more detailed comparison can be found in Appendix B.

The main differences between slow and fast rotators is that distributions of both R_{tot} and n_{tot} are flatter for slow than for fast rotators. The latter show a peak in size at about $R_{e,tot} = 1.5$ kpc and a peak for Sérsic index at about $n_{tot} = 2$. Slow rotators do not display any specific peak, but their distributions are somewhat limited in the sense that there are no small galaxies (e.g. less than 1 kpc in effective radius) and the smallest n_{tot} is about 2. Furthermore, slow rotators are also found at the upper extremes of the size and Sérsic index distributions. It is noteworthy to mention that the low values in R_{tot} and n_{tot} among slow rotators occur for special kinematics, such as for galaxies with counter-rotating components.

The distribution of the Sérsic index n_{tot} in this sample of early-type galaxies is of special importance. Various authors use the Sérsic index to separate galaxies into discs and spheroids, or late- and early-type galaxies (e.g. Shen et al. 2003; Barden et al. 2005; McIntosh et al. 2005). The typical divide is taken to be $n_{tot} = 2$ or 2.5, but some authors separate galaxies into an exponential ($n_{tot} < 1.5$) and a concentrated ($n_{tot} > 3$) group[3] (e.g. Blanton et al. 2003), or use Sérsic indices as part of their classifications (e.g. Scarlata et al. 2007). If these values are adopted, about 21 per cent (using $n_{tot} < 2$), 34 per cent (using $n_{tot} < 2.5$) or 48 per cent (using $n_{tot} < 3$) of the ATLAS^{3D} galaxies would not be considered as early-type galaxies. As shown in Paper I, none of the ATLAS^{3D} galaxies has spiral arms or large dust lanes (across the full body when seen edge-on). However, as we argued in Papers II, III and VII, and as shown

[3] In the rest of the paper we will similarly use $n_{tot} = 3$ (or $n_b = 3$) to distinguish between galaxies with concentrated and non-concentrated Sérsic profiles.

Downloaded from http://mnras.oxfordjournals.org/ at European Southern Observatory on August 13, 2014

below, it is a fact that the majority of early-type galaxies are discs or strongly related to discs.

Furthermore, parametrizing with a single Sérsic function, and using any values of Sérsic index, is not sufficient to separate slow from fast rotators. It is true that only a few slow rotators have low $n_{\rm tot}$ values (and none of them has $n_{\rm tot} < 2$), and these might be special cases. However, there is a large number of fast rotators with Sérsic index value as high as that of more typical slow rotators. There are six slow rotators with $n_{\rm tot} < 3$ (out of 124 objects) and 104 fast rotators with $n_{\rm tot} > 3$ (out of 134 objects). These fractions give a probability of only 0.22 to classify an objects as a slow rotator if its $n_{\rm tot} > 3$. If we use the Hubble classification (data from HyperLeda, Paturel et al. 2003, see Section 5.5), one gets that a probability for classifying an elliptical if its $n_{\rm tot} > 3$ is 37 per cent (there are 50 of 134 galaxies with $n_{\rm tot} > 3$ classified as ellipticals).

Sérsic index alone cannot distinguish between slow and fast rotators (beyond saying that objects with $n_{\rm tot} < 3$ are most likely fast rotators), and hence does not sufficiently distinguish between two dynamically different classes of objects with likely different formation histories. This is an important caveat which should be kept in mind in all studies of large number of galaxies, or samples at large redshifts.

5.2 The decomposition results

In Fig. 3 we plot the results of our decompositions for non-barred ATLAS^{3D} galaxies following the procedure outlined in Section 3.2. The values are given in Table C1. The top panel shows D/T light ratios. Using Monte Carlo simulations we estimate the errors to D/T light ratios and find that a median uncertainty is 0.08 for cases where $D/T > 0$. Three main features are obvious: (i) 43 per cent of the analysed galaxies are in the first bin with $D/T < 0.05$, (ii) early-type galaxies show a full range of D/T ratios and (iii) there is an increase of galaxies around $D/T \sim 0.8$. We consider that the first bin ($D/T < 0.05$) contains galaxies with no exponential sub-components, hence, it is remarkable that more than half of all non-barred ETGs contain at least some evidence, and typically a significant amount, of light parametrized with an exponential component. This is perhaps not so surprising when considering the finding of Simard et al. (2009) that visually selected early-type galaxies can have low B/T ratios (or high D/T ratios in our notation).

Separating galaxies according to their angular momentum into fast and slow rotators reveals that the majority of slow rotators (71 per cent, or 24 of 34) actually have no exponential component, but six slow rotators (18 per cent, or six of 34 objects) have $D/T > 0.3$, and 10 (29 per cent) have $D/T > 0.1$. The latter value confirms the choice in Paper VIII to separate fast and slow rotators. In conclusion, the majority of slow rotators are early-type galaxies with no exponential components, while those that have an exponential component typically also have specific signatures of rotation. We will return to this issue in Section 5.5.

The middle panel of Fig. 3 shows the distribution of Sérsic indices of the bulge. There is a strong peak at low Sérsic indices and a long tail at larger values, and a bump between $n_{\rm b} \sim 4$ and 6. This protuberance is obviously caused by slow rotators, which predominantly lie between 4 and 6, and 76 per cent (26 of 34 objects) of slow rotators have $n_{\rm b} > 3$.

While the distribution of Sérsic indices for slow rotators is as expected ($n_{\rm b}$ is typically large), the distribution of $n_{\rm b}$ for fast rotators is more surprising. There are galaxies with large indices (about a quarter of fast rotators have $n_{\rm b} > 3$), and a fast rotator can have as large a Sérsic index as a slow rotator. The majority of fast rotators

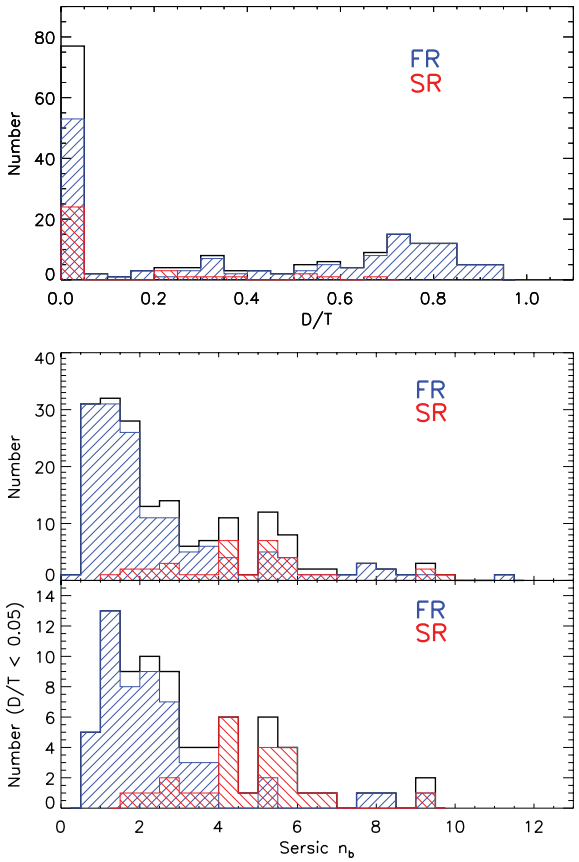

Figure 3. Distribution of disc-to-total light (D/T) ratios (top panel) and Sérsic n indices (middle and bottom panels) for non-barred ATLAS^{3D} galaxies. In all panels blue (right slanted) hatched histograms are for fast rotators and red (left slanted) hatched histograms are for slow rotators. The bottom histogram is made of galaxies in the first bin of the top panel (galaxies with $D/T < 0.05$).

(61 per cent, or 89 of 146 objects), however, have small indices ($n_{\rm b} < 2$) and the large indices are distributed in a long tail of the distribution. This comparison is only partially proper, as more than two-thirds of slow rotators are single-component systems, while this is true only for one-third of the fast rotators.

In the bottom panel of Fig. 3 we show the distribution of the Sérsic indices for all galaxies in the first bin ($D/T < 0.05$) of the top panel. We consider these galaxies to be made of a single component; the decomposition did not improve on the one-component fit significantly. There are 53 and 24 such fast and slow rotators, respectively. The distribution of $n_{\rm b}$ is again asymmetric with a peak at low values of the Sérsic index ($n_{\rm b} = 1$–3) and two peaks at larger values ($n_{\rm b} = 4$–6). As in the plot above, fast rotators make up the first peak and slow rotators the secondary bumps, with an overlap of a few galaxies in both directions, suggesting a clear difference in the structure of these two classes of early-type galaxies.

A most likely Sérsic index for a single-component fast rotator is between 1 and 2. This is remarkable, as not only more than half of fast rotators have a significant amount of light in an exponential component (e.g. 59 per cent, or 86 of 146, of fast rotators have $D/T > 0.2$), but also the majority of fast rotators, which can be described as single-component systems, have $n_{\rm b} < 3$ (79 per cent, or 42 of 53, of single-component fast rotators) and a profile similar to that of the exponential. There are 11 single-component fast rotators with $n_{\rm b} > 3$, of which four show prominent shells and tidal tails, and one

Downloaded from http://mnras.oxfordjournals.org/ at European Southern Observatory on August 13, 2014

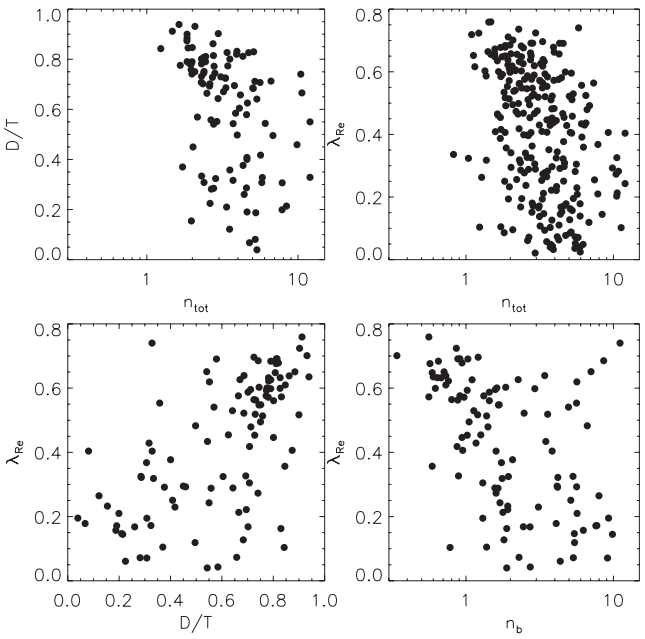

Figure 4. From left to right, top to bottom: correlations between D/T ratio and Sérsic index of the single-component fits, λ_R and Sérsic index of the single-component fits, λ_R and D/T ratio, and λ_R and Sérsic index of the bulge sub-component. In panels with D/T ratios and n_b, we show only those galaxies that required two-component fits (e.g. $D/T > 0$.)

is actually a prolate rotator. We will discuss these galaxies in more detail below.

5.3 Correlation between single Sérsic fits, the decomposition parameters and angular momentum

In Fig. 4 we show four diagrams with Sérsic index of the single-component fits, Sérsic index of the bulge sub-components, D/T ratio and angular momentum, λ_R, plotted against each other. The general conclusion is that there are no strong trends, except a general relation between D/T and λ_R. As it was reported previously (e.g. Gadotti 2009; Lackner & Gunn 2012), D/T (or rather bulge-to-total ratio[4]) ratio correlates poorly with the Sérsic index, of both global and of the bulge sub-component. We will discuss further the relations between D/T and n_b with λ_R in the next section. There is a weak correlation between D/T and λ_R, which is tighter for larger values of λ_R and high D/T ratios. In contrast, there is no significant correlation between λ_R and the Sérsic index of single-component fits, which confirms the finding of Section 5.1.

[4] Note that $B/T = 1 - D/T$ only if the decomposition was done into two components like here and, hence, a comparison with other studies that decompose galaxies into, for example, bulge, bar and discs might not be straightforward. We prefer to use D/T ratio, where D is associated with the exponential component, while bulges are an inhomogeneous set of objects with a range of Sérsic indices (for definitions of various types of bulges see Athanassoula 2005).

5.4 Exponential profiles in ETGs are discs

5.4.1 Morphological properties and angular momentum of early-type galaxies

As pointed out by de Jong et al. (2004) and Naab & Trujillo (2006), finding exponential components in the light profiles of ETGs does not imply that they correspond to discs. Combining the bulge/disc decomposition results with the stellar kinematics analysis, however, can elucidate the true nature of structural components of ETGs. Judging from Fig. 3 there is a clear separation between slow and fast rotators in their structural properties. To investigate in greater detail the relationship between kinematics and photometric structures we present in Fig. 5 two λ_R versus ϵ diagrams. In the left-hand panel we compare the amount of light in the exponential component, as quantified by the D/T ratio, and the Sérsic index n_b of the bulge component. In the right-hand panel we correlate the types of rotation found in our galaxies with the amount of light in the exponential component.

Looking at the left-hand panel of Fig. 5, and as seen in Fig. 4, galaxies with low Sérsic indices are typically found at high λ_R, while the fraction of galaxies with low D/T ratios is higher at low λ_R. There are some outliers, especially that galaxies with $D/T <$ 0.05 can be found also at larger λ_R. These objects, however, typically have a low Sérsic index, typically $n_b < 3$ (shown as ellipses). In contrast, objects with $D/T < 0.05$ at low λ_R (e.g. slow rotators) have typically higher Sérsic indices (>3). This division sets two extremes of early-type galaxies: those with low angular momentum and that are best described with a single Sérsic component of a high index, and those with high angular momentum, best described with two Sérsic components of a similar index or with a single Sérsic component of a low index.

Until this point we did not consider the detailed kinematic properties of our galaxies, except their global angular momentum. In Paper II we analysed our integral-field data by means of KINEMETRY, optimized for the mean velocity maps and divided the galaxies into five groups depending on their complexity. We plot these on the right-hand panel of Fig. 5, colour coding with the D/T ratios. Here we also separate galaxies best parametrized with single components of low Sérsic indices. This allows us to recognize that galaxies classified as non-rotators (group a) are single-component systems with high Sérsic indices. Galaxies showing featureless but non-regular rotation (group b) and kinematically distinct cores (KDCs; group c) are typically made of a single component with a high index, but in some cases low fractions of the exponential components can be attributed to their light profiles. Finally, galaxies made of two counter-rotating discs (2σ galaxies or group d) are mostly single-component systems of low Sérsic index, or have large D/T (>0.25) and low n_b (<3). In that respect they are structurally similar to group e, or galaxies with regular and most disc-like rotation, which are also characterized by low Sérsic indices and a range of D/T values. These include both single-component systems (of low Sérsic index) and systems with the highest contributions of the exponential light profiles.

5.4.2 V/σ–h_3 correlation

Next to kinematic information presented in Fig. 5 based on the angular momentum content and kinemetric analysis of the disc-like rotation in ATLAS^{3D} galaxies, we now use the information found in h_3, analogous to the skewness, the higher order moment of the line-of-sight velocity distribution (Gerhard 1993; van der Marel

Downloaded from http://mnras.oxfordjournals.org/ at European Southern Observatory on August 13, 2014

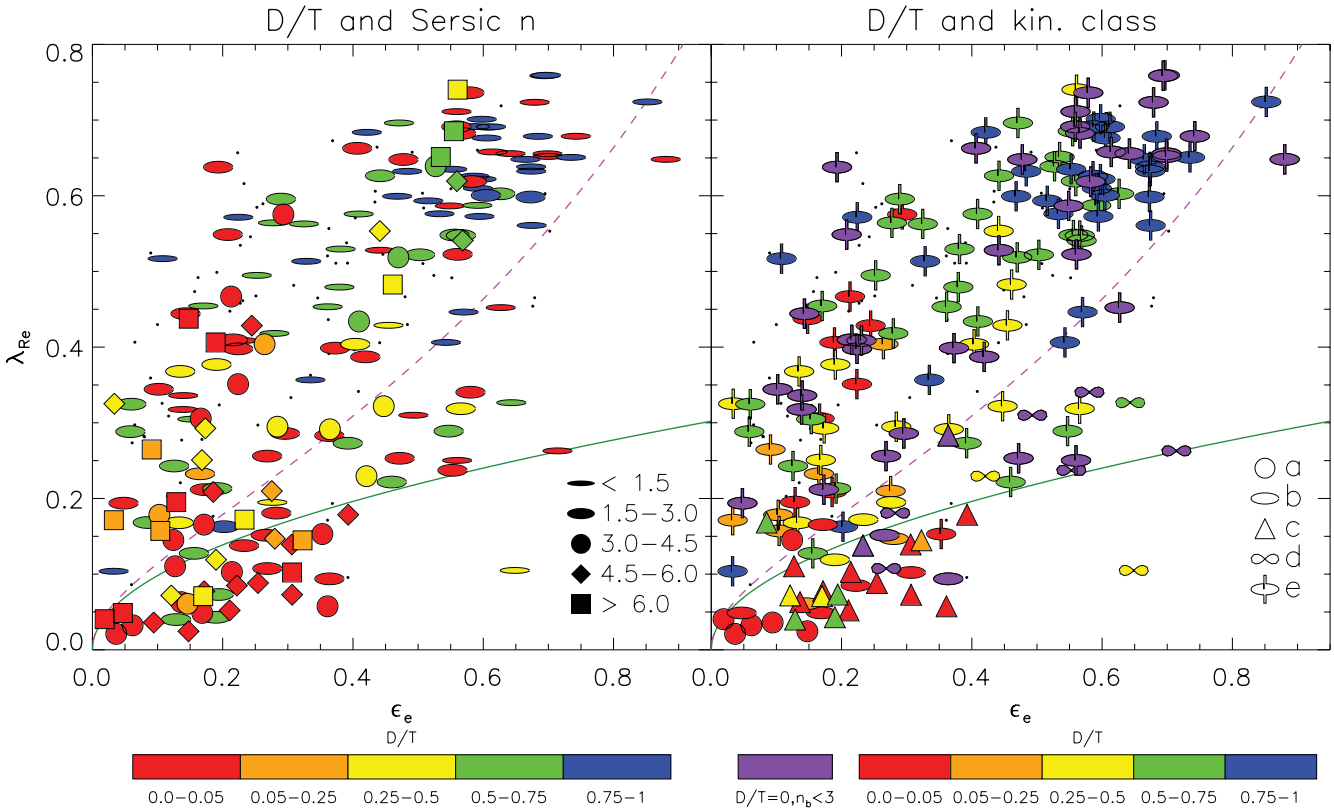

Figure 5. λ_R versus ϵ for ATLAS^{3D} galaxies. Barred galaxies not used for the decomposition are shown as small dots for completeness. Left: symbols represent Sérsic indices as shown in the legend, while colour coding quantifies the D/T ratio, as shown on the colour bar under the diagram. Right: symbols show different types of kinematics from Paper II and are described in the legend: (a) non-rotating galaxies, (b) featureless non-regular rotators, (c) KDC, (d) 2σ and (e) regular rotators. Colours again quantify D/T ratios, as shown on the colour bar, but now we also highlight those galaxies which do not have an exponential component, but have $n_b < 3$ (purple). The green line separates slow (below the line) from fast (above the line) rotators (Paper III). The dashed magenta line shows the edge-on view for ellipsoidal galaxies with anisotropy $\beta = 0.7\epsilon$, from Cappellari et al. (2007).

& Franx 1993). In Fig. 6 we show h_3 values against V/σ for all ATLAS^{3D} galaxies which we decomposed and for which we were able to measure this moment on individual spectra. We divided galaxies into those that are characterized by a single component of a large Sérsic index, those that have a low contribution of exponential components, those with a high contribution of the exponential components and galaxies of single components with small Sérsic indices. The first two classes are shown on the top panel (solid and dashed contours, respectively) and the second two on the bottom panel (solid contours) of Fig. 6.

There is an evident difference between the distributions on the two panels. Galaxies with high contribution of the exponential components show strong anticorrelation between h_3 and V/σ, which is often used as a kinematic manifestation of stellar disc kinematics, or at least evidence for stars at high rotational speeds (e.g. Bender et al. 1994). There is also a small difference between the two distributions on the top panel, as galaxies with single components (and large Sérsic indices) are dominated by $V/\sigma \sim 0$ values. In the bottom panel of this figure one can see that the tightest anticorrelation of h_3–V/σ is seen in single-component galaxies of small Sérsic indices.

The combination of various kinematic information and the decomposition results allows us to conclude that the rotation in early-type galaxies is typically associated with the presence of the exponential components in the light profiles. More specifically, the exponential profiles are only present when there is at least some indication of rotation, and galaxies in which the light is dominated by the exponential profiles are all galaxies with high stellar angular momentum. Furthermore, in cases where fits did not warrant the existence of exponential sub-components, but regular disc-like rotations are present and h_3 is anticorrelated with V/σ, the profiles are described by a single component of a small (<3) Sérsic index. This leads to a conclusion that any component with a Sérsic index less than about 3 can be associated with a disc, or is at least closely related to discs. The inverse is also true as galaxies with no detected rotation are typically single-component systems of high Sérsic indices.

5.4.3 *Similarities of fast rotators and spirals*

The existence of bulges of low n_b, a large range of D/T ratios, and a substantial fraction of objects with large D/T ratios in fast rotators confirms their similarity with spirals (e.g. Graham 2001; MacArthur et al. 2003; Weinzirl et al. 2009; Laurikainen et al. 2010), and strongly suggest an evolutionary link. Our results support the revision of the Hubble diagram put forward initially by van den Bergh (1976), which we revised to include fast and slow rotators in Paper VII (for photometric investigations see Laurikainen et al. 2011 and Kormendy & Bender 2012).

Additionally, the low values of Sérsic indices for the bulges of fast rotators are characteristic of central light concentrations built from

Downloaded from http://mnras.oxfordjournals.org/ at European Southern Observatory on August 13, 2014

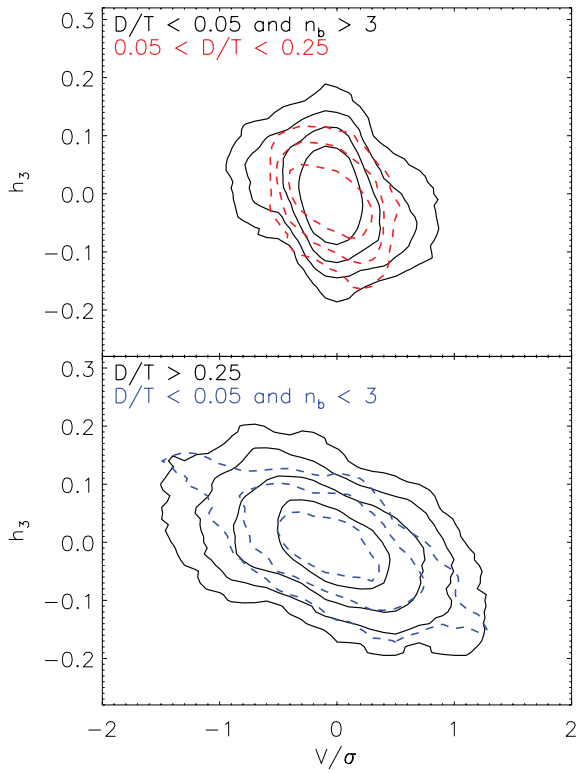

Figure 6. Local h_3–V/σ relation for every spectrum in galaxies with $\sigma >$ 120 km s^{-1} and an error on $h_3 < 0.05$. The contours show distribution of values in bins of 0.1 in V/σ and 0.01 in h_3, smoothed with a boxcar filter of a window of 2 pixel in both dimensions. The contour levels decrease in step of 0.5 in log from 2 for the smallest contours. Top: solid contours show the distribution of values for galaxies described by a single component of a high Sérsic index and dashed (red) contours show galaxies with low D/T fraction. Bottom: solid contours show the distribution for galaxies with substantial disc fractions, while dashed (blue) contours show values for galaxies described by single components of a low Sérsic index.

discs (e.g. discy-bulges; Kormendy 1993; Athanassoula 2005).[5] We remind the reader that we did not analyse barred galaxies and that our sample is devoid of spirals (and late-type galaxies in general). Also we have excluded from the fitting the central regions, while including higher resolution images could have an effect of decreasing the Sérsic index (e.g. Balcells et al. 2003). Nevertheless, it is clear from Figs 3 and 5 that bulges of low Sérsic index are typical among fast rotators and that their kinematics are disc-like, linking further the properties of early- and late-type galaxies. Similar results were reported recently by Fabricius et al. (2012) for S0s and late-type galaxies. It is, however, also evident in Fig. 5 that there are fast rotators with disc-like kinematics and with bulges of high Sérsic index, as well as fast rotators which are sufficiently well described with single components of low Sérsic indices.

[5] These are sometimes referred to as pseudo-bulges (e.g. Laurikainen et al. 2007; Fisher & Drory 2008) in order to highlight their structural and presumably evolutionary differences from the classical bulges (Kormendy & Kennicutt 2004). We, however, find this terminology unnecessarily confusing as it encompasses structures with various morphologies, scales and potential origins.

5.4.4 Masses of discs

Using dynamical masses from Paper XV, we can estimate the mass fraction in the exponential components. In the calculation we assume that there is no difference in stellar populations between the bulge and the exponential components and that galaxies are well fitted by a single mass-to-light ratio in the dynamical models. With this caveat in mind and selecting galaxies with $D/T > 0.05$, we find that the total mass in the exponential components is $\sim 4.12 \times 10^{12}$ M$_\odot$, or 27 per cent of the total mass of investigated galaxies. Selecting galaxies with $D/T < 0.05$ and $n_b < 3$ gives the total mass of 2.10×10^{12} M$_\odot$ or 14 per cent of the total mass of investigated galaxies. Combining these two figures we find that ∼41 per cent of stellar mass in early-type galaxies is in discs or disc-like components. The rest is shared mostly between single-component slow rotators and bulges of fast rotators. Note that we did not include here the contribution of the barred galaxies.

5.5 Decomposition and classifications of early-type galaxies

5.5.1 Hubble types and angular momentum

In Fig. 7 we repeat the λ_R–ϵ plot, with symbols differentiating between galaxies classified as ellipticals and S0s using morphological types from the HyperLeda catalogue (Paturel et al. 2003). In Paper III we commented on the discrepancy between E/S0 and fast/slow rotator classifications. Here we want to compare our decomposition results with both of these approaches, and with solid

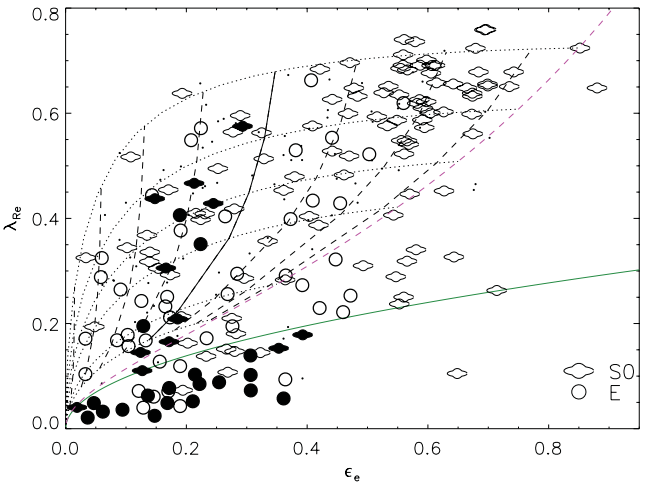

Figure 7. Distribution of elliptical (morphological type $T < -3.5$) and S0 (morphological type $T > -3.5$) galaxies in λ_R versus ϵ diagram, as in fig. 8 of Paper III. Solid symbols show ellipticals and S0s which are best fitted with a single-component Sérsic function of a large index ($n > 3$), and a decomposition of their profiles was not deemed necessary. As in Fig. 5, the green line separates the slow (below the line) from the fast (above the line) rotators (Paper III), the dashed magenta line shows the edge-on view for ellipsoidal galaxies with anisotropy $\beta = 0.7\epsilon$ from Cappellari et al. (2007), and dots are not-analysed barred ATLAS^{3D} galaxies. The dotted lines correspond to the location of galaxies with intrinsic ellipticities between 0.25 and 0.85 in steps of 0.1. The dashed lines show the location of galaxies originally on the magenta line as the inclination is varied in steps of 10°, decreasing from the magenta line (90°) to the left. As a guide line, the line that was plotted solid corresponds to an inclination of 50°. The formulas to plot these lines can be found in Cappellari et al. (2007).

Downloaded from http://mnras.oxfordjournals.org/ at European Southern Observatory on August 13, 2014

symbols we plot those galaxies which are sufficiently well described with a single Sérsic profile of a large index ($n_b > 3$).

There are 31 galaxies with that property, of which 20 are slow rotators and 11 are fast rotators. As fractions of the analysed slow and fast rotators, these galaxies make up 59 and 7 per cent, respectively. Based on their morphological classification, ellipticals best fitted with single-component profiles of a large index are typically found under the green line defining the slow rotator class. In contrast, among the fast rotators, objects with the same structural properties are typically classified as S0s. Concentrating on the $\lambda_R > 0.25$ region, there are such seven galaxies, two classified as ellipticals (NGC 0680 and NGC 4486A) and five as S0s (NGC 2695, NGC 4753, NGC 4459, NGC 5869 and NGC 3182, in order of decreasing λ_R). NGC 0680 is characterized by having evidence for a major merger, with a series of shells, arcs and two plumes rich in H I (Duc et al. 2011, hereafter Paper IX). A similar shell-like structure is also visible in NGC 5869 and in NGC 4753. Although these galaxies have significant and ordered rotation in their inner regions, the outer regions seem not to be fully relaxed, possibly having multiple structural components which are no better described with two components than with one component. The light profile of NGC 4486A is unfortunately contaminated by a bright star, nearly co-spatial with the nucleus of the galaxy, and we moved the inner fitting limit out to 5 arcsec, which is comparable to the effective radius of this galaxy, and the fit is likely not robust. Other S0 galaxies either have dust (NGC 4459 and NGC 4753) or show significant wiggles in their profiles (NGC 2695, NGC 3182), which are not removed with a two-component fit.

Light profiles of fast rotators with $\lambda_R < 0.25$ are different from the above-mentioned galaxies. The four galaxies characterized by single components of high Sérsic indices in this region are NGC 3607 (S0), NGC 3193 (elliptical), NGC 5485 (S0) and NGC 3073 (S0). All galaxies except NGC 5485 do not show strong evidence for an exponential profile. A blind decomposition assigns between 0.03 and 0.08 of the light fraction to an exponential profile, but the fits are barely improved with respect to one-component fits. All four galaxies are somewhat special, but NGC 5485 is the most intriguing one as this is one of the two galaxies in the entire ATLAS^{3D} sample which shows a prolate rotation (around its major axis), coinciding with a dust disc in a polar configuration.

Below the green line, most interesting are the galaxies that can be decomposed or have one component with a low Sérsic index. There are 14 such objects (NGC 4168, NGC 3608, NGC 5198, NGC 4458, NGC 5813, NGC 3414, NGC 7454, NGC 4191, NGC 4559, UGC03960, PGC050395, NGC 1222, PGC28887 and NGC 4690, in order of increasing λ_R), seven classified as S0 and seven as Es. The profiles for these galaxies, except NGC 4191 and NGC 7454, require a significant fraction (>0.2) of the exponential components in their lights. NGC 4191 and NGC 4550 are 2σ galaxies, and their low Sérsic indices are consistent with these galaxies being made of counter-rotating discs (Rix et al. 1992; Rubin, Graham & Kenney 1992; Cappellari et al. 2007; Coccato et al. 2011). NGC 7454 and NGC 5198 are galaxies with non-regular but featureless kinematics. Atypically for slow rotators, NGC 5198 and UGC03960 have H I gas, in both cases in peculiar configurations (Serra et al. 2012, hereafter Paper XIII). The last five galaxies in this list are found close to the green line, and they are likely to be transitional objects in terms of λ_R. The other five galaxies have KDCs and possibly the exponential profiles could be associated with the stellar distributions forming the KDCs.

5.5.2 *A transitional region in λ_R*

There seems to exist a transitional region between fast and slow rotators, and it can be broadly put to be in the range $0.1 < \lambda_R < 0.25$. Almost all galaxies above this region can be considered disc-dominated galaxies or at least galaxies with significant disc fractions. Below this region galaxies are typically, with a few exceptions, single-component systems of high Sérsic index. Within the region, however, there is a mix of objects, fast rotators with no significant fraction of light and slow rotators with a significant fraction of light in exponential components.

This region was also highlighted in the study of binary mergers by Bois et al. (2011, hereafter Paper VI). There we found that slow rotator remnants of binary mergers (of 1:1 and 1:2 mass ratios) are typically found below this region. Above the region, however, is the area populated by fast rotator remnants of binary mergers, whose progenitors were on prograde orbits (prograde or retrograde motion of the main progenitor has a strong influence on the dynamical structure of the remnant). The transitional region itself is also populated by merger remnants, but this time remnants of re-mergers of galaxies lie above or below this region (see fig. 11 in Paper VI). Although these were non-cosmological mergers, their results highlight that this region will likely contain galaxies with special dynamical structures.

Furthermore, part of this region is populated by galaxies seen at low inclination, while their edge-on projections are on the dashed magenta line in Fig. 5 (see fig. 1 of Paper III for the illustration of the projections in λ_R–ϵ diagram). This means that galaxies in this region could be a mix of two populations, oblate galaxies with discs projected at low inclinations and remnants of major mergers. In this respect the varied properties of light profiles of galaxies are no more surprising than their varied kinematic properties, and one could expect more surprises from galaxies in this region.

5.5.3 *Hubble types, angular momentum and decomposition results*

In Table 1 we list the median values and the standard deviations of Sérsic indices and D/T ratios, splitting the analysed galaxies into ellipticals and S0s, fast and slow rotators, as well as the combination of the two classification: fast-rotating ellipticals (E FR), fast-rotating S0 (S0 FR), slow-rotating ellipticals (E SR) and slow-rotating S0s (S0 SR). In terms of the decomposition parameters, both classifications give similar results, but fast–slow division highlights more

Table 1. Median values and standard deviation of Sérsic indices and D/T ratios for galaxies as classified by apparent shape or angular momentum.

Classification (1)	$\overline{D/T}$ (2)	$\sigma_{D/T}$ (3)	$\overline{n_b}$ (4)	σ_{n_b} (5)
E	0.19	0.29	3.8	2.2
S0	0.37	0.39	1.4	1.0
SR	0.00	0.16	4.8	1.9
FR	0.41	0.36	1.7	1.3
E FR	0.32	0.28	2.7	2.1
S0 FR	0.58	0.43	1.4	0.8
E SR	0.00	0.14	5.1	1.7
S0 SR	0.00	0.19	4.1	2.4

Note that a number of galaxies are single-component systems with $D/T = 0$. In these cases n_b was the Sérsic index of the single component.

Downloaded from http://mnras.oxfordjournals.org/ at European Southern Observatory on August 13, 2014

the differences between the objects with higher and lower D/T ratios and Sérsic indices than the standard Hubble classification. This is enhanced if we sort ellipticals and S0s depending on their angular momentum content. We can see that slow-rotating ellipticals and S0s are structurally very similar, while fast-rotating ellipticals and S0 show a certain range of properties, but they are rather very different from their slow-rotating counterparts. As general conclusion of this section, based on Fig. 7 and Table 1, we stress that results of the decomposition are more closely related to the fast–slow classification. They could be used to improve on the standard Hubble classification, but they cannot be used as a substitute for the kinematic classification.

As a guideline, when stellar kinematics is not available, we recommend to use the following combination of criteria to select tentative fast and slow rotators: a $D/T > 0.05$ (a $D/T > 0.1$ is also acceptable, depending on the confidence of the decomposition) for galaxies which need to be decomposed in (at least) two components, and $n < 3$ for galaxies not requiring a decomposition. We stress that with this selection one can misclassify up to 40 per cent of slow rotators.

The large spread of possible values for D/T ratios when elliptical/S0 classification is used, as well as for fast rotators, is likely a manifestation of the inclination effects. In addition, the semi-analytic models of Paper VIII suggest that there are differences between fast rotators. In particular, there is a range of D/T ratios (as we confirm in Section 5.2), where those with small ratios are likely to grow discs via cold accretion flows or grow bulges via minor mergers, while fast rotators with large D/T have exhausted their gas reservoirs (and cannot replenish it) and live in dense environments resembling passively evolved spirals. In the following two sections we address these two issues, by investigating the influence of the inclination on our results and looking for differences among fast rotators.

5.6 Inclination effects

The change of D/T ratios or values of n_b from the top-right (mostly blue) corners of the panels in Fig. 5 to the bottom-left (orange and red) corners could be caused by inclination effects. This is expected as ellipsoidal galaxies viewed edge-on, and having an anisotropy as found in Cappellari et al. (2007), lie on the dashed magenta line. Their projections due to varying inclinations are found to the left of this line (see Fig. 7), within the region inhabited by the majority of fast rotators, where the changes in D/T and n_b are the most obvious. Given the known effects of the inclination on the ability to find discs in model galaxies (e.g. Rix & White 1990; Gerhard & Binney 1996), we can also expect that finding discs using the decomposition method will be affected as well. In order to gain a qualitative understanding of the effects of the inclination on the decomposition parameters we performed the following test.

We selected two galaxies (NGC 4621 and NGC 5308), a galaxy with a weak and a strong disc (and small and large D/T ratios), respectively, which can be reasonably assumed to be close to edge-on. We used the Multi-Gaussian Expansion (MGE) method (Monnet, Bacon & Emsellem 1992; Emsellem, Monnet & Bacon 1994) as implemented by Cappellari (2002) to parametrize their light distributions as a series of 2D Gaussians. Assuming that the galaxies are seen edge-on, the MGE models specify the intrinsic shapes of these galaxies. The models were projected at a series of inclinations. Each of these models was then analysed in the same way as the original images: we extracted an azimuthally averaged light profile (letting the ellipse parameters free during the fit) and fitted the light profile as described in Section 3.2 with a general Sérsic and an exponential component.

Table 2. Inclination effect on the parameters of the decomposition.

Name (1)	Inclination (2)	D/T (3)	n_b (4)	R_e (5)	R_s (6)
	10	0.72	1.56	3.1	19.8
	20	0.73	1.49	4.6	19.9
	30	0.74	1.45	4.7	19.7
NGC 5308	40	0.77	1.39	4.6	19.3
	50	0.79	1.33	4.4	19.0
	60	0.82	1.24	4.2	18.5
	70	0.85	1.10	3.9	18.0
	90	0.88	0.87	3.5	17.3
	10	0.17	6.0	58.5	30.8
	20	0.20	5.6	49.4	31.8
	30	0.17	5.9	56.7	29.9
NGC 4621	40	0.17	5.7	54.7	29.4
	50	0.18	5.6	52.3	28.8
	60	0.25	5.0	39.0	30.4
	70	0.27	4.8	35.3	30.7
	90	0.33	4.4	29.3	31.2

In Table 2 we list the parameters of the decompositions of our MGE models. The results of this idealized analysis are that although there are some changes in the recovered parameters, they are systematic, but not large. The D/T fraction decreases as the viewing inclination approaches the face-on orientation, but the amplitude of the change is relatively small. In addition, the change of n_b and the sizes of the two components are also increasing, where the increase is more pronounced for the models with the smaller disc.

The changes of the model D/T and n_b with inclination can account for a change of at most 20–25 per cent in D/T and 1–1.5 in n_b in Fig. 5. The reason for this is likely in the systematics associated with the decomposition of the profiles. We illustrate this with Fig. 8, where we show the radial profiles of the surface brightness, ellipticity and the disciness parameter (e.g. Bender et al. 1989, we plot the Fourier term, a_4/a_0, associated with the $\cos(4\theta)$ harmonics, normalized by the intensity), for our two model galaxies seen at different inclinations (we show every other inclination for clarity).

Looking at the edge-on case (90°) of the NGC 5308 model, the disc component is clearly visible as a bump in the surface brightness profile at about $\log(R) = 1.3$. The same bump is clearly associated with the rise in ellipticity and high a_4/a_0 which measures the disciness. At this inclination we can be sure that the recovered parameters indeed describe a disc. As the inclination decreases, the profiles also change. Ellipticity and disciness show a dramatic change, while the surface brightness changes less prominently, but the bump in the profile steadily decreases. These same changes are also visible for the models of NGC 4621, but the differences at various inclinations are much smaller.

As demonstrated by Rix & White (1990), the disciness parameter loses its usefulness below an inclination of 50°–60°. The differences in ellipticity between a bulge and a disc, if they existed in the first place, are erased below an inclination of 30°–40°. The only signature of a disc, or, to be more precise, a necessity for another component, is visible in the light profile of the model such as NGC 5308. The light profiles of the NGC 4621 model, which had a relatively small disc, become less curved as the inclination decreases, and offer less hints for a need of a disc. In this model, below an inclination of 70° there is basically no clear photometric evidence for a disc. Our

Downloaded from http://mnras.oxfordjournals.org/ at European Southern Observatory on August 13, 2014

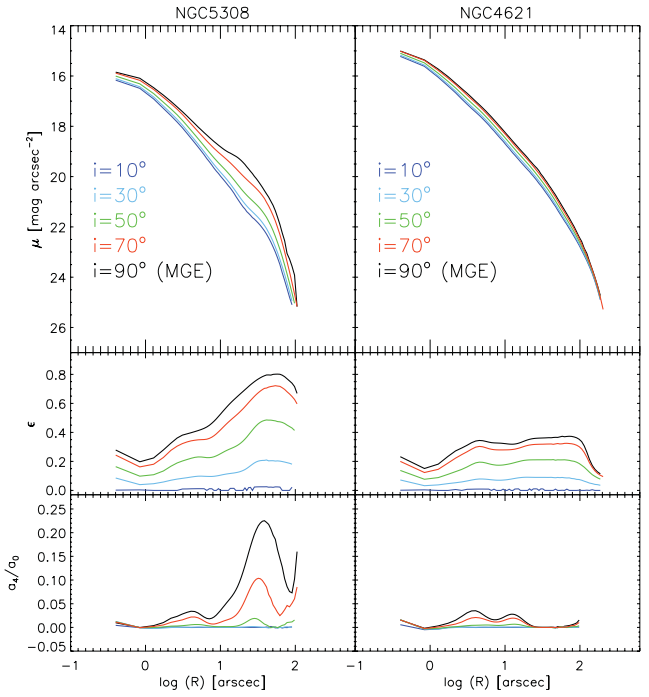

Figure 8. Top to bottom: surface brightness, flattening and disciness radial profiles for model galaxies with different fractions of light in the exponential components. Left to right: MGE models and their projections at 70°, 50°, 30° and 10° are based on NGC 5308 ($D/T \sim 0.8$) and NGC 4621 ($D/T \sim 0.35$). These galaxies were chosen as they are seen close to edge-on and the intrinsic MGE model is considered to be seen at 90°. Colours on all panels correspond to models projected at different inclinations, as shown in the legend. Note that as the inclination decreases, the profiles of the corresponding model also decrease in the maximum amplitude.

results are in agreement with Gerhard & Binney (1996), who also note that only strong discs are visible at low inclinations.

These examples show the dramatic effect of the inclination on the photometry and the observed shape of galaxies. Unless the disc is the dominant component, it will not be possible to recognize it below a certain inclination (∼50°). A decomposition method might recover a certain amount of the disc at a low inclination in a galaxy such as represented by our model of NGC 4621, but the confidence that this model could really be distinguished from a single-component model, or that the exponential is really needed, is generally low.

This should be taken into account when judging the decomposition results, including those presented here. Below an inclination of 50°, the photometric evidence for discs disappears and this might explain the large fraction of galaxies classified as ellipticals among fast rotators left of the line corresponding to this inclination (and above the magenta line) in Fig. 7. It can also be used to explain why fast rotators with single component of high Sérsic index are also found left of that line. Kinematic signatures of discs are more robust with respect to the changes in inclinations. The disc-like kinematics, found in nearly oblate axisymmetric objects (as well as bars) is visible at inclinations of 20° or even less (Krajnović et al. 2008). Complex kinematics, on the other hand, is a clear signature that the mass distribution is not favourable for the existence of discs.

5.7 Two types of ETGs with discs

The incidence of discs among slow rotators, large ranges of D/T ratios and Sérsic indices (both n and n_b) among fast rotators suggest that there are sub-populations present among these galaxies. Additionally, different types of fast rotators are predicted by the semi-analytic models (Paper VIII). In this section we explore this by dividing galaxies into three bins, using both kinematic and photometric information on the disc components. The galaxies in the three bins can be described as having *no discs*, *intermediate discs* or *dominant discs*. Following the results of Sections 5.2 and 5.4, the selection of bins is made by requiring that galaxies have:

(i) *No discs*: those slow rotators with $D/T < 0.05$, $n_b > 3$ and not 2σ galaxies. This selection yields 20 objects (only slow rotators).

(ii) *Intermediate discs*: those slow rotators which have $0.05 < D/T < 0.5$ or those that have $D/T < 0.05$, but $n_b < 3$, or those fast rotators which have $D/T < 0.5$ and $n_b > 3$. No 2σ galaxies are taken in this bin. This selection yields 36 objects, including nine slow rotators.

(iii) *Dominant discs*: those slow and fast rotators with $D/T > 0.5$, or those fast rotators with $D/T < 0.5$ but $n_b < 3$, and all (both fast and slow rotators) 2σ. This selection yields 124 objects, including five slow rotators.

The *no disc* bin comprises slow rotators which do not have any signature (neither in the kinematics nor in the photometry) of disc-like components, and it is the most conservative estimate for non-existence of discs in early-type galaxies. We required $n_b > 3$ (actually, for these galaxies n_b is the global Sérsic index, as they are all best fitted with a single component) to remove the few galaxies with low Sérsic index. As 2σ galaxies are made of two counter-rotating discs, or at least of two flattened families of counter-rotating orbits of high angular momentum (for detailed dynamical models of 2σ galaxies see Cappellari et al. 2007), these galaxies should be considered to have large disc contributions, even though their kinematics are not disc-like. Therefore, we also removed all slow rotator 2σ galaxies.

The *intermediate discs* contain all galaxies which have some indications of discs, but these discs do not dominate the total light. This bin collects most of the slow rotators of typically higher λ_R (for the range of λ_R found among slow rotators, see open symbols in Fig. 7), and those fast rotators that have relatively small exponential discs and bulge components of high Sérsic indices. The reason for this requirement is that a system with a bulge component fitted by a low Sérsic index next to an exponential disc could be approximated as a double disc system or at least as being made of two disc-like components and should be excluded from this class. Again, no 2σ galaxies are taken in this bin.

Finally, the *dominant discs* bin gathers all remaining galaxies, including all remaining slow rotators with strong photometric disc contribution, all 2σ galaxies, and all fast rotators which have either $D/T > 0.5$ or $D/T < 0.5$ and $n_b < 0.3$, for the same reason as explained in the previous paragraph. Given the previous results, it is not a surprise that most of our galaxies indeed fall in this group.

We did not include barred galaxies as they were not analysed in this paper. However, if we were to include barred and ringed systems, it is likely that they would be split between *dominant discs* and *intermediate discs*, stronger barred systems probably contributing to the latter. In Fig. 9, which summarizes the results of this section, we include barred galaxies in a separate bin for comparison with other three bins defined above.

In Fig. 9, we present the mass and environment dependence for ATLAS^{3D} galaxies. We used mass estimates from Paper XV, and the density estimator from Paper VII (see Section 5.4.4). As a measure of the environment, we use the volume density in

Downloaded from http://mnras.oxfordjournals.org/ at European Southern Observatory on August 13, 2014

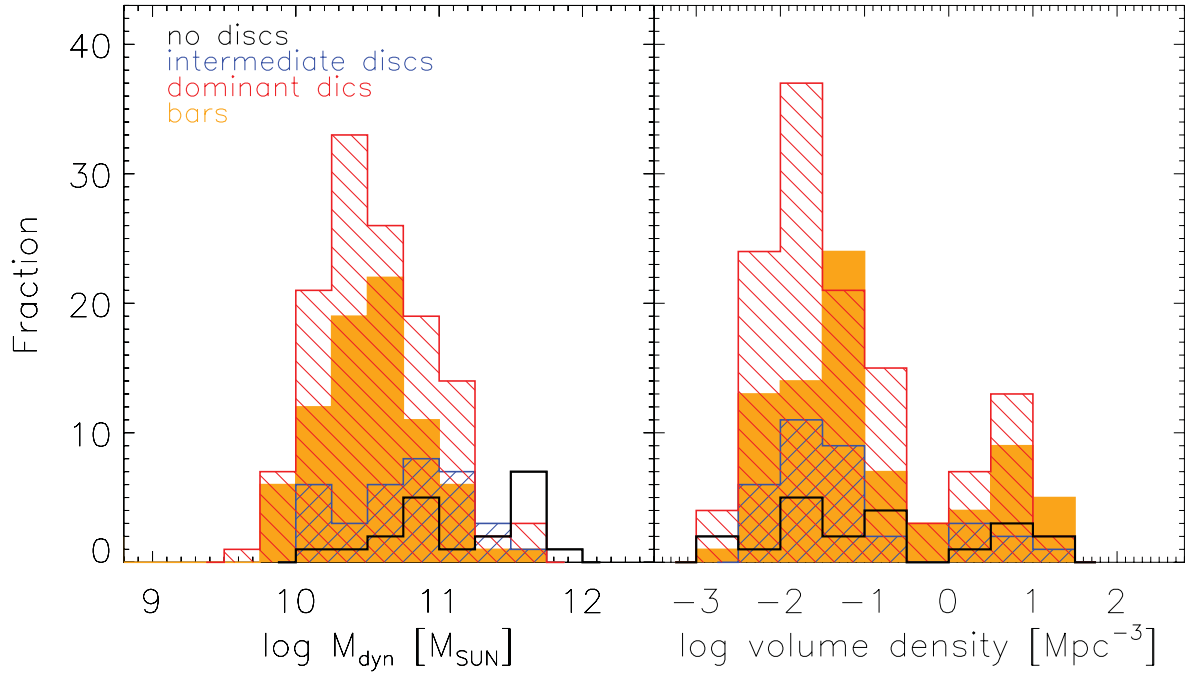

Figure 9. Distribution of ATLAS^{3D} galaxies of different disc content with respect to the total galaxy mass (left) and environment (right). In both panels galaxies are divided into three classes as specified in the legend (left-hand panel) and in text (Section 5.7) and we added all barred galaxies for which we did not attempt a decomposition. Open histogram shows *no discs*, red (left slanted) histogram shows *intermediate discs*, blue (right slanted) histogram shows *dominant discs* distributions and orange filled histogram shows barred galaxies.

Mpc^{-3} of galaxies inside a sphere of a radius which includes 10 nearest neighbours. Here we used the best distance estimates to get the 3D distribution of galaxies (for more details see Paper VII). This density estimator is good to differentiate between cluster and field regions, or Virgo and non-Virgo densities in the ATLAS^{3D} sample.

In both histograms shown in Fig. 9 there is a substantial overlap between the bins, but a clear trend in mass can be seen on the left-hand panel. The *dominant discs* are typically found in lower mass systems (centred around $10^{10.3}$ $M_{\odot}$), the *intermediate discs* in intermediate and more massive systems (centred around $10^{10.9}$ $M_{\odot}$), while the population of *no discs* dominates the most massive end of the distribution of ATLAS^{3D} galaxies (beyond $10^{11.5}$ $M_{\odot}$). Bars are distributed similarly like *dominant discs*, and the KS test gives a probability of 0.98 that these two distributions are drawn from the same parent sample. A contrary result is obtained if one compares the distribution of bars and *intermediate discs* (KS test probability is 0.003). This result is consistent with the observed distribution of galaxy properties on the mass–size diagram and our interpretation of ETG scaling relations (Cappellari et al. 2013a, hereafter Paper XX).

A more complex picture is evident in the right-hand plot of the same figure which considered the environmental dependence. There is no major difference between fractions of different types of galaxies between Virgo [log(volume density) >0] and non-Virgo environments. Outside of Virgo, *dominant discs* and *intermediate discs* have similar distributions, while bars favour a bit more dense environments. Within Virgo, densest regions are favoured by *no disc* populations (as shown already in Paper VII), while *intermediate discs* are found more towards the outskirts. Bars and *dominant discs* are found also in denser environments within the cluster, but bars tend to be more similarly distributed like *no disc* galaxies.

6 CONCLUSIONS

In this work we performed a disc–bulge decomposition of ATLAS^{3D} galaxies with the aim to investigate the photometric evidence for discs in early-type galaxies, and to link them with our kinematic data. For this purpose we selected all (obviously) non-barred galaxies from our sample (180 galaxies out of 260, with 34 slow and 146 fast rotators), and performed a two-component decomposition on to an exponential disc and a bulge described by the Sérsic function of a free index. We did not try to reproduce other components (i.e. bars and rings). The removal of the barred objects is justifiable as these galaxies are known to contain discs and they are found in fast rotators; therefore, the link between photometry and kinematics for these systems is clear, and we cannot fit them accurately with our two-component approach. We also performed a single-component fit with a Sérsic function and several tests with 1D and 2D decompositions methods (presented in Appendix A). The results of the fits are presented in Table C1.

Before listing our main conclusion, we would like to highlight that global Sérsic index is a poor estimate of galaxy morphology. It is widely used to differentiate between early- and late-type galaxies, but even when applied on a sample of only early-type galaxies it does not recover either the traditional Hubble classification based on the apparent shapes or the modern kinematic classification based on the specific angular momentum. Using the decomposition into a bulge and a disc does improve the agreement between morphological and kinematic classifications, but it is still not sufficiently good. While it can be used to highlight those objects which are likely consistent with being fast rotators and disc related (by assuming low Sérsic index for light profiles requiring only a single component and $D/T > 0.05$ for two-component fits), it still fails in recognizing slow rotators (or even galaxies commonly classified as ellipticals). This

Downloaded from http://mnras.oxfordjournals.org/ at European Southern Observatory on August 13, 2014

is of particular importance for higher redshift studies and studies of large samples of galaxies.

Our main conclusions are as follows.

(i) Using the Sérsic index alone (obtained by fitting a single Sérsic function to the light profile) is not sufficient to distinguish between fast and slow rotators. The distribution of Sérsic indices for slow and fast rotators are not drawn from the same sample, and typically fast rotators have low n (<3). There is, however, a significant overlap of slow and fast rotators for $n > 3$. Based on the ATLAS^{3D} sample of nearby early-type galaxies there is a 5 per cent chance that an object with $n < 3$ is a slow rotator. For an object with $n > 3$, there is, however, only a 22 per cent chance that it is a slow rotator.

(ii) Single-component Sérsic fits were adequate for 43 per cent of the analysed early-type galaxies (77 of 180 galaxies). The light profiles of other galaxies were better fitted with two sub-components. The single-component galaxies do not contain a formal exponential component (with $n = 1$), but 46 of 77 (or 59 per cent) of them have a low Sérsic index ($n < 3$), frequently around a value of 1.

(iii) The exponential sub-components, or single components with low Sérsic indices ($n < 3$), are found in the majority of early-type galaxies. We show that these components are present in galaxies with regular rotation, intermediate to high angular momentum and objects with h_3–V/σ anticorrelation typical for discs. Therefore, we associate exponential sub-components with discs. Similarly, single components of low Sérsic indices can be associated with discs (if $n \sim 1$) and disc-like structures (for other n that are <3).

(iv) About 17 per cent of ATLAS^{3D} (early-type) galaxies (31 of 180 galaxies, or 12 per cent of 258 ATLAS^{3D} galaxies with good imaging, assuming here that not analysed bars are disc-related structures) do not have any evidence for discs or disc-like structures.

(v) About 41 per cent of the stellar mass of early-type galaxies is in discs or disc-like components.

(vi) Disc or disc-like components are typically found in fast rotators, while in some slow rotators the presence of exponential sub-components or single components with low Sérsic indices ($n < 3$) could be related to structures made of more complex orbital families (with high angular momentum) allowed in non-axisymmetric potentials. These components are often related to KDCs.

(vii) 24 of 34 (70 per cent) slow rotators are best fitted with single components. Of these four have a low Sérsic index (<3). Other slow rotators (10) have a substantial fraction of light in the exponential components.

(viii) 93 of analysed 146 fast rotators (64 per cent) have exponential sub-components (discs). 42 of the remaining 53 fast rotators have single components of low Sérsic index (<3). There are only 11 fast rotators that do not show clear evidence for discs or disc-like structures in their photometry. For some of these galaxies inclination effects could be the reason for not detecting the disc-like structures in photometry, some are recent merger remnants while rest are complex systems.

(ix) Sérsic index of the bulge sub-component is smaller than 3 for 73 of 103 early-type galaxies, for which a two-component fit was deemed necessary. The same is true for 70 objects if $n = 2.5$ is used. It is not obvious that only secular evolution is responsible for build-up of these sub-components.

(x) There are trends between D/T and n_b with λ_R, such that for high λ_R, D/T is high and n_b is low, but there is no clear correlation. The Sérsic index n_{tot} from a single fit to galaxies does not correlate strongly with D/T ratio, as shown by other studies, or with λ_R.

(xi) Decomposing those galaxies that require two components into discs and bulges improves the differentiation between fast and slow rotators compared to using a single-component Sérsic index. To a first approximation, it is possible to describe fast rotators as early-type galaxies with exponential discs ($D/T > 0.05$) or, for single-component Sérsic fits, low n ($n < 3$). Similarly, slow rotators can be described as galaxies without exponential components and high n. We recommend this criterion when stellar kinematics is not available, but the correspondence is not 1:1, with a 7 per cent probability (11 of 146 analysed fast rotators) to miss a fast rotator and a 59 per cent probability (20 of 34 analysed slow rotators do not have disc-like components) to correctly recognize a slow rotator, implying that the decomposition can be used only as a guidance for classification. In general, kinematic analysis and classification based on the angular momentum content remains the best attempt to mitigate the influence of inclination effects.

(xii) As noted previously by other authors, there is a significant dependance of photometric parameters on the inclination effects. Strong (exponential) disc signatures, however, can be seen in the light profiles even at low inclinations, while weak discs disappear sooner and are hard to detect below an inclination of $\sim 50^\circ$.

(xiii) Disc-dominated galaxies are typically the least massive, while galaxies with no tracers of discs are the most massive systems in the nearby Universe. Barred galaxies have a consistent distribution of mass as systems dominated by discs.

(xiv) There is no strong relation between the environment and the amount of disc light and discs are found in all environments. At high densities there is a weak evidence that disc-dominated systems are found in more denser regions than galaxies with smaller disc contributions. Barred galaxies are found at all densities, but typically in denser regions than dominant discs, and have a similar distribution like galaxies with no discs.

ACKNOWLEDGEMENTS

MC acknowledges support from a Royal Society University Research Fellowship. MS acknowledges support from an STFC Advanced Fellowship ST/F009186/1. RMMcD is supported by the Gemini Observatory, which is operated by the Association of Universities for Research in Astronomy, Inc., on behalf of the international Gemini partnership of Argentina, Australia, Brazil, Canada, Chile, the UK and the USA. SK acknowledges support from the Royal Society Joint Projects Grant JP0869822. TN and MBois acknowledge support from the DFG Cluster of Excellence 'Origin and Structure of the Universe'. PS is an NWO/Veni Fellow. The research leading to these results has received funding from the European Community's Seventh Framework Programme (/FP7/2007-2013/) under grant agreement No. 229517. This work was supported by the rolling grants 'Astrophysics at Oxford' PP/E001114/1 and ST/H002456/1 and visitors grants PPA/V/S/2002/00553, PP/E001564/1 and ST/H504862/1 from the UK Research Councils. RLD acknowledges travel and computer grants from Christ Church, Oxford, and support from the Royal Society in the form of a Wolfson Merit Award 502011.K502/jd. We acknowledge the usage of the HyperLeda data base (http://leda.univ-lyon1.fr).This paper is based on observations obtained at the WHT, operated by the Isaac Newton Group in the Spanish Observatorio del Roque de los Muchachos of the Instituto de Astrofísica de Canarias. Funding for the SDSS and SDSS-II was provided by the Alfred P. Sloan Foundation, the Participating Institutions, the National Science Foundation, the US Department of Energy, the National Aeronautics and Space Administration, the Japanese

Downloaded from http://mnras.oxfordjournals.org/ at European Southern Observatory on August 13, 2014

Monbukagakusho, the Max Planck Society and the Higher Education Funding Council for England. The SDSS was managed by the Astrophysical Research Consortium for the Participating Institutions.

REFERENCES

Abazajian K. N. et al., 2009, ApJS, 182, 543
Aguerri J. A. L., Trujillo I., 2002, MNRAS, 333, 633
Allen P. D., Driver S. P., Graham A. W., Cameron E., Liske J., de Propris R., 2006, MNRAS, 371, 2
Andredakis Y. C., Peletier R. F., Balcells M., 1995, MNRAS, 275, 874
Arnold R., de Zeeuw P. T., Hunter C., 1994, MNRAS, 271, 924
Athanassoula E., 2005, MNRAS, 358, 1477
Bacon R. et al., 2001, MNRAS, 326, 23
Balcells M., Graham A. W., Domínguez-Palmero L., Peletier R. F., 2003, ApJ, 582, L79
Barden M. et al., 2005, ApJ, 635, 959
Bell E. F., McIntosh D. H., Katz N., Weinberg M. D., 2003, ApJS, 149, 289
Bender R., Surma P., Doebereiner S., Moellenhoff C., Madejsky R., 1989, A&A, 217, 35
Bender R., Saglia R. P., Gerhard O. E., 1994, MNRAS, 269, 785
Benson A. J., Džanović D., Frenk C. S., Sharples R., 2007, MNRAS, 379, 841
Binney J., Merrifield M., 1998, Galactic Astronomy. Princeton Univ. Press, Princeton, NJ
Blanton M. R. et al., 2003, ApJ, 594, 186
Bois M. et al., 2011, MNRAS, 416, 1654 (Paper VI)
Boroson T., 1981, ApJS, 46, 177
Burstein D., 1979, ApJ, 234, 435
Byun Y. I., Freeman K. C., 1995, ApJ, 448, 563
Caon N., Capaccioli M., D'Onofrio M., 1993, MNRAS, 265, 1013
Cappellari M., 2002, MNRAS, 333, 400
Cappellari M., 2008, MNRAS, 390, 71
Cappellari M. et al., 2007, MNRAS, 379, 418
Cappellari M. et al., 2011a, MNRAS, 413, 813 (Paper I)
Cappellari M. et al., 2011b, MNRAS, 416, 1680 (Paper VII)
Cappellari M. et al., 2013a, MNRAS, 432, 1862 (Paper XX)
Cappellari M. et al., 2013b, MNRAS, 432, 1709 (Paper XV)
Chen C.-W., Côté P., West A. A., Peng E. W., Ferrarese L., 2010, ApJS, 191, 1
Ciotti L., 1991, A&A, 249, 99
Ciotti L., Bertin G., 1999, A&A, 352, 447
Coccato L., Morelli L., Corsini E. M., Buson L., Pizzella A., Vergani D., Bertola F., 2011, MNRAS, 412, L113
Côté P. et al., 2004, ApJS, 153, 223
Courteau S., de Jong R. S., Broeils A. H., 1996, ApJ, 457, L73
D'Onofrio M., 2001, MNRAS, 326, 1517
Davies R. L., Efstathiou G., Fall S. M., Illingworth G., Schechter P. L., 1983, ApJ, 266, 41
de Jong R. S., 1996, A&AS, 118, 557
de Jong R. S., Simard L., Davies R. L., Saglia R. P., Burstein D., Colless M., McMahan R., Wegner G., 2004, MNRAS, 355, 1155
de Souza R. E., Gadotti D. A., dos Anjos S., 2004, ApJS, 153, 411
de Vaucouleurs G., 1959, Handbuch der Physik, 53, 311
de Zeeuw P. T. et al., 2002, MNRAS, 329, 513
Duc P.-A. et al., 2011, MNRAS, 417, 863 (Paper IX)
Emsellem E., Monnet G., Bacon R., 1994, A&A, 285, 723
Emsellem E. et al., 2004, MNRAS, 352, 721
Emsellem E. et al., 2007, MNRAS, 379, 401
Emsellem E. et al., 2011, MNRAS, 414, 888 (Paper III)
Erwin P., Pohlen M., Beckman J. E., 2008, AJ, 135, 20
Faber S. M. et al., 1997, AJ, 114, 1771
Fabricius M. H., Saglia R. P., Fisher D. B., Drory N., Bender R., Hopp U., 2012, ApJ, 754, 67
Ferrarese L., van den Bosch F. C., Ford H. C., Jaffe W., O'Connell R. W., 1994, AJ, 108, 1598
Ferrarese L. et al., 2006, ApJS, 164, 334
Fisher D. B., Drory N., 2008, AJ, 136, 773
Freeman K. C., 1970, ApJ, 160, 811
Gadotti D. A., 2008, MNRAS, 384, 420
Gadotti D. A., 2009, MNRAS, 393, 1531
Gadotti D. A., Sánchez-Janssen R., 2012, MNRAS, 423, 877
Gerhard O. E., 1993, MNRAS, 265, 213
Gerhard O. E., Binney J. J., 1996, MNRAS, 279, 993
Gradshteyn I. S., Ryzhik I. M., Jeffrey A., Zwillinger D., 2000, Table of Integrals, Series, and Products. Academic Press, New York
Graham A. W., 2001, AJ, 121, 820
Graham A. W., Driver S. P., 2005, Publ. Astron. Soc. Aust., 22, 118
Graham A., Lauer T. R., Colless M., Postman M., 1996, ApJ, 465, 534
Graham A. W., Erwin P., Trujillo I., Asensio Ramos A., 2003, AJ, 125, 2951
Hoyos C. et al., 2011, MNRAS, 411, 2439
Hubble E. P., 1922, ApJ, 56, 162
Hubble E. P., 1926, ApJ, 64, 321
Hubble E. P., 1936, Realm of the Nebulae. Yale Univ. Press, New Haven
Jeans J. H., 1929, Astronomy and Cosmology. Cambridge Univ. Press, Cambridge
Jedrzejewski R. I., 1987, MNRAS, 226, 747
Johnston E. J., Aragón-Salamanca A., Merrifield M. R., Bedregal A. G., 2012, MNRAS, 422, 2590
Jorgensen I., Franx M., 1994, ApJ, 433, 553
Kent S. M., 1985, ApJS, 59, 115
Khochfar S. et al., 2011, MNRAS, 417, 845 (Paper VIII)
Kormendy J., 1977, ApJ, 217, 406
Kormendy J., 1993, in Dejonghe H., Habing H. J., eds, IAU Symp. 153, Galactic Bulges. Kluwer Academic Publishers, Dordrecht, p. 209
Kormendy J., Bender R., 2012, ApJS, 198, 2
Kormendy J., Kennicutt R. C., Jr, 2004, ARA&A, 42, 603
Kormendy J., Fisher D. B., Cornell M. E., Bender R., 2009, ApJS, 182, 216
Krajnović D., Cappellari M., de Zeeuw P. T., Copin Y., 2006, MNRAS, 366, 787
Krajnović D. et al., 2008, MNRAS, 390, 93
Krajnović D. et al., 2011, MNRAS, 414, 2923 (Paper II)
Lackner C. N., Gunn J. E., 2012, MNRAS, 421, 2277
Landsman W. B., 1993, in ASP Conf. Ser. Vol. 52, Astronomical Data Analysis Software and Systems II. Astron. Soc. Pac., San Francisco, p. 246
Laurikainen E., Salo H., Buta R., Knapen J. H., 2007, MNRAS, 381, 401
Laurikainen E., Salo H., Buta R., Knapen J. H., 2009, ApJ, 692, L34
Laurikainen E., Salo H., Buta R., Knapen J. H., Comerón S., 2010, MNRAS, 405, 1089
Laurikainen E., Salo H., Buta R., Knapen J. H., 2011, Adv. Astron., 2011, 18
MacArthur L. A., Courteau S., Holtzman J. A., 2003, ApJ, 582, 689
Markwardt C. B., 2009, in Bohlender D. A., Durand D., Dowler P., eds, ASP Conf. Ser. Vol. 411, Astronomical Data Analysis Software and Systems XVIII. Astron. Soc. Pac., San Francisco, p. 251
McIntosh D. H. et al., 2005, ApJ, 632, 191
Méndez-Abreu J., Aguerri J. A. L., Corsini E. M., Simonneau E., 2008, A&A, 478, 353
Monnet G., Bacon R., Emsellem E., 1992, A&A, 253, 366
Moré J. J., Garbow B. S., Hillstrom K. E., 1980, User Guide for MINPACK-1, Argonne National Laboratory Report ANL-80-74, 74
Naab T., Trujillo I., 2006, MNRAS, 369, 625
Paturel G., Petit C., Prugniel P., Theureau G., Rousseau J., Brouty M., Dubois P., Cambrésy L., 2003, A&A, 412, 45
Peng C. Y., Ho L. C., Impey C. D., Rix H.-W., 2002, AJ, 124, 266
Pignatelli E., Fasano G., Cassata P., 2006, A&A, 446, 373
Reynolds J. H., 1920, MNRAS, 80, 746
Rix H., White S. D. M., 1990, ApJ, 362, 52
Rix H.-W., Franx M., Fisher D., Illingworth G., 1992, ApJ, 400, L5
Rubin V. C., Graham J. A., Kenney J. D. P., 1992, ApJ, 394, L9
Saglia R. P., Bertschinger E., Baggley G., Burstein D., Colless M., Davies R. L., McMahan R. K., Jr, Wegner G., 1997, ApJS, 109, 79
Sandage A., 2005, ARA&A, 43, 581

Downloaded from http://mnras.oxfordjournals.org/ at European Southern Observatory on August 13, 2014

Sandage A., Freeman K. C., Stokes N. R., 1970, ApJ, 160, 831
Scarlata C. et al., 2007, ApJS, 172, 406
Schombert J. M., Bothun G. D., 1987, AJ, 93, 60
Scorza C., Bender R., Winkelmann C., Capaccioli M., Macchetto D. F., 1998, A&AS, 131, 265
Scot et al., 2013, MNRAS, 432, 1894 (Paper XXI)
Serra P. et al., 2012, MNRAS, 422, 1835 (Paper XIII)
Sérsic J. L., 1968, Atlas de galaxias australes. Observatorio Astronomico, Cordoba, Argentina
Shen S., Mo H. J., White S. D. M., Blanton M. R., Kauffmann G., Voges W., Brinkmann J., Csabai I., 2003, MNRAS, 343, 978
Simard L. et al., 2002, ApJS, 142, 1
Simard L. et al., 2009, A&A, 508, 1141
Simard L., Mendel J. T., Patton D. R., Ellison S. L., McConnachie A. W., 2011, ApJS, 196, 11
Spitzer L., Jr, Baade W., 1951, ApJ, 113, 413
Statler T. S., 1991, AJ, 102, 882
Trujillo I., Erwin P., Asensio Ramos A., Graham A. W., 2004, AJ, 127, 1917
van den Bergh S., 1976, ApJ, 206, 883
van der Marel R. P., Franx M., 1993, ApJ, 407, 525
Weinzirl T., Jogee S., Khochfar S., Burkert A., Kormendy J., 2009, ApJ, 696, 411
Yoon I., Weinberg M. D., Katz N., 2011, MNRAS, 414, 1625

APPENDIX A: CHOOSING THE FITTING METHOD

As mentioned in Section 3.1, there are various methods which can be used to parametrically describe a light distribution of a galaxy. The availability of computing power made techniques working in two dimensions widely used in the recent years, which are especially better suited for working with spatially poorly resolved galaxies at higher redshifts. Our method of choice, however, was to fit 1D light profiles obtained by azimuthally averaging along ellipses, because this approach allowed for a uniform and a systematic treatment of early-type galaxies with and without discs. In particular, in the case of one-component fits we used profiles azimuthally averaged along ellipses with fixed position angle and flattening, while in the case of two-component decomposition we used profiles azimuthally averaged along best-fitting ellipses, where the ellipse fitting program was allowed to vary the position angle and flattening of the ellipses.

There are, however, different approaches with regard to the best suited 1D light profile for the decomposition. For example, one could take major axis cuts (e.g Kormendy 1977; Burstein 1979; Fisher & Drory 2008; Kormendy & Bender 2012), major and minor axis cuts (e.g Kent 1985; de Jong 1996) or azimuthally averaged light profiles (e.g Boroson 1981; Saglia et al. 1997; Aguerri & Trujillo 2002; Blanton et al. 2003; MacArthur et al. 2003; Naab & Trujillo 2006). While azimuthally averaging increases the signal-to-noise ratio and removes local irregularities, the argument against this procedure is that, unless the galaxy is seen directly face-on, the mixing of the disc and bulge components is such that the radial light profile becomes ambiguous, i.e. azimuthally averaging mixes the contributions of the disc and the bulge. Gadotti & Sánchez-Janssen (2012) point out this problem of averaging along isophotes in an edge-on galaxy, but remark also that it is less an issue for other inclinations. As our galaxies are seen at (random) range of inclinations, and we desired a uniform approach to all galaxies, we did not change the extraction of 1D profiles. We, however, made a test by extracting light profiles along the major axes and while we found some differences, they do not change our results and conclusions.

In this appendix we want to understand the origin of differences between our 1D and 2D approaches. Our wish is not to weigh relative merits of these two approaches, but to quantify the differences one can expect between them. As our choice of 2D decomposition algorithm we use GALFIT (Peng et al. 2002).

A1 One-component fits

We first run GALFIT to fit a single Sérsic function to our images. As a preparation of the images before running GALFIT, we estimated the sky levels and determined the centre for each galaxy. Furthermore, we created error images based on Poisson noise and seeing images using the same average seeing as given in Section 3.2. As initial values for position angle and flattening of the galaxies we used values from Paper II, which are the same as used for 1D single-component fits. The final values for the ellipse parameters returned by GALFIT are very similar to the Paper II values. The rms for ellipticities is 0.063 and for position angles 3.°67, which are both consistent with errors estimated in Paper II. The comparison with the single-component 1D fits described in Section 4 is shown on the left-hand panel of Fig. A1, which shows the distribution of the Sérsic indices. For completeness we also show results of the 1D fits to light profiles obtained by azimuthally averaging along free ellipses on the right-hand panel of Fig. A1. Note that these latter results come from the fits which were used to judge whether a decomposition is necessary or a single component is sufficient to describe the light profile (see Section 3.2).

There is a general similarity between the 1D and 2D results when 1D light profiles are obtained by azimuthally averaging along fixed ellipses. The rms of the difference of these two estimates is $\sim$0.8, and there is a trend for some galaxies to have larger $n_{\rm tot}$ values using our method, but the difference of the medians of the two distributions is 0.08. The non-symmetric shape of the distributions is clearly seen on the bottom panels with histograms.

Comparison of the 2D results with those in one dimension using the free ellipses is shown on the right-hand panels. There are two notable properties: the spread around the one-to-one line is larger (rms of $\sim$1.1) than in the case using fixed ellipses and there is a trend such that 1D $n_{\rm tot}$ are smaller than 2D values (median difference of -0.35) when 2D $n_{\rm tot} < 4$.

The cause for the better agreement of 2D results and fits to 1D profiles obtained by azimuthally averaging along fixed ellipses can be understood if galaxies are divided into fast and slow rotators. When free ellipses are used, distributions of Sérsic indices for fast rotators in 1D and 2D cases are different (lower-right panel of Fig. A1). Distributions for slow rotators are, however, quite similar. In this work we show that fast rotators, unlike slow rotators, can be decomposed into two components (Sections 5.2 and 5.4) of typically different ellipticities. Fitting a single component to light profiles extracted along fixed or free ellipses will give different results as the light profiles themselves differ. As we are fitting one component, it is reasonable to ignore the changes in ellipticities and extract light profiles along the fixed ellipses. For galaxies that may show strong variations in ellipticity (or position angle) due to their triaxial structure (and not existence of multiple components), this approach might not be the most optimal. These objects are typically slow rotators and do not require a decomposition in two components. We compared the results of the fits from free and fixed ellipse models and found only three galaxies that have $n_{\rm tot}$ different for 1 or more between these two cases (NGC 4486 – it does not show any signature of rotation; NGC 5576 and NGC 7454 – both galaxies have peculiar and non-regular velocity maps). Hence, as there is only a handful of such objects in our sample and for the sake of uniformity we fit them as all other objects. This closely resembles

Downloaded from http://mnras.oxfordjournals.org/ at European Southern Observatory on August 13, 2014

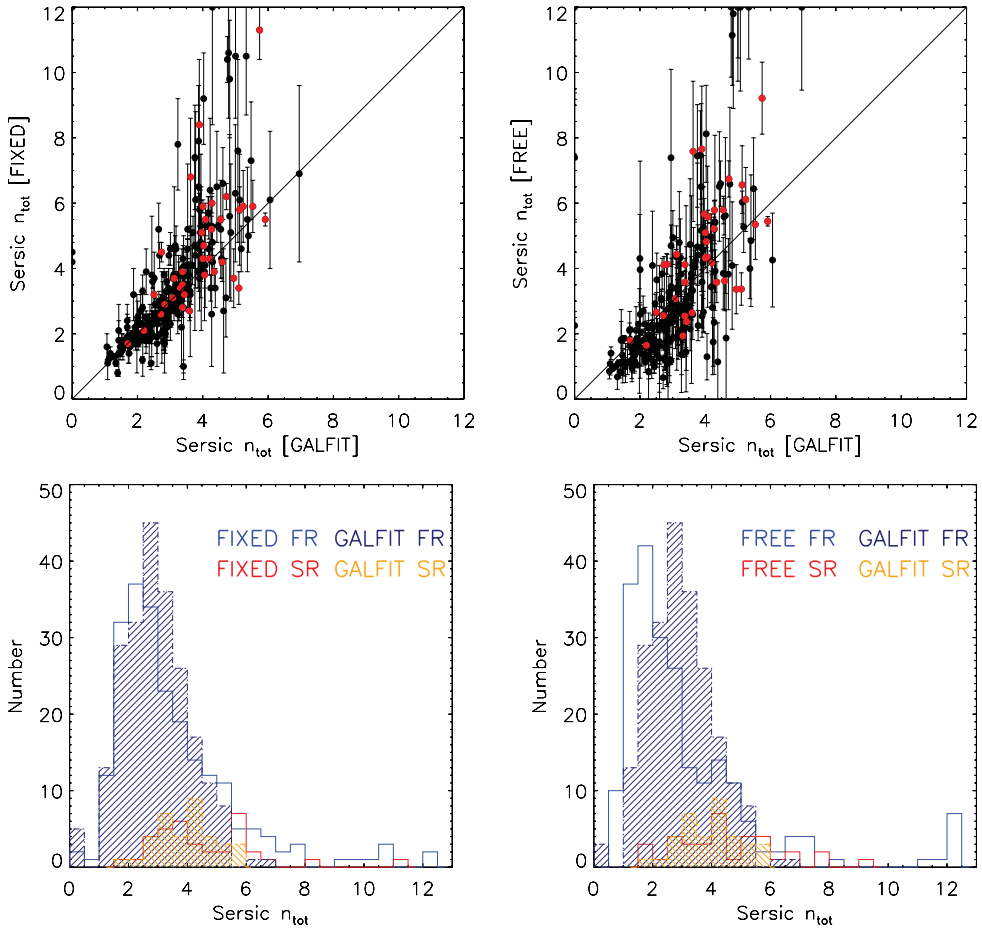

Figure A1. Comparison of Sérsic indices using our method (in one dimension) and GALFIT (in two dimensions) on ATLAS^{3D} galaxies. Left: comparison of GALFIT results and single Sérsic component fits to light profiles obtained by azimuthally averaging along fixed ellipses (described as FIXED in the legend). Right: comparison of GALFIT results and single Sérsic component fits to light profiles obtained by azimuthally averaging along free ellipses (described as FREE in the legend). Top row panels show a direct comparison for objects, while bottom row panels show histograms of respective distributions. On top panels, slow rotators are shown with red symbols. On bottom panels, GALFIT results are shown with hatched histograms, while 1D results with open histograms, and colours relate to the separation into fast and slow rotators, as shown in the legend.

what is done in 2D (galaxy is assumed to have fixed position angle and ellipticity) and explains the similarity of the results with these two methods.

A2 Two-component fits

We also run GALFIT to decompose the images in free Sérsic and exponential components, and we decompose 1D profiles obtained by azimuthally averaging along fixed ellipses using the same 1D algorithm as in the main text (see Section 3.2). The results of this exercise are shown in Fig. A2, where we compare Sérsic indices of the disc and bulge components for these three methods (2D GALFIT, 1D along free and fixed ellipses). Before running GALFIT, images were prepared as in the case of single-component fitting, but this time we fix in GALFIT the position angle and flattening of the exponential components, while these parameters were left free for the bulge components. The parameters were fixed to the values in Paper II (these are the same values used to fix the parameters of the ellipses when extracting 1D light profiles). In Fig. A2 we include only those objects which required two components in 1D (free or fixed, respectively) fits.

Again, there are differences between 1D and 2D approaches and between light profiles extracted from free and fixed ellipses. The differences are more pronounced between 1D free and 2D methods. The trend is the same as seen in the case of fitting only one component to the light profile: the 1D free n_b are smaller than the 2D n_b for about 1–2 units, and the 1D distribution of n_b is asymmetric, while the 2D distribution is more symmetric. Bulge Sérsic indices of 1D fixed ellipse fits are more similar to 2D results, although they span a larger range of values. Note that we run fits on the 1D fixed profiles within the same fitting range as for 1D free profiles, which sometimes might not be optimal.

The difference between results obtained by GALFIT and 1D light profiles extracted along free ellipses warrants a further test of the 1D fitting method; specifically, can 1D methods recover parameters of model galaxies? For this purpose we use our GALFIT two-component models to extract light profiles along azimuthally averaged ellipses of free parameters. The extraction was done in the same way as for galaxy images using kinemetry. These profiles were then fitted with

Downloaded from http://mnras.oxfordjournals.org/ at European Southern Observatory on August 13, 2014

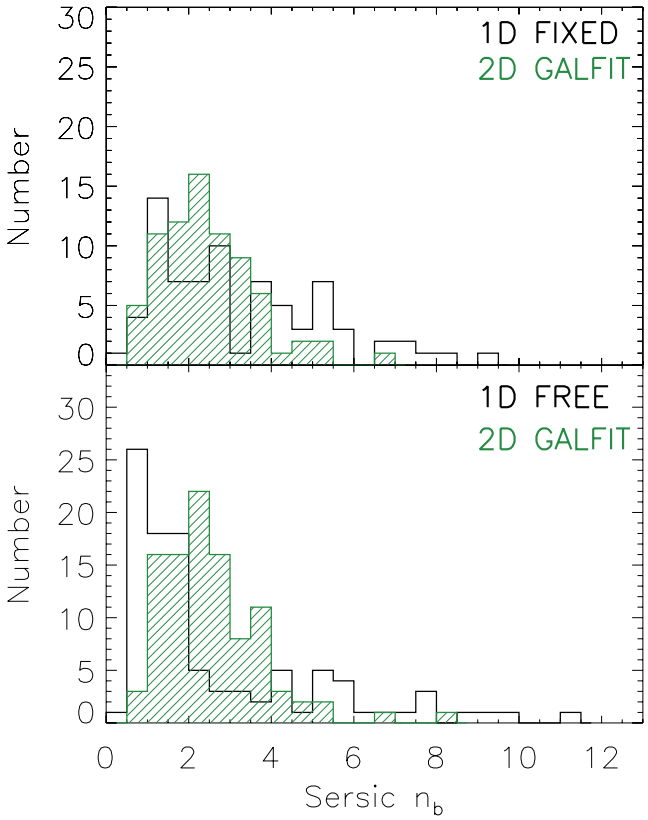

Figure A2. Comparison of bulge Sérsic indices obtained by decomposing ATLAS^{3D} galaxies into a bulge and a disc component, using GALFIT (hatched histograms on all panels) and fitting 1D light profiles (black histograms on all panels) extracted by azimuthally averaging along fixed ellipses (top; described as 1D FIXED in the legend) and free (bottom panel; described as 1D FREE in the legend). Only galaxies that required two components in 1D fits are shown, which explains the difference between the bottom panel and histograms in Fig. 3.

our 1D algorithm. The only significant difference with the fits to the real galaxies was that we used a fixed range for all galaxies, between 2.5 arcsec and the radius at which the intensity of the models was equal to 1 (i.e. no special fitting ranges for individual galaxies). This was possible as GALFIT models are made of only two components (e.g. no nuclear or halo components, only bulge and a disc). We also excluded all models for which GALFIT predicted bulge or disc sizes of less than 2.5 arcsec and n_b smaller than 0.3, as these are 1D fit boundary conditions.

The comparison is shown in Fig. A3. The top panel shows the two distributions of the Sérsic index n_b, while the bottom panel shows a more direct comparison between individual values for each galaxy. The two distributions are not identical, but are generally similar. On the bottom panel, we highlight with open circles those models for which our 1D algorithm returned the best fit with only one (free Sérsic) component (i.e. for the fitting range and the starting parameters the algorithm found the best-fitting solution with a single-component model). These cases are typically the largest outliers and give an estimate of the systematic errors involved related to the choice of initial conditions and the fitting range used. If they are excluded from the comparison, the rms of the difference in n_b is 0.18 and the KS test gives the probability of ∼80 per cent that the data are drawn from the same distribution.

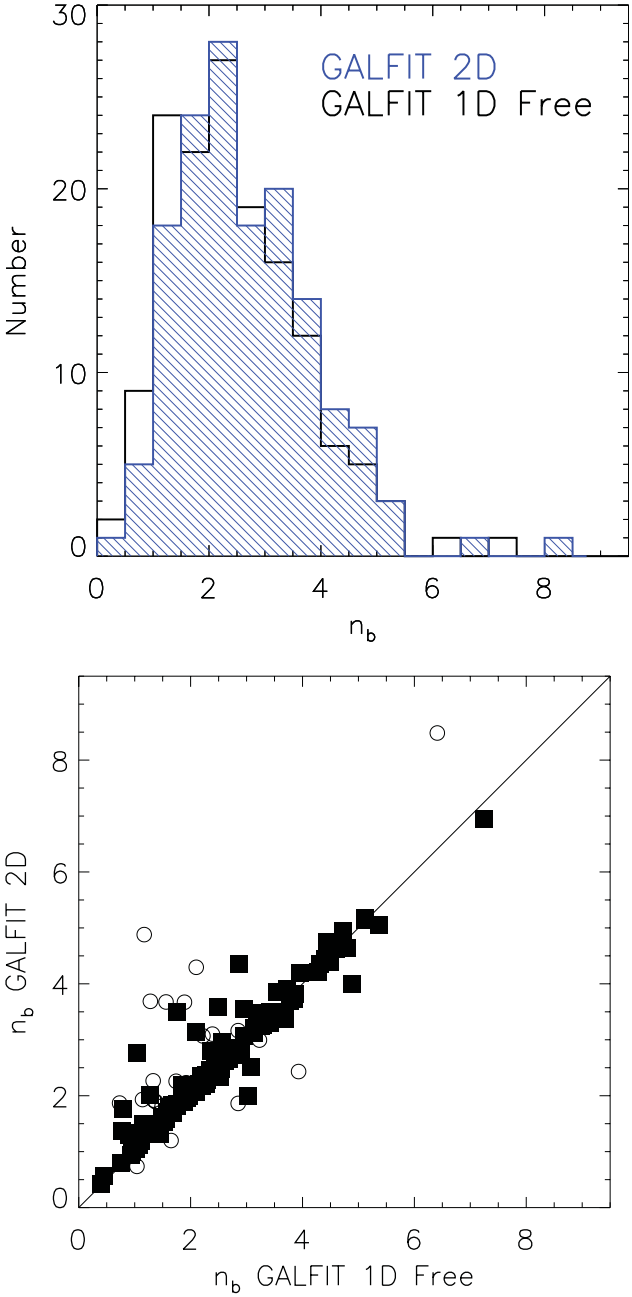

Figure A3. Top: distribution of Sérsic indices obtained by using GALFIT to fit the same sample of ATLAS^{3D} galaxies as in the main text (hatched blue histogram) and fitting 1D light profiles extracted by azimuthally averaging along free ellipses of the same GALFIT models. Bottom: comparison of individual values of Sérsic indices. Open circles are models for which our 1D algorithm automatically returned the best fit with only one (free Sérsic) component, while solid squares are galaxies decomposed into a disc and a bulge.

The results of this test suggest that the 1D fitting method used in the main text can recover the structural parameters of the models, fully justifying our approach. The differences between the methods presented in this appendix point out large systematic uncertainties associated with the photometric decomposition, which are much larger than any statistical errors due to noise in the data. In the case of the 1D fits, the most dominant contributors are the methods used to extract the profiles (e.g. along fixed or free ellipses) and the

Downloaded from http://mnras.oxfordjournals.org/ at European Southern Observatory on August 13, 2014

fitting range. This should be kept in mind when comparing Sérsic parameters obtained with different methods and approaches.

APPENDIX B: COMPARISON WITH LITERATURE DATA

A comparison of the results of this work with published data faces two problems: there are not many studies that fit in a comparable way (i.e. decomposition into a free Sérsic and an exponential functions), and the number of galaxies in common is typically small. Studies which consider a similar set of nearby galaxies often use a parametrization into a de Vaucouleurs profile and an exponential profile (e.g. Kent 1985) or decompose galaxies into more than just two components (e.g. Kormendy & Bender 2012).

We have selected two studies with which we have a relatively large overlap of objects. For the comparison of the single Sérsic fits we use the results of the ACSVCS (Côté et al. 2004) survey of Virgo galaxies presented in Chen et al. (2010). A number of these galaxies are also present in Kormendy et al. (2009) and the authors show a general agreement between these two studies, hence we use only the larger ACSVCS sample. The comparison is shown in the left-hand panel of Fig. B1. There are 44 galaxies in common and there is a generally good agreement between the values of the Sérsic indices with an rms of 0.7. The two strongest outliers are NGC 4267 and NCG4377 (above and below the one-to-one relation, respectively), for which the fits are poor, possibly due to bar/ring structures. Generally, at larger values of $n_{\rm tot}$ the deviations increase in the sense that Chen et al. (2010) values are systematically larger. This can partially be explained by the fact that they use the *HST* imaging and exclude only the region within the break radius, which is for galaxies in common typically smaller than our 2.5 arcsec inner limit.

For the comparison of our decomposition results we used the comprehensive study of S0 and spiral galaxies by Laurikainen et al. (2010). There are 23 galaxies in common (S0s), but in the right-hand panel of Fig. B1 we compare only 16. Of the seven discarded galaxies two were decomposed in more than two components, while other two objects were not decomposed by Laurikainen et al. (2010). Also, three objects did not warrant the decomposition by our approach. There is a considerably larger spread between these two data sets (rms $\sim$1.2) than for the single Sérsic fits comparison, but excluding two largest outliers on each side of the one-to-one relation, the remaining points are in a general agreement within uncertainties.

A similar conclusion is achieved by looking at the comparison of D/T ratios. We converted Laurikainen et al. (2010) B/T ratios to $D/T = 1 - B/T$, in order to compare with our D/T values. We stress, however, that a 'bulge' may not necessarily be the same in these two studies, as Laurikainen et al. (2010) decompose some galaxies in more than two components. Still, within our nominal (median) error of 0.08 in D/T, our results agree. The two largest outliers (NGC 4694 and NGC 5493, above and below the one-to-one relation, respectively) illustrate the difference in achieved results when using different methods. Laurikainen et al. (2010) decomposed both galaxies with more than two components, also using Ferrers functions for the possible bar component in NGC 5493. We find large variations in possible B/T (or D/T) for both galaxies (one of the biggest in the sample) which indicate the complex nature of these systems.

The comparisons of Fig. B1 are encouraging, given that the fits are done with different methods and on different data. The role of systematic errors is hard to estimate in these studies, but should not be removed from consideration. As an example of possible systematic effects arising from the different methods applied on different samples, we compare our results with the results of two studies which analysed statistically large samples. The first one is a comparison with Gadotti (2009). That work analyses about 1000 galaxies in the range $0.02 < z < 0.07$, selected in a similar mass range ($M_\star > 10^{10}$ M$_\odot$, but typically $M_\star < 5 \times 10^{11}$ M$_\odot$), but with $q > 0.9$. As the author notes, the latter selection likely introduces a bias, as it selects galaxies that are more round, brighter and more concentrated.

On top panels of Fig. B2, we plot only the sub-sample of unbarred galaxies from Gadotti (2009), as well as our results. Most striking is the disparity of the $n_{\rm b}$ distributions, ours being smaller for about a value of 2, which is somewhat larger (but not inconsistent) than what we found in Section A2. In our sample, mostly slow rotators have larger indices, and it is possible that the mentioned bias introduced some excess of $n \sim 4$ galaxies in the Gadotti (2009) sample. The distribution of D/T ratios, however, is rather similar. Both studies find a large number of galaxies with no exponential components (they are classified as ellipticals in Gadotti 2009, while in our case

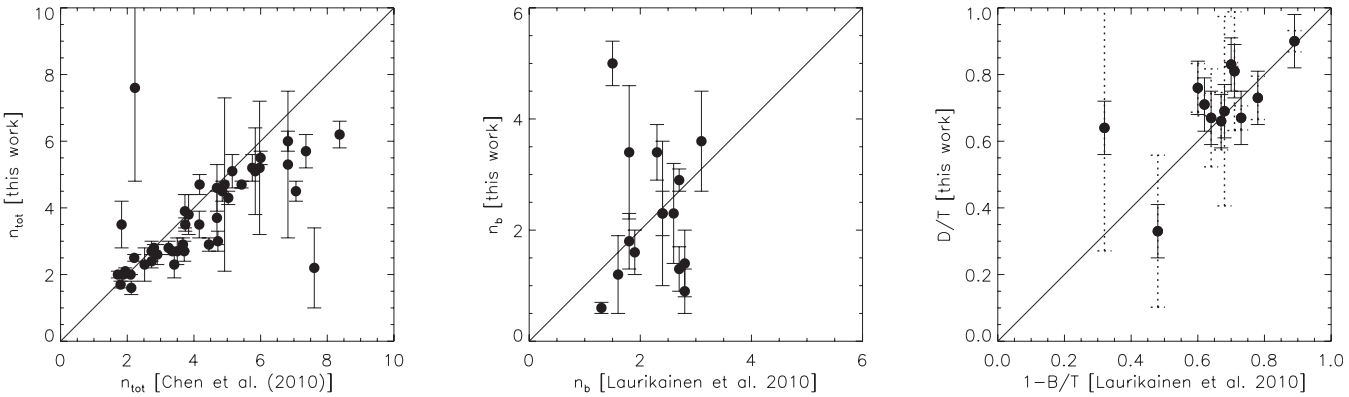

Figure B1. Comparison of obtained Sérsic indices and D/T ratios with the literature data for selected galaxies. Left: comparison of single-component Sérsic indices for galaxies in common with the ACSVCS Chen et al. (2010). Middle: comparison of the bulge Sérsic indices for galaxies in common with Laurikainen et al. (2010). Right: comparison of our D/T ratios with those of Laurikainen et al. (2010). Dashed error bars are individual Monte Carlo uncertainties, while thick error bars correspond to the median error (of 0.08) for all objects with $D/T > 0$. In all panels the straight line is one-to-one relation.

Downloaded from http://mnras.oxfordjournals.org/ at European Southern Observatory on August 13, 2014

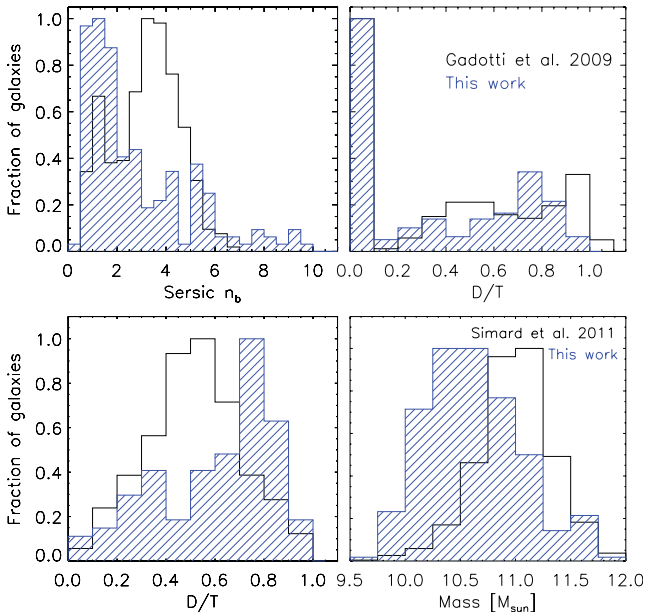

Figure B2. Top: comparison with Gadotti (2009) focusing on the bulge Sérsic indices (left) and D/T (right). Bottom: comparison off D/T ratios (left) and stellar mass distribution (right) of a subsample of galaxies selected from Simard et al. (2011). In all panels our data are shown with hatched (blue) histograms, but note that in the comparison with Simard et al. (2011) we used only objects with $D/T > 0$. All histograms are normalized to peak values.

these are mostly slow rotators, but also fast rotators with small n), and a large spread of D/T values.

We also compared our results with a recent study of Simard et al. (2011) who analyse more than a million of SDSS galaxies. From their catalogue we selected a set of objects trying to match the general properties of our sample (i.e. local early-types of a similar mass) and we looked for galaxies that can be decomposed into bulge and disc systems. Specifically, this meant we looked for objects with redshift below 0.1, ellipticity below 0.85, stellar mass in the range $9.7 < \log(M_\star) < 12\,\mathrm{M}_\odot$ (calculated from colours using Bell et al. 2003), image smoothness parameter S2 ≤ 0.075 (Simard et al. 2009) and equivalent width of [O II] < 5 Å. From these galaxies we further selected those that had $P_{\mathrm{pS}} < 0.32$. P_{pS} is the F-statistics probability that the decomposition into a bulge and a disc is not preferred to a single Sérsic fit (low values mean that objects could be considered genuine two-component systems).

As Simard et al. (2011) note, the quality of imaging was typically insufficient to determine bulge Sérsic indices, and there were no statistically significant differences between their $n_{\mathrm{b}} = 4$ and free n_{b} models. Therefore, we do not compare the Sérsic indices, but focus on the comparison of the disc fractions (obtained, however, from free n_{b} models). On bottom panels of Fig. B2 we show the comparison of D/T ratios of our sample and a sample selected as mentioned above (by using $D/T = 1 - B/T$ to convert their B/T). We plot only our galaxies which could be decomposed into two components. A notable difference between these two samples is that our D/T values peak at a higher value. A possible explanation for this disparity is offered by the right-hand panel comparing the actual mass distributions. As much as we tried to reproduce our sample by selecting galaxies from the much larger Simard et al. (2011) sample, the mass distributions are offset: the sample selected by the above criterion is dominated by galaxies just above $10^{11}\,\mathrm{M}_\odot$, while our sample is dominated by objects of mass $5 \times 10^{10}\,\mathrm{M}_\odot$.

APPENDIX C: DECOMPOSITION PROPERTIES OF ATLAS^{3D} GALAXIES

Downloaded from http://mnras.oxfordjournals.org/ at European Southern Observatory on August 13, 2014

Table C1. Fitting parameters for ATLAS^{3D} galaxies.

Name	μ_{tot} (mag arcsec^{-2})	$R_{e,tot}$ (arcsec)	n_{tot}	μ_b (mag arcsec^{-2})	$R_{e,b}$ (arcsec)	n_b	q_b	μ_d (mag arcsec^{-2})	R_d (arcsec)	q_d	D/T
(1)	(2)	(3)	(4)	(5)	(6)	(7)	(8)	(9)	(10)	(11)	(12)
IC0560	21.32 ± 0.12	16.5 ± 1.0	2.8 ± 0.4	19.39 ± 0.58	2.9 ± 1.2	0.9 ± 0.4	0.71	19.58 ± 0.06	10.8 ± 0.5	0.47	0.81 ± 0.227
IC0598	20.22 ± 0.05	12.9 ± 0.3	2.3 ± 0.1	20.57 ± 0.07	13.7 ± 0.4	1.8 ± 0.2	0.41	0.00 ± 0.00	0.0 ± 0.0	0.00	0.00 ± 0.000
IC0676	22.06 ± 0.20	24.7 ± 2.8	2.7 ± 0.5	0.00 ± 0.00	0.0 ± 0.0	0.0 ± 0.0	0.00	0.00 ± 0.00	0.0 ± 0.0	0.00	0.00 ± 0.000
IC0719	20.03 ± 0.04	14.5 ± 0.2	1.3 ± 0.0	20.00 ± 0.06	14.7 ± 0.3	1.0 ± 0.1	0.29	0.00 ± 0.00	0.0 ± 0.0	0.00	0.00 ± 0.000
IC0782	22.66 ± 0.33	22.3 ± 4.4	3.2 ± 0.8	0.00 ± 0.00	0.0 ± 0.0	0.0 ± 0.0	0.00	0.00 ± 0.00	0.0 ± 0.0	0.00	0.00 ± 0.000
IC1024	20.56 ± 0.10	15.2 ± 0.7	1.2 ± 0.1	20.45 ± 0.12	14.4 ± 0.9	1.4 ± 0.2	0.36	0.00 ± 0.00	0.0 ± 0.0	0.00	0.00 ± 0.000
IC3631	21.26 ± 0.10	12.4 ± 0.6	1.8 ± 0.2	20.89 ± 0.17	11.5 ± 1.3	1.1 ± 0.4	0.83	0.00 ± 0.00	0.0 ± 0.0	0.00	0.00 ± 0.000
NGC 0448	19.32 ± 0.05	11.2 ± 0.3	2.6 ± 0.2	18.29 ± 0.10	4.7 ± 0.3	0.9 ± 0.1	0.38	18.06 ± 0.01	9.1 ± 0.3	0.34	0.69 ± 0.030
NGC 0474	23.84 ± 0.67	77.5 ± 42.2	10.6 ± 2.0	18.62 ± 0.11	4.3 ± 0.3	1.8 ± 0.5	0.93	20.16 ± 0.03	21.3 ± 0.9	0.77	0.67 ± 0.036
NGC 0502	20.90 ± 0.26	13.0 ± 2.0	4.1 ± 1.3	0.00 ± 0.00	0.0 ± 0.0	0.0 ± 0.0	0.00	0.00 ± 0.00	0.0 ± 0.0	0.00	0.00 ± 0.000
NGC 0509	22.03 ± 0.21	23.5 ± 2.9	1.6 ± 0.4	0.00 ± 0.00	0.0 ± 0.0	0.0 ± 0.0	0.00	0.00 ± 0.00	0.0 ± 0.0	0.00	0.00 ± 0.000
NGC 0516	20.86 ± 0.06	16.4 ± 0.4	1.5 ± 0.1	20.83 ± 0.11	16.6 ± 0.7	1.1 ± 0.1	0.35	0.00 ± 0.00	0.0 ± 0.0	0.00	0.00 ± 0.000
NGC 0524	20.67 ± 0.13	31.9 ± 2.1	2.8 ± 0.2	21.83 ± 0.69	41.4 ± 16.2	5.3 ± 2.3	0.94	19.57 ± 0.07	18.6 ± 1.9	0.96	0.28 ± 0.043
NGC 0525	20.75 ± 0.06	10.3 ± 0.3	2.3 ± 0.2	19.72 ± 0.27	3.7 ± 0.4	0.9 ± 0.3	0.87	20.40 ± 0.04	11.3 ± 0.8	0.74	0.71 ± 0.036
NGC 0661	21.29 ± 0.05	20.5 ± 0.5	5.9 ± 0.2	21.07 ± 0.08	18.3 ± 0.7	5.1 ± 0.4	0.73	0.00 ± 0.00	0.0 ± 0.0	0.00	0.00 ± 0.000
NGC 0680	22.40 ± 0.34	32.6 ± 7.1	9.2 ± 1.4	22.55 ± 0.40	35.5 ± 10.3	8.1 ± 1.5	0.81	0.00 ± 0.00	0.0 ± 0.0	0.00	0.00 ± 0.000
NGC 0770	19.63 ± 0.10	6.0 ± 0.3	2.4 ± 0.2	19.25 ± 0.12	4.8 ± 0.5	1.3 ± 0.3	0.71	21.13 ± 0.08	10.9 ± 2.1	0.73	0.31 ± 0.102
NGC 0821	25.14 ± 0.09	248.7 ± 49.3	10.4 ± 0.7	18.58 ± 0.22	5.0 ± 0.7	1.6 ± 0.4	0.66	19.08 ± 0.02	16.8 ± 1.5	0.60	0.74 ± 0.043
NGC 0936	21.55 ± 0.44	53.2 ± 24.9	4.3 ± 2.2	0.00 ± 0.00	0.0 ± 0.0	0.0 ± 0.0	0.00	0.00 ± 0.00	0.0 ± 0.0	0.00	0.00 ± 0.000
NGC 1023	21.39 ± 0.23	157.7 ± 22.4	6.1 ± 0.4	0.00 ± 0.00	0.0 ± 0.0	0.0 ± 0.0	0.00	0.00 ± 0.00	0.0 ± 0.0	0.00	0.00 ± 0.000
NGC 1121	19.64 ± 0.09	7.2 ± 0.3	1.9 ± 0.2	19.81 ± 0.07	8.4 ± 0.3	1.0 ± 0.1	0.44	0.00 ± 0.00	0.0 ± 0.0	0.00	0.00 ± 0.000
NGC 1222	21.05 ± 0.14	14.8 ± 1.0	3.4 ± 0.5	22.38 ± 0.56	22.5 ± 13.1	5.4 ± 2.5	0.72	19.94 ± 0.09	7.7 ± 1.0	0.72	0.21 ± 0.035
NGC 1248	20.60 ± 0.12	12.2 ± 0.7	1.8 ± 0.3	0.00 ± 0.00	0.0 ± 0.0	0.0 ± 0.0	0.00	0.00 ± 0.00	0.0 ± 0.0	0.00	0.00 ± 0.000
NGC 1266	21.30 ± 0.10	17.2 ± 0.8	1.9 ± 0.2	21.35 ± 0.11	17.5 ± 1.0	2.1 ± 0.2	0.77	0.00 ± 0.00	0.0 ± 0.0	0.00	0.00 ± 0.000
NGC 1289	22.46 ± 0.22	30.1 ± 4.1	5.9 ± 0.8	22.52 ± 0.30	30.7 ± 6.2	5.3 ± 1.1	0.59	0.00 ± 0.00	0.0 ± 0.0	0.00	0.00 ± 0.000
NGC 1665	21.87 ± 0.33	26.5 ± 5.9	2.0 ± 1.2	0.00 ± 0.00	0.0 ± 0.0	0.0 ± 0.0	0.00	0.00 ± 0.00	0.0 ± 0.0	0.00	0.00 ± 0.000
NGC 2481	19.28 ± 0.26	8.3 ± 1.0	3.9 ± 0.7	18.25 ± 0.49	2.4 ± 1.3	0.9 ± 0.5	0.81	18.21 ± 0.03	9.5 ± 0.5	0.44	0.82 ± 0.093
NGC 2549	19.95 ± 0.14	25.1 ± 2.0	3.2 ± 0.6	0.00 ± 0.00	0.0 ± 0.0	0.0 ± 0.0	0.00	0.00 ± 0.00	0.0 ± 0.0	0.00	0.00 ± 0.000
NGC 2577	20.57 ± 0.07	15.3 ± 0.5	3.3 ± 0.2	18.71 ± 0.07	4.0 ± 0.2	1.2 ± 0.2	0.62	19.16 ± 0.02	12.2 ± 0.2	0.55	0.72 ± 0.018
NGC 2592	20.46 ± 0.14	11.4 ± 0.8	3.3 ± 0.5	20.59 ± 0.08	12.2 ± 0.5	2.7 ± 0.3	0.80	0.00 ± 0.00	0.0 ± 0.0	0.00	0.00 ± 0.000
NGC 2594†	19.58 ± 0.36	4.8 ± 0.9	12.0 ± 3.6	18.43 ± 0.23	3.1 ± 0.4	1.6 ± 2.2	0.55	20.73 ± 0.11	9.0 ± 5.9	0.60	0.33 ± 0.268
NGC 2679	22.51 ± 0.28	26.3 ± 4.7	3.3 ± 0.9	0.00 ± 0.00	0.0 ± 0.0	0.0 ± 0.0	0.00	0.00 ± 0.00	0.0 ± 0.0	0.00	0.00 ± 0.000
NGC 2685	21.01 ± 0.11	27.2 ± 1.4	4.3 ± 0.4	18.05 ± 0.42	4.1 ± 1.0	0.9 ± 0.4	0.48	18.58 ± 0.03	15.3 ± 0.5	0.43	0.81 ± 0.178
NGC 2695	20.87 ± 0.11	18.2 ± 0.9	4.2 ± 0.4	21.02 ± 0.18	19.5 ± 1.8	3.9 ± 0.7	0.70	0.00 ± 0.00	0.0 ± 0.0	0.00	0.00 ± 0.000
NGC 2698	19.90 ± 0.09	13.8 ± 0.6	3.4 ± 0.4	17.50 ± 0.29	2.2 ± 0.3	1.0 ± 0.3	0.76	18.48 ± 0.02	11.0 ± 0.1	0.51	0.77 ± 0.030
NGC 2699	20.20 ± 0.08	9.6 ± 0.4	4.1 ± 0.4	19.66 ± 0.17	7.6 ± 0.6	2.9 ± 0.5	0.85	0.00 ± 0.00	0.0 ± 0.0	0.00	0.00 ± 0.000
NGC 2764	20.84 ± 0.04	15.7 ± 0.3	1.6 ± 0.1	20.41 ± 0.05	14.6 ± 0.3	1.1 ± 0.1	0.38	0.00 ± 0.00	0.0 ± 0.0	0.00	0.00 ± 0.000
NGC 2768	21.63 ± 0.06	81.8 ± 2.3	3.3 ± 0.1	21.68 ± 0.16	80.3 ± 7.1	2.9 ± 0.2	0.46	0.00 ± 0.00	0.0 ± 0.0	0.00	0.00 ± 0.000
NGC 2778	20.79 ± 0.12	13.4 ± 0.7	2.0 ± 0.4	19.11 ± 0.22	3.3 ± 0.4	1.0 ± 0.3	0.87	19.36 ± 0.04	9.9 ± 0.2	0.79	0.78 ± 0.027
NGC 2824	20.82 ± 0.61	9.1 ± 11.1	6.9 ± 2.7	0.00 ± 0.00	0.0 ± 0.0	0.0 ± 0.0	0.00	0.00 ± 0.00	0.0 ± 0.0	0.00	0.00 ± 0.000
NGC 2852	19.91 ± 0.37	5.6 ± 1.2	7.9 ± 1.7	19.78 ± 0.26	5.2 ± 1.1	1.7 ± 2.0	0.89	22.26 ± 0.18	17.1 ± 11.4	0.86	0.31 ± 0.279
NGC 2859	21.07 ± 0.54	25.6 ± 12.3	6.3 ± 2.1	0.00 ± 0.00	0.0 ± 0.0	0.0 ± 0.0	0.00	0.00 ± 0.00	0.0 ± 0.0	0.00	0.00 ± 0.000
NGC 2880	21.09 ± 0.10	23.8 ± 1.2	4.4 ± 0.4	0.00 ± 0.00	0.0 ± 0.0	0.0 ± 0.0	0.00	0.00 ± 0.00	0.0 ± 0.0	0.00	0.00 ± 0.000
NGC 2950	20.00 ± 0.26	19.1 ± 2.9	6.5 ± 1.7	0.00 ± 0.00	0.0 ± 0.0	0.0 ± 0.0	0.00	0.00 ± 0.00	0.0 ± 0.0	0.00	0.00 ± 0.000
NGC 2962	23.33 ± 0.57	71.7 ± 47.9	6.4 ± 2.2	0.00 ± 0.00	0.0 ± 0.0	0.0 ± 0.0	0.00	0.00 ± 0.00	0.0 ± 0.0	0.00	0.00 ± 0.000
NGC 2974	20.93 ± 0.15	33.1 ± 2.6	4.0 ± 0.4	20.16 ± 0.33	22.1 ± 4.9	2.7 ± 0.6	0.61	0.00 ± 0.00	0.0 ± 0.0	0.00	0.00 ± 0.000
NGC 3032	22.70 ± 0.43	32.8 ± 12.6	4.2 ± 1.7	22.16 ± 0.17	26.2 ± 2.3	2.3 ± 0.4	0.85	0.00 ± 0.00	0.0 ± 0.0	0.00	0.00 ± 0.000
NGC 3073	22.73 ± 0.12	21.5 ± 1.2	4.4 ± 0.4	22.56 ± 0.14	20.0 ± 1.4	3.8 ± 0.5	0.91	0.00 ± 0.00	0.0 ± 0.0	0.00	0.00 ± 0.000
NGC 3098	19.29 ± 0.03	15.7 ± 0.2	1.6 ± 0.0	18.61 ± 0.75	2.1 ± 1.5	0.6 ± 0.1	0.80	17.66 ± 0.03	9.9 ± 0.5	0.36	0.94 ± 0.060
NGC 3156	20.84 ± 0.03	19.9 ± 0.3	1.8 ± 0.1	20.89 ± 0.03	20.5 ± 0.2	1.5 ± 0.0	0.52	0.00 ± 0.00	0.0 ± 0.0	0.00	0.00 ± 0.000
NGC 3182	21.60 ± 0.06	21.3 ± 0.6	2.9 ± 0.1	21.75 ± 0.09	22.6 ± 1.0	3.1 ± 0.2	0.85	0.00 ± 0.00	0.0 ± 0.0	0.00	0.00 ± 0.000
NGC 3193	21.52 ± 0.04	33.1 ± 0.6	5.3 ± 0.1	23.58 ± 1.05	90.3 ± 17.5	9.3 ± 0.8	0.87	19.37 ± 0.07	6.2 ± 3.3	0.85	0.04 ± 0.023
NGC 3226	22.95 ± 0.29	65.4 ± 13.3	4.6 ± 0.7	21.98 ± 0.46	27.2 ± 28.9	5.1 ± 0.6	0.83	21.02 ± 0.12	29.4 ± 4.9	0.83	0.41 ± 0.210
NGC 3230	20.35 ± 0.12	19.5 ± 1.2	2.0 ± 0.3	0.00 ± 0.00	0.0 ± 0.0	0.0 ± 0.0	0.00	0.00 ± 0.00	0.0 ± 0.0	0.00	0.00 ± 0.000
NGC 3245	20.32 ± 0.31	24.5 ± 7.0	3.2 ± 1.9	18.53 ± 0.47	5.9 ± 4.5	2.3 ± 1.3	0.71	19.06 ± 0.05	20.6 ± 1.0	0.54	0.67 ± 0.147
NGC 3248	22.08 ± 0.31	27.8 ± 5.6	5.2 ± 1.5	0.00 ± 0.00	0.0 ± 0.0	0.0 ± 0.0	0.00	0.00 ± 0.00	0.0 ± 0.0	0.00	0.00 ± 0.000

Downloaded from http://mnras.oxfordjournals.org/ at European Southern Observatory on August 13, 2014

Table C1 – *continued*

Name	$\mu_{\rm tot}$ (mag arcsec^{-2})	$R_{\rm e,tot}$ (arcsec)	$n_{\rm tot}$	$\mu_{\rm b}$ (mag arcsec^{-2})	$R_{\rm e,b}$ (arcsec)	$n_{\rm b}$	$q_{\rm b}$	$\mu_{\rm d}$ (mag arcsec^{-2})	$R_{\rm d}$ (arcsec)	$q_{\rm d}$	D/T
(1)	(2)	(3)	(4)	(5)	(6)	(7)	(8)	(9)	(10)	(11)	(12)
NGC 3301	20.28 ± 0.19	27.0 ± 3.5	2.2 ± 0.8	0.00 ± 0.00	0.0 ± 0.0	0.0 ± 0.0	0.00	0.00 ± 0.00	0.0 ± 0.0	0.00	0.00 ± 0.000
NGC 3377	21.61 ± 0.16	53.4 ± 4.5	5.0 ± 0.5	18.44 ± 0.51	7.2 ± 2.0	2.5 ± 1.7	0.52	18.81 ± 0.03	21.9 ± 1.0	0.49	0.69 ± 0.130
NGC 3379	20.83 ± 0.23	49.7 ± 6.4	5.3 ± 0.9	20.74 ± 0.65	40.4 ± 16.9	6.2 ± 1.9	0.86	20.48 ± 0.10	36.3 ± 6.7	0.87	0.19 ± 0.126
NGC 3384	20.40 ± 0.31	40.8 ± 14.2	5.1 ± 2.1	0.00 ± 0.00	0.0 ± 0.0	0.0 ± 0.0	0.00	0.00 ± 0.00	0.0 ± 0.0	0.00	0.00 ± 0.000
NGC 3400	20.95 ± 0.10	14.6 ± 0.6	1.4 ± 0.2	0.00 ± 0.00	0.0 ± 0.0	0.0 ± 0.0	0.00	0.00 ± 0.00	0.0 ± 0.0	0.00	0.00 ± 0.000
NGC 3412	20.36 ± 0.28	28.1 ± 10.0	2.8 ± 2.2	0.00 ± 0.00	0.0 ± 0.0	0.0 ± 0.0	0.00	0.00 ± 0.00	0.0 ± 0.0	0.00	0.00 ± 0.000
NGC 3414	21.37 ± 0.19	33.4 ± 3.5	4.2 ± 0.6	18.95 ± 0.31	6.8 ± 1.0	2.3 ± 0.9	0.78	19.87 ± 0.04	24.4 ± 0.7	0.76	0.66 ± 0.086
NGC 3457	20.22 ± 0.09	9.7 ± 0.4	1.2 ± 0.1	18.26 ± 0.54	1.8 ± 1.0	0.8 ± 0.3	1.00	18.56 ± 0.04	6.3 ± 0.1	0.95	0.84 ± 0.063
NGC 3458	19.97 ± 0.32	10.1 ± 2.3	1.7 ± 0.9	0.00 ± 0.00	0.0 ± 0.0	0.0 ± 0.0	0.00	0.00 ± 0.00	0.0 ± 0.0	0.00	0.00 ± 0.000
NGC 3489	19.51 ± 0.13	22.7 ± 1.6	2.9 ± 0.5	0.00 ± 0.00	0.0 ± 0.0	0.0 ± 0.0	0.00	0.00 ± 0.00	0.0 ± 0.0	0.00	0.00 ± 0.000
NGC 3499	20.31 ± 0.18	7.6 ± 0.7	1.4 ± 0.3	20.27 ± 0.23	7.6 ± 1.0	1.2 ± 0.4	0.85	0.00 ± 0.00	0.0 ± 0.0	0.00	0.00 ± 0.000
NGC 3522	21.32 ± 0.05	16.3 ± 0.4	3.5 ± 0.2	21.80 ± 0.10	19.9 ± 0.9	3.6 ± 0.3	0.54	0.00 ± 0.00	0.0 ± 0.0	0.00	0.00 ± 0.000
NGC 3530	19.35 ± 0.12	6.1 ± 0.4	2.2 ± 0.2	19.41 ± 0.06	7.5 ± 0.2	1.0 ± 0.1	0.73	0.00 ± 0.00	0.0 ± 0.0	0.00	0.00 ± 0.000
NGC 3595	20.76 ± 0.23	15.9 ± 2.1	3.8 ± 1.1	0.00 ± 0.00	0.0 ± 0.0	0.0 ± 0.0	0.00	0.00 ± 0.00	0.0 ± 0.0	0.00	0.00 ± 0.000
NGC 3599	23.23 ± 0.46	46.8 ± 17.0	5.5 ± 1.6	0.00 ± 0.00	0.0 ± 0.0	0.0 ± 0.0	0.00	0.00 ± 0.00	0.0 ± 0.0	0.00	0.00 ± 0.000
NGC 3605	21.34 ± 0.44	18.5 ± 6.5	6.1 ± 2.7	19.78 ± 0.64	5.5 ± 2.9	3.5 ± 2.3	0.68	19.38 ± 0.05	9.6 ± 0.6	0.62	0.54 ± 0.157
NGC 3607	21.74 ± 0.18	59.5 ± 5.6	5.7 ± 0.5	21.21 ± 0.14	46.5 ± 3.2	5.0 ± 0.4	0.89	0.00 ± 0.00	0.0 ± 0.0	0.00	0.00 ± 0.000
NGC 3608	21.21 ± 0.19	31.0 ± 3.0	3.9 ± 0.5	19.38 ± 0.38	8.7 ± 12.1	2.7 ± 0.5	0.81	20.00 ± 0.06	24.2 ± 9.5	0.78	0.58 ± 0.326
NGC 3610	19.69 ± 0.09	15.1 ± 0.7	5.3 ± 0.4	17.03 ± 0.05	3.9 ± 0.1	1.1 ± 0.1	0.55	18.18 ± 0.01	11.8 ± 0.2	0.63	0.64 ± 0.012
NGC 3613	20.69 ± 0.06	29.7 ± 0.8	3.8 ± 0.2	19.08 ± 0.44	7.6 ± 4.5	1.9 ± 1.0	0.66	18.96 ± 0.04	19.1 ± 1.6	0.54	0.69 ± 0.181
NGC 3619	24.67 ± 0.69	119.3 ± 68.0	9.8 ± 1.8	20.49 ± 0.59	10.8 ± 8.3	5.6 ± 2.9	0.91	21.31 ± 0.13	29.9 ± 1.6	0.91	0.46 ± 0.209
NGC 3626	20.99 ± 0.37	29.0 ± 13.2	2.7 ± 1.9	0.00 ± 0.00	0.0 ± 0.0	0.0 ± 0.0	0.00	0.00 ± 0.00	0.0 ± 0.0	0.00	0.00 ± 0.000
NGC 3630	19.32 ± 0.10	13.2 ± 0.7	2.4 ± 0.2	18.05 ± 0.58	3.1 ± 1.3	0.6 ± 0.5	0.81	18.40 ± 0.04	12.1 ± 0.7	0.46	0.81 ± 0.091
NGC 3640	21.40 ± 0.12	42.2 ± 2.7	4.6 ± 0.3	19.68 ± 0.44	16.8 ± 8.8	2.1 ± 0.8	0.77	21.49 ± 0.16	49.9 ± 21.8	0.82	0.40 ± 0.302
NGC 3641†	24.58 ± 0.70	51.9 ± 41.2	12.0 ± 0.0	18.52 ± 0.49	2.6 ± 0.2	1.7 ± 0.4	0.78	21.10 ± 0.11	13.6 ± 4.7	0.92	0.55 ± 0.053
NGC 3648	20.43 ± 0.21	12.9 ± 1.9	1.8 ± 0.8	18.29 ± 0.24	2.5 ± 0.4	0.6 ± 0.3	0.78	18.99 ± 0.03	9.5 ± 0.3	0.60	0.79 ± 0.038
NGC 3658	21.63 ± 0.29	21.1 ± 4.8	2.6 ± 1.6	0.00 ± 0.00	0.0 ± 0.0	0.0 ± 0.0	0.00	0.00 ± 0.00	0.0 ± 0.0	0.00	0.00 ± 0.000
NGC 3665	21.62 ± 0.09	47.3 ± 2.1	3.3 ± 0.2	21.66 ± 0.10	48.5 ± 2.3	2.9 ± 0.2	0.78	0.00 ± 0.00	0.0 ± 0.0	0.00	0.00 ± 0.000
NGC 3674	19.61 ± 0.05	11.5 ± 0.3	2.2 ± 0.1	18.41 ± 0.43	2.9 ± 0.7	5.0 ± 3.1	0.76	18.99 ± 0.04	10.8 ± 0.2	0.50	0.57 ± 0.114
NGC 3694	20.20 ± 0.18	7.4 ± 0.8	2.2 ± 0.4	20.25 ± 0.14	8.1 ± 0.6	1.6 ± 0.3	0.74	0.00 ± 0.00	0.0 ± 0.0	0.00	0.00 ± 0.000
NGC 3757	19.42 ± 0.36	6.2 ± 1.2	3.8 ± 0.9	0.00 ± 0.00	0.0 ± 0.0	0.0 ± 0.0	0.00	0.00 ± 0.00	0.0 ± 0.0	0.00	0.00 ± 0.000
NGC 3796	20.74 ± 0.08	12.3 ± 0.4	3.1 ± 0.3	0.00 ± 0.00	0.0 ± 0.0	0.0 ± 0.0	0.00	0.00 ± 0.00	0.0 ± 0.0	0.00	0.00 ± 0.000
NGC 3838	19.39 ± 0.12	10.2 ± 0.6	2.5 ± 0.2	17.55 ± 0.41	2.1 ± 0.4	0.6 ± 0.3	0.77	18.05 ± 0.03	8.3 ± 0.2	0.49	0.81 ± 0.051
NGC 3941	19.68 ± 0.18	21.3 ± 2.4	2.5 ± 0.6	0.00 ± 0.00	0.0 ± 0.0	0.0 ± 0.0	0.00	0.00 ± 0.00	0.0 ± 0.0	0.00	0.00 ± 0.000
NGC 3945	21.24 ± 0.47	36.9 ± 12.4	6.5 ± 2.5	0.00 ± 0.00	0.0 ± 0.0	0.0 ± 0.0	0.00	0.00 ± 0.00	0.0 ± 0.0	0.00	0.00 ± 0.000
NGC 3998	19.90 ± 0.32	19.3 ± 4.5	4.6 ± 1.9	17.60 ± 0.16	5.0 ± 0.4	1.3 ± 0.4	0.87	19.25 ± 0.03	21.0 ± 0.7	0.81	0.63 ± 0.036
NGC 4026	19.42 ± 0.13	28.5 ± 2.0	2.4 ± 0.4	17.87 ± 0.06	5.4 ± 14.5	1.7 ± 0.8	0.64	18.68 ± 0.03	26.5 ± 1.3	0.40	0.75 ± 0.000
NGC 4036	19.85 ± 0.07	29.3 ± 0.9	2.0 ± 0.1	21.87 ± 0.58	26.9 ± 8.5	8.6 ± 2.2	0.40	18.46 ± 0.04	21.0 ± 0.6	0.43	0.74 ± 0.020
NGC 4078	19.82 ± 0.06	8.9 ± 0.3	3.8 ± 0.2	19.76 ± 0.04	9.6 ± 0.2	2.1 ± 0.1	0.37	0.00 ± 0.00	0.0 ± 0.0	0.00	0.00 ± 0.000
NGC 4111	18.79 ± 0.05	24.6 ± 0.6	2.1 ± 0.1	18.69 ± 0.04	23.3 ± 0.5	2.3 ± 0.1	0.21	0.00 ± 0.00	0.0 ± 0.0	0.00	0.00 ± 0.000
NGC 4119	21.72 ± 0.22	56.1 ± 7.9	2.1 ± 0.3	20.02 ± 0.31	8.0 ± 7.2	0.3 ± 0.5	0.52	19.78 ± 0.05	33.7 ± 2.0	0.41	0.93 ± 0.058
NGC 4143	19.54 ± 0.18	16.9 ± 2.0	2.1 ± 0.6	0.00 ± 0.00	0.0 ± 0.0	0.0 ± 0.0	0.00	0.00 ± 0.00	0.0 ± 0.0	0.00	0.00 ± 0.000
NGC 4150	20.44 ± 0.20	18.0 ± 2.7	2.0 ± 0.7	17.71 ± 0.51	2.6 ± 0.8	1.4 ± 0.6	0.85	19.00 ± 0.04	13.6 ± 0.3	0.70	0.76 ± 0.073
NGC 4168	21.94 ± 0.09	38.4 ± 1.6	3.7 ± 0.2	20.27 ± 0.12	13.5 ± 1.1	1.9 ± 0.2	0.87	21.59 ± 0.06	42.6 ± 2.9	0.88	0.54 ± 0.034
NGC 4179	19.68 ± 0.08	26.0 ± 1.0	2.6 ± 0.2	18.84 ± 0.45	8.1 ± 4.3	1.4 ± 0.8	0.57	18.93 ± 0.04	23.6 ± 2.2	0.38	0.70 ± 0.161
NGC 4191	21.28 ± 0.05	14.9 ± 0.4	3.2 ± 0.2	21.06 ± 0.07	14.0 ± 0.4	2.4 ± 0.2	0.69	0.00 ± 0.00	0.0 ± 0.0	0.00	0.00 ± 0.000
NGC 4203	21.66 ± 0.41	42.8 ± 25.5	5.6 ± 2.5	18.51 ± 0.17	6.8 ± 0.7	1.3 ± 0.4	0.90	19.78 ± 0.04	27.6 ± 1.7	0.91	0.71 ± 0.034
NGC 4215	20.10 ± 0.14	17.8 ± 1.7	1.9 ± 0.5	0.00 ± 0.00	0.0 ± 0.0	0.0 ± 0.0	0.00	0.00 ± 0.00	0.0 ± 0.0	0.00	0.00 ± 0.000
NGC 4233	20.56 ± 0.18	19.9 ± 2.0	3.3 ± 0.7	18.44 ± 0.19	4.4 ± 0.4	0.8 ± 0.2	0.73	20.00 ± 0.04	20.6 ± 1.1	0.63	0.72 ± 0.028
NGC 4249	21.83 ± 0.09	11.6 ± 0.5	1.9 ± 0.2	21.87 ± 0.11	11.8 ± 0.7	1.8 ± 0.4	0.97	0.00 ± 0.00	0.0 ± 0.0	0.00	0.00 ± 0.000
NGC 4251	19.90 ± 0.09	23.4 ± 1.0	3.6 ± 0.3	0.00 ± 0.00	0.0 ± 0.0	0.0 ± 0.0	0.00	0.00 ± 0.00	0.0 ± 0.0	0.00	0.00 ± 0.000
NGC 4255	20.09 ± 0.19	11.6 ± 1.3	2.2 ± 0.4	0.00 ± 0.00	0.0 ± 0.0	0.0 ± 0.0	0.00	0.00 ± 0.00	0.0 ± 0.0	0.00	0.00 ± 0.000
NGC 4259	20.31 ± 0.05	9.1 ± 0.2	2.5 ± 0.1	20.66 ± 0.05	10.6 ± 0.3	1.9 ± 0.1	0.54	0.00 ± 0.00	0.0 ± 0.0	0.00	0.00 ± 0.000
NGC 4261	21.76 ± 0.16	52.1 ± 4.8	5.1 ± 0.4	21.86 ± 0.16	55.4 ± 4.8	5.7 ± 0.5	0.84	0.00 ± 0.00	0.0 ± 0.0	0.00	0.00 ± 0.000
NGC 4262	19.49 ± 0.48	9.8 ± 3.0	4.7 ± 2.6	0.00 ± 0.00	0.0 ± 0.0	0.0 ± 0.0	0.00	0.00 ± 0.00	0.0 ± 0.0	0.00	0.00 ± 0.000
NGC 4264	20.77 ± 0.11	11.7 ± 0.6	2.3 ± 0.3	0.00 ± 0.00	0.0 ± 0.0	0.0 ± 0.0	0.00	0.00 ± 0.00	0.0 ± 0.0	0.00	0.00 ± 0.000

Downloaded from http://mnras.oxfordjournals.org/ at European Southern Observatory on August 13, 2014

Table C1 – *continued*

Name	$\mu_{\rm tot}$ (mag arcsec^{-2})	$R_{\rm e,tot}$ (arcsec)	$n_{\rm tot}$	$\mu_{\rm b}$ (mag arcsec^{-2})	$R_{\rm e,b}$ (arcsec)	$n_{\rm b}$	$q_{\rm b}$	$\mu_{\rm d}$ (mag arcsec^{-2})	$R_{\rm d}$ (arcsec)	$q_{\rm d}$	D/T
(1)	(2)	(3)	(4)	(5)	(6)	(7)	(8)	(9)	(10)	(11)	(12)
NGC 4267	22.01 ± 0.48	37.8 ± 28.4	7.6 ± 2.8	0.00 ± 0.00	0.0 ± 0.0	0.0 ± 0.0	0.00	0.00 ± 0.00	0.0 ± 0.0	0.00	0.00 ± 0.000
NGC 4268	20.36 ± 0.12	14.2 ± 0.9	1.9 ± 0.3	0.00 ± 0.00	0.0 ± 0.0	0.0 ± 0.0	0.00	0.00 ± 0.00	0.0 ± 0.0	0.00	0.00 ± 0.000
NGC 4270	20.38 ± 0.08	18.8 ± 0.7	1.8 ± 0.2	19.09 ± 0.60	3.5 ± 2.0	0.9 ± 0.7	0.73	18.84 ± 0.05	13.2 ± 0.5	0.53	0.87 ± 0.120
NGC 4278	20.70 ± 0.11	31.6 ± 1.6	4.8 ± 0.3	20.96 ± 0.21	35.3 ± 2.9	4.1 ± 0.4	0.92	17.69 ± 0.02	4.2 ± 2.8	0.86	0.07 ± 0.000
NGC 4281	20.63 ± 0.11	28.5 ± 1.5	2.8 ± 0.3	21.84 ± 0.76	27.7 ± 11.7	7.1 ± 2.8	0.45	19.19 ± 0.07	19.0 ± 1.4	0.47	0.54 ± 0.062
NGC 4283	19.92 ± 0.14	9.0 ± 0.6	4.6 ± 0.5	22.18 ± 1.32	21.7 ± 6.5	7.6 ± 1.1	0.96	18.27 ± 0.05	3.9 ± 3.1	0.95	0.19 ± 0.000
NGC 4324	20.25 ± 0.18	22.1 ± 2.7	1.8 ± 0.7	0.00 ± 0.00	0.0 ± 0.0	0.0 ± 0.0	0.00	0.00 ± 0.00	0.0 ± 0.0	0.00	0.00 ± 0.000
NGC 4339	21.88 ± 0.20	31.3 ± 3.6	4.1 ± 0.6	19.85 ± 0.36	8.3 ± 1.9	1.9 ± 0.8	0.96	20.69 ± 0.06	24.5 ± 1.8	0.94	0.60 ± 0.094
NGC 4340	22.32 ± 0.49	51.3 ± 25.4	5.3 ± 2.2	0.00 ± 0.00	0.0 ± 0.0	0.0 ± 0.0	0.00	0.00 ± 0.00	0.0 ± 0.0	0.00	0.00 ± 0.000
NGC 4342	17.98 ± 0.28	5.6 ± 0.7	2.9 ± 0.4	18.61 ± 0.12	8.2 ± 0.5	1.2 ± 0.1	0.38	0.00 ± 0.00	0.0 ± 0.0	0.00	0.00 ± 0.000
NGC 4346	19.84 ± 0.11	22.8 ± 1.3	2.8 ± 0.4	17.91 ± 0.18	4.2 ± 0.4	0.9 ± 0.3	0.75	18.86 ± 0.02	21.1 ± 0.4	0.44	0.77 ± 0.021
NGC 4350	19.39 ± 0.05	19.8 ± 0.5	2.7 ± 0.1	17.49 ± 0.20	3.0 ± 0.3	0.7 ± 0.2	0.78	17.69 ± 0.01	15.1 ± 0.1	0.38	0.86 ± 0.015
NGC 4365	22.08 ± 0.18	86.3 ± 8.6	5.2 ± 0.4	22.16 ± 0.19	91.1 ± 9.6	5.2 ± 0.4	0.76	0.00 ± 0.00	0.0 ± 0.0	0.00	0.00 ± 0.000
NGC 4371	21.42 ± 0.25	48.5 ± 6.7	3.8 ± 0.6	0.00 ± 0.00	0.0 ± 0.0	0.0 ± 0.0	0.00	0.00 ± 0.00	0.0 ± 0.0	0.00	0.00 ± 0.000
NGC 4374	21.90 ± 0.12	87.0 ± 5.4	6.0 ± 0.3	21.52 ± 0.11	73.2 ± 4.1	5.8 ± 0.3	0.94	0.00 ± 0.00	0.0 ± 0.0	0.00	0.00 ± 0.000
NGC 4377	20.14 ± 0.27	13.0 ± 2.6	2.2 ± 1.2	0.00 ± 0.00	0.0 ± 0.0	0.0 ± 0.0	0.00	0.00 ± 0.00	0.0 ± 0.0	0.00	0.00 ± 0.000
NGC 4379	20.41 ± 0.12	15.7 ± 0.9	2.6 ± 0.3	20.33 ± 0.07	15.6 ± 0.5	2.4 ± 0.2	0.70	0.00 ± 0.00	0.0 ± 0.0	0.00	0.00 ± 0.000
NGC 4382	22.32 ± 0.49	133.5 ± 63.4	5.1 ± 1.3	18.60 ± 0.10	10.4 ± 0.6	1.9 ± 0.2	0.79	19.31 ± 0.02	51.0 ± 0.7	0.77	0.83 ± 0.009
NGC 4387	20.20 ± 0.05	13.6 ± 0.4	2.5 ± 0.1	20.20 ± 0.04	14.0 ± 0.3	2.0 ± 0.1	0.59	0.00 ± 0.00	0.0 ± 0.0	0.00	0.00 ± 0.000
NGC 4406†	23.29 ± 0.03	250.0 ± 0.0	5.5 ± 0.2	23.37 ± 0.03	250.0 ± 0.0	5.4 ± 0.1	0.62	0.00 ± 0.00	0.0 ± 0.0	0.00	0.00 ± 0.000
NGC 4417	19.93 ± 0.04	24.6 ± 0.4	2.8 ± 0.1	18.39 ± 0.39	5.3 ± 1.0	1.7 ± 0.6	0.67	18.78 ± 0.04	20.5 ± 0.7	0.44	0.74 ± 0.054
NGC 4425	20.70 ± 0.07	28.2 ± 0.9	1.7 ± 0.1	0.00 ± 0.00	0.0 ± 0.0	0.0 ± 0.0	0.00	0.00 ± 0.00	0.0 ± 0.0	0.00	0.00 ± 0.000
NGC 4429	21.10 ± 0.19	65.2 ± 6.6	2.7 ± 0.3	0.00 ± 0.00	0.0 ± 0.0	0.0 ± 0.0	0.00	0.00 ± 0.00	0.0 ± 0.0	0.00	0.00 ± 0.000
NGC 4434	20.44 ± 0.13	11.9 ± 0.8	2.7 ± 0.4	19.10 ± 0.29	4.7 ± 0.8	1.6 ± 0.8	0.94	19.95 ± 0.05	12.1 ± 0.7	0.94	0.56 ± 0.124
NGC 4435	20.48 ± 0.07	26.7 ± 0.9	4.7 ± 0.3	17.85 ± 0.04	4.1 ± 0.1	0.6 ± 0.1	0.77	17.89 ± 0.01	12.7 ± 0.1	0.61	0.83 ± 0.006
NGC 4442	19.72 ± 0.06	29.3 ± 0.7	2.8 ± 0.2	0.00 ± 0.00	0.0 ± 0.0	0.0 ± 0.0	0.00	0.00 ± 0.00	0.0 ± 0.0	0.00	0.00 ± 0.000
NGC 4452	20.31 ± 0.12	25.3 ± 1.6	1.6 ± 0.2	19.77 ± 0.21	22.9 ± 5.3	1.1 ± 0.6	0.30	0.00 ± 0.00	0.0 ± 0.0	0.00	0.00 ± 0.000
NGC 4458	21.48 ± 0.09	19.9 ± 0.9	2.7 ± 0.3	21.92 ± 0.32	18.3 ± 3.0	5.3 ± 1.3	0.87	20.51 ± 0.08	12.0 ± 0.7	0.89	0.28 ± 0.026
NGC 4459	21.36 ± 0.22	47.1 ± 5.9	3.9 ± 0.5	22.53 ± 0.32	82.0 ± 16.5	7.5 ± 1.4	0.79	0.00 ± 0.00	0.0 ± 0.0	0.00	0.00 ± 0.000
NGC 4461	20.33 ± 0.16	27.8 ± 2.6	2.6 ± 0.6	0.00 ± 0.00	0.0 ± 0.0	0.0 ± 0.0	0.00	0.00 ± 0.00	0.0 ± 0.0	0.00	0.00 ± 0.000
NGC 4472	21.83 ± 0.09	134.2 ± 6.2	4.7 ± 0.1	22.00 ± 0.10	146.7 ± 8.6	4.8 ± 0.2	0.83	0.00 ± 0.00	0.0 ± 0.0	0.00	0.00 ± 0.000
NGC 4473	20.67 ± 0.14	38.2 ± 2.6	5.7 ± 0.5	18.80 ± 0.31	12.6 ± 3.1	3.1 ± 0.8	0.61	20.21 ± 0.05	38.6 ± 1.3	0.54	0.42 ± 0.085
NGC 4474	20.83 ± 0.11	22.8 ± 1.2	3.5 ± 0.4	18.38 ± 0.26	3.5 ± 0.3	0.9 ± 0.3	0.80	18.82 ± 0.03	15.0 ± 0.3	0.48	0.80 ± 0.020
NGC 4476	21.06 ± 0.07	16.7 ± 0.5	4.5 ± 0.3	20.58 ± 0.06	14.0 ± 0.4	4.1 ± 0.3	0.64	0.00 ± 0.00	0.0 ± 0.0	0.00	0.00 ± 0.000
NGC 4477	21.35 ± 0.33	41.4 ± 8.5	4.1 ± 1.2	0.00 ± 0.00	0.0 ± 0.0	0.0 ± 0.0	0.00	0.00 ± 0.00	0.0 ± 0.0	0.00	0.00 ± 0.000
NGC 4478	19.56 ± 0.03	13.0 ± 0.2	2.0 ± 0.1	19.93 ± 0.25	14.3 ± 0.9	1.9 ± 0.1	0.81	18.66 ± 0.03	5.4 ± 3.1	0.83	0.15 ± 0.087
NGC 4483	20.76 ± 0.15	19.4 ± 1.6	2.3 ± 0.4	0.00 ± 0.00	0.0 ± 0.0	0.0 ± 0.0	0.00	0.00 ± 0.00	0.0 ± 0.0	0.00	0.00 ± 0.000
NGC 4486	20.90 ± 0.13	74.2 ± 5.0	2.9 ± 0.2	21.56 ± 0.14	97.4 ± 7.1	4.1 ± 0.3	0.89	0.00 ± 0.00	0.0 ± 0.0	0.00	0.00 ± 0.000
NGC 4486A	18.49 ± 0.53	5.0 ± 1.2	3.7 ± 0.8	18.49 ± 0.53	5.0 ± 1.2	3.7 ± 0.8	0.85	0.00 ± 0.00	0.0 ± 0.0	0.00	0.00 ± 0.000
NGC 4489	21.52 ± 0.16	20.0 ± 1.6	2.3 ± 0.5	19.80 ± 0.38	4.8 ± 1.0	2.5 ± 1.6	0.94	20.18 ± 0.06	15.0 ± 0.5	0.92	0.70 ± 0.108
NGC 4494	21.03 ± 0.13	45.0 ± 3.1	3.4 ± 0.3	20.86 ± 0.08	42.5 ± 1.4	2.7 ± 0.2	0.82	0.00 ± 0.00	0.0 ± 0.0	0.00	0.00 ± 0.000
NGC 4503	20.74 ± 0.18	33.1 ± 3.5	2.8 ± 0.6	0.00 ± 0.00	0.0 ± 0.0	0.0 ± 0.0	0.00	0.00 ± 0.00	0.0 ± 0.0	0.00	0.00 ± 0.000
NGC 4521	20.25 ± 0.14	19.5 ± 1.6	2.4 ± 0.5	20.92 ± 0.18	24.4 ± 2.7	2.1 ± 0.6	0.63	0.00 ± 0.00	0.0 ± 0.0	0.00	0.00 ± 0.000
NGC 4526	20.44 ± 0.18	74.1 ± 7.4	2.7 ± 0.3	19.22 ± 0.12	18.1 ± 1.5	1.0 ± 0.2	0.64	19.64 ± 0.03	58.7 ± 5.4	0.47	0.73 ± 0.036
NGC 4528	19.53 ± 0.07	11.3 ± 0.4	2.1 ± 0.1	0.00 ± 0.00	0.0 ± 0.0	0.0 ± 0.0	0.00	0.00 ± 0.00	0.0 ± 0.0	0.00	0.00 ± 0.000
NGC 4546	19.76 ± 0.08	25.8 ± 0.9	3.3 ± 0.2	17.58 ± 0.55	4.0 ± 5.5	3.4 ± 1.2	0.83	18.20 ± 0.03	18.6 ± 0.6	0.50	0.69 ± 0.284
NGC 4550	19.65 ± 0.03	20.2 ± 0.3	1.7 ± 0.1	20.91 ± 0.24	29.9 ± 3.3	1.4 ± 0.2	0.34	17.63 ± 0.02	6.9 ± 0.5	0.40	0.37 ± 0.084
NGC 4551	20.41 ± 0.02	15.4 ± 0.1	2.0 ± 0.0	21.20 ± 0.29	14.5 ± 1.4	4.2 ± 1.4	0.71	19.19 ± 0.04	9.8 ± 0.3	0.74	0.45 ± 0.037
NGC 4552	21.34 ± 0.12	49.3 ± 3.1	6.2 ± 0.4	21.67 ± 0.15	56.7 ± 4.5	6.7 ± 0.6	0.90	0.00 ± 0.00	0.0 ± 0.0	0.00	0.00 ± 0.000
NGC 4564	19.97 ± 0.07	21.9 ± 0.7	2.9 ± 0.2	20.39 ± 0.09	14.7 ± 0.6	5.7 ± 0.4	0.49	18.85 ± 0.02	17.2 ± 0.2	0.46	0.55 ± 0.004
NGC 4570	19.35 ± 0.06	25.1 ± 0.7	2.4 ± 0.2	18.12 ± 0.45	5.4 ± 1.5	1.9 ± 0.8	0.64	18.41 ± 0.03	22.7 ± 0.7	0.35	0.74 ± 0.072
NGC 4578	22.23 ± 0.48	43.1 ± 18.2	5.2 ± 2.0	19.19 ± 0.14	6.4 ± 0.5	1.6 ± 0.3	0.78	20.33 ± 0.04	27.2 ± 1.0	0.71	0.71 ± 0.022
NGC 4596	21.83 ± 0.14	59.2 ± 4.5	3.8 ± 0.3	0.00 ± 0.00	0.0 ± 0.0	0.0 ± 0.0	0.00	0.00 ± 0.00	0.0 ± 0.0	0.00	0.00 ± 0.000
NGC 4608	25.05 ± 0.41	196.2 ± 84.6	10.5 ± 1.9	0.00 ± 0.00	0.0 ± 0.0	0.0 ± 0.0	0.00	0.00 ± 0.00	0.0 ± 0.0	0.00	0.00 ± 0.000
NGC 4612	21.42 ± 0.20	31.4 ± 3.7	3.5 ± 0.7	0.00 ± 0.00	0.0 ± 0.0	0.0 ± 0.0	0.00	0.00 ± 0.00	0.0 ± 0.0	0.00	0.00 ± 0.000
NGC 4621	21.08 ± 0.09	52.4 ± 2.3	4.3 ± 0.2	20.21 ± 0.11	25.9 ± 37.4	4.2 ± 0.7	0.63	19.78 ± 0.06	31.8 ± 13.8	0.63	0.38 ± 0.000

Downloaded from http://mnras.oxfordjournals.org/ at European Southern Observatory on August 13, 2014

Table C1 – *continued*

Name	μ_{tot} (mag arcsec^{-2})	$R_{e,tot}$ (arcsec)	n_{tot}	μ_b (mag arcsec^{-2})	$R_{e,b}$ (arcsec)	n_b	q_b	μ_d (mag arcsec^{-2})	R_d (arcsec)	q_d	D/T
(1)	(2)	(3)	(4)	(5)	(6)	(7)	(8)	(9)	(10)	(11)	(12)
NGC 4623	20.98 ± 0.04	25.7 ± 0.4	2.0 ± 0.1	21.36 ± 0.63	11.9 ± 8.7	2.9 ± 1.5	0.37	19.42 ± 0.06	17.4 ± 0.9	0.34	0.79 ± 0.058
NGC 4624	22.39 ± 0.45	68.6 ± 24.0	4.6 ± 1.3	0.00 ± 0.00	0.0 ± 0.0	0.0 ± 0.0	0.00	0.00 ± 0.00	0.0 ± 0.0	0.00	0.00 ± 0.000
NGC 4636‡	23.32 ± 0.29	193.2 ± 36.3	5.5 ± 0.5	23.78 ± 0.04	250.0 ± 0.9	5.6 ± 0.2	0.69	0.00 ± 0.00	0.0 ± 0.0	0.00	0.00 ± 0.000
NGC 4638	19.96 ± 0.16	17.5 ± 1.4	4.6 ± 0.7	22.52 ± 0.10	45.9 ± 2.4	1.0 ± 0.8	0.69	16.53 ± 0.01	6.1 ± 0.3	0.41	0.58 ± 0.054
NGC 4643	22.45 ± 0.47	71.3 ± 26.9	7.4 ± 1.6	0.00 ± 0.00	0.0 ± 0.0	0.0 ± 0.0	0.00	0.00 ± 0.00	0.0 ± 0.0	0.00	0.00 ± 0.000
NGC 4649	21.89 ± 0.25	119.6 ± 17.5	5.1 ± 0.5	18.79 ± 0.11	17.0 ± 1.2	1.8 ± 0.1	0.85	19.73 ± 0.02	63.3 ± 1.8	0.77	0.68 ± 0.021
NGC 4660	19.31 ± 0.07	12.1 ± 0.4	3.5 ± 0.2	19.26 ± 0.18	9.0 ± 1.0	5.6 ± 1.3	0.64	18.40 ± 0.02	9.5 ± 0.4	0.62	0.36 ± 0.031
NGC 4684	20.08 ± 0.06	24.5 ± 0.6	1.9 ± 0.1	19.16 ± 0.37	8.8 ± 1.0	0.8 ± 0.8	0.42	18.99 ± 0.03	20.5 ± 3.9	0.40	0.78 ± 0.034
NGC 4690	22.03 ± 0.12	21.9 ± 1.3	2.8 ± 0.3	22.04 ± 0.14	21.6 ± 1.5	2.5 ± 0.3	0.72	0.00 ± 0.00	0.0 ± 0.0	0.00	0.00 ± 0.000
NGC 4694	21.48 ± 0.04	36.1 ± 0.7	3.0 ± 0.1	20.18 ± 0.29	12.5 ± 10.3	1.6 ± 0.4	0.48	20.09 ± 0.04	25.6 ± 8.0	0.44	0.64 ± 0.369
NGC 4697	21.72 ± 0.10	96.4 ± 4.6	4.6 ± 0.2	21.04 ± 1.69	53.3 ± 40.4	4.2 ± 2.0	0.59	19.41 ± 0.10	31.9 ± 4.9	0.54	0.29 ± 0.270
NGC 4710	20.26 ± 0.07	49.1 ± 1.4	1.1 ± 0.1	20.27 ± 0.08	49.3 ± 1.6	1.1 ± 0.1	0.25	0.00 ± 0.00	0.0 ± 0.0	0.00	0.00 ± 0.000
NGC 4733	21.74 ± 0.09	27.9 ± 1.2	1.8 ± 0.2	0.00 ± 0.00	0.0 ± 0.0	0.0 ± 0.0	0.00	0.00 ± 0.00	0.0 ± 0.0	0.00	0.00 ± 0.000
NGC 4753	21.40 ± 0.18	80.6 ± 8.1	2.9 ± 0.3	22.05 ± 0.29	100.9 ± 20.4	3.3 ± 0.5	0.55	0.00 ± 0.00	0.0 ± 0.0	0.00	0.00 ± 0.000
NGC 4754	21.00 ± 0.11	41.3 ± 2.4	4.5 ± 0.3	0.00 ± 0.00	0.0 ± 0.0	0.0 ± 0.0	0.00	0.00 ± 0.00	0.0 ± 0.0	0.00	0.00 ± 0.000
NGC 4762	20.58 ± 0.17	72.4 ± 6.9	3.0 ± 0.3	17.57 ± 0.05	3.1 ± 46.1	0.9 ± 0.8	0.73	18.08 ± 0.02	35.7 ± 12.6	0.14	0.90 ± 0.000
NGC 4803	19.92 ± 0.18	6.2 ± 0.6	2.8 ± 0.6	19.90 ± 0.12	6.3 ± 0.4	1.8 ± 0.3	0.62	0.00 ± 0.00	0.0 ± 0.0	0.00	0.00 ± 0.000
NGC 5103	20.45 ± 0.26	12.6 ± 1.9	3.9 ± 1.5	17.80 ± 0.52	1.9 ± 0.8	0.6 ± 0.4	0.83	18.14 ± 0.03	7.7 ± 0.4	0.51	0.83 ± 0.089
NGC 5173	20.43 ± 0.07	8.7 ± 0.3	4.4 ± 0.3	19.70 ± 0.33	5.5 ± 2.5	2.7 ± 1.0	0.87	21.07 ± 0.13	10.6 ± 5.8	0.87	0.26 ± 0.260
NGC 5198	21.14 ± 0.08	20.3 ± 0.8	2.6 ± 0.2	22.59 ± 0.56	32.0 ± 11.3	4.4 ± 2.2	0.88	19.53 ± 0.07	8.4 ± 0.8	0.83	0.22 ± 0.034
NGC 5273	21.72 ± 0.32	31.7 ± 8.2	1.8 ± 1.1	19.43 ± 0.47	3.9 ± 1.2	1.2 ± 0.7	0.89	19.86 ± 0.06	20.2 ± 0.7	0.91	0.90 ± 0.032
NGC 5308	21.72 ± 0.32	31.7 ± 8.2	1.8 ± 1.1	18.00 ± 0.30	3.1 ± 0.5	0.7 ± 0.3	0.66	18.18 ± 0.02	17.5 ± 0.3	0.31	0.88 ± 0.024
NGC 5322	21.79 ± 0.07	64.7 ± 2.2	5.5 ± 0.1	21.95 ± 0.15	67.9 ± 5.5	5.8 ± 0.4	0.66	0.00 ± 0.00	0.0 ± 0.0	0.00	0.00 ± 0.000
NGC 5342	19.81 ± 0.05	8.1 ± 0.2	2.4 ± 0.1	18.25 ± 0.41	1.7 ± 0.5	1.1 ± 0.5	0.82	18.52 ± 0.04	6.6 ± 0.1	0.53	0.79 ± 0.068
NGC 5353	19.93 ± 0.14	22.3 ± 1.7	3.3 ± 0.5	0.00 ± 0.00	0.0 ± 0.0	0.0 ± 0.0	0.00	0.00 ± 0.00	0.0 ± 0.0	0.00	0.00 ± 0.000
NGC 5355	20.79 ± 0.04	10.1 ± 0.2	2.4 ± 0.1	20.92 ± 0.02	10.6 ± 0.1	2.2 ± 0.1	0.70	0.00 ± 0.00	0.0 ± 0.0	0.00	0.00 ± 0.000
NGC 5358	20.67 ± 0.03	10.8 ± 0.2	2.0 ± 0.1	19.35 ± 0.46	2.1 ± 0.3	0.7 ± 0.4	0.81	19.38 ± 0.05	7.9 ± 0.2	0.56	0.85 ± 0.033
NGC 5379	21.54 ± 0.20	22.6 ± 2.2	1.1 ± 0.5	0.00 ± 0.00	0.0 ± 0.0	0.0 ± 0.0	0.00	0.00 ± 0.00	0.0 ± 0.0	0.00	0.00 ± 0.000
NGC 5422	19.93 ± 0.20	22.1 ± 3.4	1.7 ± 0.7	18.76 ± 0.47	4.2 ± 23.7	1.6 ± 1.3	0.69	19.41 ± 0.06	22.2 ± 6.7	0.36	0.78 ± 0.410
NGC 5473	20.89 ± 0.25	21.3 ± 3.0	3.7 ± 1.0	0.00 ± 0.00	0.0 ± 0.0	0.0 ± 0.0	0.00	0.00 ± 0.00	0.0 ± 0.0	0.00	0.00 ± 0.000
NGC 5475	20.20 ± 0.09	18.6 ± 0.8	1.5 ± 0.2	18.87 ± 0.58	2.4 ± 1.7	0.6 ± 0.3	0.83	18.79 ± 0.05	13.3 ± 0.6	0.39	0.91 ± 0.072
NGC 5481	22.19 ± 0.28	27.5 ± 4.3	3.7 ± 0.9	22.46 ± 0.29	31.1 ± 5.0	3.4 ± 0.8	0.71	0.00 ± 0.00	0.0 ± 0.0	0.00	0.00 ± 0.000
NGC 5485	21.46 ± 0.06	31.5 ± 1.0	3.1 ± 0.1	21.74 ± 0.19	34.7 ± 3.7	3.4 ± 0.5	0.74	0.00 ± 0.00	0.0 ± 0.0	0.00	0.00 ± 0.000
NGC 5493	19.88 ± 0.09	13.1 ± 0.6	5.8 ± 0.5	21.90 ± 2.06	26.0 ± 0.8	11.1 ± 0.4	0.68	16.78 ± 0.03	5.4 ± 3.4	0.42	0.33 ± 0.228
NGC 5500	21.99 ± 0.08	15.5 ± 0.6	2.9 ± 0.2	22.94 ± 0.77	16.6 ± 3.9	7.7 ± 2.4	0.76	20.62 ± 0.12	8.7 ± 0.8	0.78	0.32 ± 0.051
NGC 5507	20.19 ± 0.17	13.1 ± 1.4	2.1 ± 0.7	18.36 ± 0.36	2.9 ± 0.7	1.0 ± 0.6	0.84	19.38 ± 0.04	11.8 ± 0.6	0.76	0.75 ± 0.045
NGC 5557	21.12 ± 0.15	26.9 ± 2.0	3.8 ± 0.4	21.29 ± 0.15	29.1 ± 2.2	4.4 ± 0.5	0.84	0.00 ± 0.00	0.0 ± 0.0	0.00	0.00 ± 0.000
NGC 5574	20.73 ± 0.41	16.4 ± 4.6	3.8 ± 1.8	19.84 ± 0.16	13.0 ± 1.3	1.1 ± 0.3	0.60	0.00 ± 0.00	0.0 ± 0.0	0.00	0.00 ± 0.000
NGC 5576	22.79 ± 0.24	72.9 ± 9.1	11.3 ± 0.9	22.49 ± 0.29	63.2 ± 10.8	9.2 ± 1.1	0.67	0.00 ± 0.00	0.0 ± 0.0	0.00	0.00 ± 0.000
NGC 5582	23.12 ± 0.44	58.4 ± 22.9	7.3 ± 1.8	0.00 ± 0.00	0.0 ± 0.0	0.0 ± 0.0	0.00	0.00 ± 0.00	0.0 ± 0.0	0.00	0.00 ± 0.000
NGC 5611	19.63 ± 0.09	9.1 ± 0.4	2.8 ± 0.2	19.91 ± 0.05	10.7 ± 0.3	1.8 ± 0.1	0.44	0.00 ± 0.00	0.0 ± 0.0	0.00	0.00 ± 0.000
NGC 5631	21.35 ± 0.13	24.8 ± 1.6	4.3 ± 0.5	21.14 ± 0.09	22.7 ± 1.0	4.2 ± 0.4	0.90	0.00 ± 0.00	0.0 ± 0.0	0.00	0.00 ± 0.000
NGC 5638	21.25 ± 0.08	27.1 ± 1.0	3.5 ± 0.2	23.46 ± 1.46	69.1 ± 40.9	8.0 ± 2.7	0.87	20.19 ± 0.15	12.4 ± 0.9	0.93	0.12 ± 0.083
NGC 5687	22.61 ± 0.29	42.8 ± 6.9	6.6 ± 1.1	18.90 ± 0.15	3.9 ± 0.5	1.4 ± 0.5	0.76	19.35 ± 0.02	12.2 ± 1.1	0.65	0.71 ± 0.055
NGC 5770	21.01 ± 0.18	14.8 ± 1.3	3.3 ± 0.8	0.00 ± 0.00	0.0 ± 0.0	0.0 ± 0.0	0.00	0.00 ± 0.00	0.0 ± 0.0	0.00	0.00 ± 0.000
NGC 5813	23.28 ± 0.57	110.4 ± 65.3	5.8 ± 1.7	24.17 ± 0.74	117.6 ± 88.8	9.1 ± 2.2	0.70	20.93 ± 0.15	39.5 ± 3.1	0.75	0.31 ± 0.095
NGC 5831	21.73 ± 0.06	30.0 ± 0.9	4.3 ± 0.2	21.33 ± 0.08	25.2 ± 1.0	4.3 ± 0.3	0.90	0.00 ± 0.00	0.0 ± 0.0	0.00	0.00 ± 0.000
NGC 5838	20.34 ± 0.18	30.8 ± 3.5	3.4 ± 0.7	0.00 ± 0.00	0.0 ± 0.0	0.0 ± 0.0	0.00	0.00 ± 0.00	0.0 ± 0.0	0.00	0.00 ± 0.000
NGC 5839	21.58 ± 0.30	18.6 ± 3.0	3.1 ± 1.2	0.00 ± 0.00	0.0 ± 0.0	0.0 ± 0.0	0.00	0.00 ± 0.00	0.0 ± 0.0	0.00	0.00 ± 0.000
NGC 5845	17.17 ± 0.40	2.7 ± 1.1	5.2 ± 0.8	17.50 ± 0.17	3.0 ± 0.7	3.8 ± 0.5	0.75	20.34 ± 0.09	6.3 ± 4.8	0.75	0.08 ± 0.000
NGC 5846	22.07 ± 0.09	67.4 ± 3.2	3.9 ± 0.2	22.23 ± 0.11	72.8 ± 4.1	4.1 ± 0.2	0.92	0.00 ± 0.00	0.0 ± 0.0	0.00	0.00 ± 0.000
NGC 5854	20.06 ± 0.06	21.1 ± 0.7	1.7 ± 0.1	0.00 ± 0.00	0.0 ± 0.0	0.0 ± 0.0	0.00	0.00 ± 0.00	0.0 ± 0.0	0.00	0.00 ± 0.000
NGC 5864	20.14 ± 0.07	23.7 ± 0.7	1.3 ± 0.1	0.00 ± 0.00	0.0 ± 0.0	0.0 ± 0.0	0.00	0.00 ± 0.00	0.0 ± 0.0	0.00	0.00 ± 0.000
NGC 5866	20.18 ± 0.11	46.7 ± 2.6	2.3 ± 0.2	21.43 ± 0.26	72.3 ± 10.7	1.8 ± 0.5	0.42	17.57 ± 0.02	13.5 ± 0.8	0.42	0.33 ± 0.092
NGC 5869	21.40 ± 0.11	24.4 ± 1.2	4.8 ± 0.4	21.93 ± 0.17	30.4 ± 2.7	5.4 ± 0.7	0.75	0.00 ± 0.00	0.0 ± 0.0	0.00	0.00 ± 0.000
NGC 6010	19.94 ± 0.12	19.2 ± 1.4	1.8 ± 0.4	20.33 ± 0.22	23.5 ± 6.5	0.8 ± 0.9	0.24	0.00 ± 0.00	0.0 ± 0.0	0.00	0.00 ± 0.000

Downloaded from http://mnras.oxfordjournals.org/ at European Southern Observatory on August 13, 2014

Table C1 – *continued*

Name	$\mu_{\rm tot}$ (mag arcsec^{-2})	$R_{\rm e,tot}$ (arcsec)	$n_{\rm tot}$	$\mu_{\rm b}$ (mag arcsec^{-2})	$R_{\rm e,b}$ (arcsec)	$n_{\rm b}$	$q_{\rm b}$	$\mu_{\rm d}$ (mag arcsec^{-2})	$R_{\rm d}$ (arcsec)	$q_{\rm d}$	D/T
(1)	(2)	(3)	(4)	(5)	(6)	(7)	(8)	(9)	(10)	(11)	(12)
NGC 6014	22.01 ± 0.14	21.1 ± 1.4	1.7 ± 0.2	21.86 ± 0.13	20.5 ± 1.2	1.6 ± 0.2	0.63	0.00 ± 0.00	0.0 ± 0.0	0.00	0.00 ± 0.000
NGC 6017	19.84 ± 0.10	6.3 ± 0.3	3.7 ± 0.3	19.78 ± 0.05	7.6 ± 0.1	1.2 ± 0.1	0.52	16.58 ± 0.00	1.3 ± 6.3	0.86	0.32 ± 0.173
NGC 6149	20.88 ± 0.17	10.4 ± 0.9	2.3 ± 0.6	19.38 ± 0.35	3.2 ± 0.5	0.9 ± 0.4	0.76	19.83 ± 0.05	9.1 ± 0.7	0.70	0.73 ± 0.057
NGC 6278	20.46 ± 0.34	14.1 ± 4.8	2.5 ± 1.4	18.83 ± 0.49	3.8 ± 1.6	1.3 ± 0.9	0.80	19.61 ± 0.06	13.7 ± 1.5	0.52	0.66 ± 0.160
NGC 6547	20.44 ± 0.20	15.7 ± 1.6	3.4 ± 0.6	17.85 ± 0.67	1.7 ± 1.2	0.6 ± 0.6	0.88	18.57 ± 0.04	8.8 ± 1.6	0.47	0.83 ± 0.184
NGC 6548	25.50 ± 0.29	199.0 ± 80.2	10.5 ± 1.8	0.00 ± 0.00	0.0 ± 0.0	0.0 ± 0.0	0.00	0.00 ± 0.00	0.0 ± 0.0	0.00	0.00 ± 0.000
NGC 6703	22.14 ± 0.32	39.0 ± 8.1	5.9 ± 1.1	22.29 ± 0.34	41.9 ± 8.7	6.1 ± 1.0	0.96	0.00 ± 0.00	0.0 ± 0.0	0.00	0.00 ± 0.000
NGC 6798	21.67 ± 0.22	23.6 ± 2.8	4.0 ± 0.6	21.73 ± 0.96	13.8 ± 15.0	6.7 ± 2.6	0.53	20.03 ± 0.08	13.3 ± 1.2	0.55	0.50 ± 0.129
NGC 7280	22.44 ± 0.59	42.8 ± 41.8	6.1 ± 2.1	0.00 ± 0.00	0.0 ± 0.0	0.0 ± 0.0	0.00	0.00 ± 0.00	0.0 ± 0.0	0.00	0.00 ± 0.000
NGC 7332	19.44 ± 0.13	24.4 ± 1.7	2.3 ± 0.4	17.61 ± 0.50	3.5 ± 1.5	1.4 ± 0.7	0.70	18.29 ± 0.03	20.1 ± 0.6	0.35	0.80 ± 0.202
NGC 7454	21.49 ± 0.21	29.5 ± 3.8	3.4 ± 0.4	20.53 ± 0.12	19.1 ± 1.2	1.9 ± 0.2	0.65	0.00 ± 0.00	0.0 ± 0.0	0.00	0.00 ± 0.000
NGC 7457	21.96 ± 0.30	59.1 ± 12.1	3.1 ± 0.5	21.32 ± 0.54	18.7 ± 7.5	3.6 ± 0.9	0.59	19.77 ± 0.06	29.0 ± 0.8	0.55	0.73 ± 0.065
NGC 7465	19.27 ± 0.08	7.3 ± 0.3	3.6 ± 0.2	19.30 ± 0.09	7.6 ± 0.4	2.9 ± 0.3	0.69	0.00 ± 0.00	0.0 ± 0.0	0.00	0.00 ± 0.000
NGC 7693	20.79 ± 0.08	9.3 ± 0.4	1.1 ± 0.2	0.00 ± 0.00	0.0 ± 0.0	0.0 ± 0.0	0.00	0.00 ± 0.00	0.0 ± 0.0	0.00	0.00 ± 0.000
NGC 7710	20.05 ± 0.05	8.3 ± 0.2	2.5 ± 0.2	20.53 ± 0.12	9.8 ± 0.6	2.2 ± 0.5	0.47	0.00 ± 0.00	0.0 ± 0.0	0.00	0.00 ± 0.000
PGC016060	20.42 ± 0.05	13.5 ± 0.3	1.4 ± 0.1	20.41 ± 0.09	13.1 ± 0.6	0.8 ± 0.1	0.29	0.00 ± 0.00	0.0 ± 0.0	0.00	0.00 ± 0.000
PGC028887	22.52 ± 0.39	15.7 ± 4.1	8.4 ± 2.0	19.77 ± 0.65	3.7 ± 1.6	9.9 ± 2.3	0.68	22.13 ± 0.19	13.2 ± 1.1	0.69	0.21 ± 0.086
PGC029321	20.85 ± 0.11	6.0 ± 0.3	0.8 ± 0.1	20.82 ± 0.16	5.9 ± 0.4	0.8 ± 0.2	0.88	0.00 ± 0.00	0.0 ± 0.0	0.00	0.00 ± 0.000
PGC035754	20.85 ± 0.21	7.4 ± 0.8	7.8 ± 1.4	19.08 ± 0.35	3.1 ± 1.3	5.7 ± 3.2	0.67	22.85 ± 0.26	17.8 ± 2.1	0.68	0.20 ± 0.161
PGC042549	20.46 ± 0.13	9.1 ± 0.6	1.6 ± 0.2	0.00 ± 0.00	0.0 ± 0.0	0.0 ± 0.0	0.00	0.00 ± 0.00	0.0 ± 0.0	0.00	0.00 ± 0.000
PGC044433	19.73 ± 0.10	7.1 ± 0.3	1.9 ± 0.2	18.43 ± 0.47	1.5 ± 0.5	0.6 ± 0.3	0.79	18.59 ± 0.04	5.7 ± 0.2	0.54	0.85 ± 0.049
PGC050395	21.35 ± 0.10	9.7 ± 0.4	3.2 ± 0.4	21.35 ± 0.13	9.7 ± 0.6	2.7 ± 0.6	0.76	0.00 ± 0.00	0.0 ± 0.0	0.00	0.00 ± 0.000
PGC051753	20.54 ± 0.10	8.5 ± 0.4	1.4 ± 0.2	20.43 ± 0.07	8.5 ± 0.3	0.9 ± 0.1	0.45	0.00 ± 0.00	0.0 ± 0.0	0.00	0.00 ± 0.000
PGC054452	21.53 ± 0.08	11.4 ± 0.4	1.7 ± 0.2	0.00 ± 0.00	0.0 ± 0.0	0.0 ± 0.0	0.00	0.00 ± 0.00	0.0 ± 0.0	0.00	0.00 ± 0.000
PGC056772	20.93 ± 0.13	9.4 ± 0.6	2.3 ± 0.3	20.76 ± 0.12	9.3 ± 0.5	1.4 ± 0.2	0.51	0.00 ± 0.00	0.0 ± 0.0	0.00	0.00 ± 0.000
PGC058114⋆	0.00 ± 0.00	0.0 ± 0.0	0.0 ± 0.0	0.00 ± 0.00	0.0 ± 0.0	0.0 ± 0.0	0.00	0.00 ± 0.00	0.0 ± 0.0	0.00	0.00 ± 0.000
PGC061468	21.12 ± 0.18	9.4 ± 1.0	1.6 ± 0.4	20.57 ± 0.15	6.7 ± 0.5	0.9 ± 0.2	0.74	0.00 ± 0.00	0.0 ± 0.0	0.00	0.00 ± 0.000
PGC071531⋆	0.00 ± 0.00	0.0 ± 0.0	0.0 ± 0.0	0.00 ± 0.00	0.0 ± 0.0	0.0 ± 0.0	0.00	0.00 ± 0.00	0.0 ± 0.0	0.00	0.00 ± 0.000
PGC170172	20.41 ± 0.10	6.0 ± 0.3	1.0 ± 0.2	0.00 ± 0.00	0.0 ± 0.0	0.0 ± 0.0	0.00	0.00 ± 0.00	0.0 ± 0.0	0.00	0.00 ± 0.000
UGC03960	24.35 ± 0.49	50.2 ± 26.5	6.8 ± 1.8	21.10 ± 0.78	6.0 ± 5.8	5.4 ± 0.9	0.95	21.75 ± 0.22	18.6 ± 0.8	0.74	0.50 ± 0.193
UGC04551	19.27 ± 0.24	9.8 ± 1.2	2.5 ± 0.5	0.00 ± 0.00	0.0 ± 0.0	0.0 ± 0.0	0.00	0.00 ± 0.00	0.0 ± 0.0	0.00	0.00 ± 0.000
UGC05408	20.26 ± 0.21	4.7 ± 0.5	3.4 ± 0.6	0.00 ± 0.00	0.0 ± 0.0	0.0 ± 0.0	0.00	0.00 ± 0.00	0.0 ± 0.0	0.00	0.00 ± 0.000
UGC06062	20.73 ± 0.07	11.3 ± 0.4	3.0 ± 0.3	0.00 ± 0.00	0.0 ± 0.0	0.0 ± 0.0	0.00	0.00 ± 0.00	0.0 ± 0.0	0.00	0.00 ± 0.000
UGC06176	20.99 ± 0.10	12.1 ± 0.6	1.7 ± 0.2	0.00 ± 0.00	0.0 ± 0.0	0.0 ± 0.0	0.00	0.00 ± 0.00	0.0 ± 0.0	0.00	0.00 ± 0.000
UGC08876	19.88 ± 0.16	9.0 ± 0.7	2.0 ± 0.3	0.00 ± 0.00	0.0 ± 0.0	0.0 ± 0.0	0.00	0.00 ± 0.00	0.0 ± 0.0	0.00	0.00 ± 0.000
UGC09519	20.10 ± 0.19	6.7 ± 0.7	2.3 ± 0.4	18.04 ± 0.51	1.6 ± 0.8	0.7 ± 1.5	0.76	18.27 ± 0.03	4.7 ± 0.2	0.63	0.78 ± 0.186

Column (1): the name is the principal designation from LEDA, which is used as standard designation.
Column (2): effective surface brightness of the single Sérsic fit in mag arcsec^{-2}.
Column (3): effective radius of the single Sérsic fit in arcsec.
Column (4): Sérsic index of the single Sérsic fit.
Column (5): effective surface brightness of the bulge component in mag arcsec^{-2}.
Column (6): effective radius of the bulge in arcsec.
Column (7): Sérsic index of the bulge component.
Column (8): flattening of the bulge component.
Column (9): effective surface brightness of the exponential component in mag arcsec^{-2}.
Column (10): effective radius of the exponential component in arcsec.
Column (11): flattening of the exponential component.
Column (12): disc-to-total light ratio.
Note that Columns (2)–(4) are results of one-component Sérsic fits to profiles azimuthally averaged along fixed ellipses, while columns (5)–(11) are results of two-component fits to profiles azimuthally averaged along free ellipses. This explains the difference between ($\mu_{\rm tot}$, $R_{\rm tot}$, $n_{\rm tot}$) and ($\mu_{\rm b}$, $R_{\rm b}$, $n_{\rm b}$) when two-component fit was not required ($\mu_{\rm d} = 0$, $R_{\rm d} = 0$).
⋆ *r*-band imaging not available. †Single-component fit did not converge (parameters at boundary conditions). ‡Two-component fit did not converge (parameters at boundary conditions).

This paper has been typeset from a TEX/LATEX file prepared by the author.

Downloaded from http://mnras.oxfordjournals.org/ at European Southern Observatory on August 13, 2014